MODIFICATION OF A HIGH REYNOLDS NUMBER TURBULENT BOUNDARY LAYER WITH THE ADDITION OF DRAG-REDUCING POLYMER SOLUTION

By

YASAMAN FARSIANI

Bachelor of Science in Aerospace Engineering
Azad University Science and Research branch
Tehran, Iran
2011

Master of Science in Aerospace Engineering
Amirkabir University of Technology
Tehran, Iran
2014

Submitted to the Faculty of the
Graduate College of the
Oklahoma State University
in partial fulfillment of
the requirements for
the Degree of
DOCTOR OF PHILOSOPHY
May 2020

MODIFICATION OF A HIGH REYNOLDS NUMBER TURBULENT BOUNDARY LAYER WITH THE ADDITION OF DRAG-REDUCING POLYMER SOLUTION

Dissertation Approved:

Dr. Brian Elbing

Dissertation Adviser

Dr. Khaled Sallam

Dr. Arvind Santhanakrishnan

Dr. Geir Hareland

ACKNOWLEDGEMENTS

I would like to express my sincere gratitude to my advisor Dr. Brian Elbing, who has given me continuous support during my Ph.D. research. Without his guidance and persistent help, this dissertation would not have been possible. I also want to thank Dr. Arvind Santhanakrishnan, Dr. Khaled Sallam, and Dr. Geir Hareland for serving in my committee and sharing their comments and suggestion throughout my research work. I also acknowledge the support from the U.S. National Science Foundation (NSF Award #1604978). I would like to acknowledge my colleague, Zeeshan Saeed for helping me performing experiments, gathering the data, and analyzing the results. All of my success is possible because of the endless love and support of my parents Parichehr and Gholamreza and my brother Soroosh. Finally, I would like to thank my amazing friends, Azadeh Zandieh, Sara Soltani and Kyle Tatroult for their unconditional support and motivation.

Name: YASAMAN FARSIANI

Date of Degree: MAY, 2020

Title of Study: MODIFICATION OF A HIGH REYNOLDS NUMBER TURBULENT
BOUNDARY LAYER WITH THE ADDITION OF DRAG-REDUCING
POLYMER SOLUTION

Major Field: MECHANICAL AND AEROSPACE ENGINEERING

Abstract: Polymer drag reduction (PDR) is an active flow control technique that has drawn significant scientific examination and industrial interest for over 70 years (e.g. fluid transport in oil pipelines, surface ships, safer fuels, drug delivery). While it is well known that trace amounts of polymer solutions can reduce drag by up to 80%, the fluid mechanism of how the polymers reduce the drag remains elusive. Recent findings have shown that polymer properties influence how PDR modifies the near-wall mean velocity profile, which is in contrast to the classical view. Consequently, the current study uses a novel technique to create a developing turbulent boundary layer within a homogeneous polymer solution (i.e. polymer ocean), in which polymer properties are sensitive to polymer concentration. This has never been attempted before due to known issues with polymer degradation, which this study includes an assessment of the impact of mechanical degradation on polymer drag reduction performance. The degradation study showed that degradation effects can have an impact on the performance, but these can be mitigated with sufficiently large residence times. The modifications to the velocity distribution are analyzed using particle image velocimetry. Analysis included comparisons between mean and fluctuating velocity profiles and proper orthogonal decomposition (POD). In addition, modifications to coherent structures were studying via two-point correlations between the fluctuating velocity components to reveal modifications to the intermittency of the near-wall events. Results show that for the controlled range of Reynolds number ($800<Re_\theta<3000$), a critical polymer dependent parameter, Weissenberg number (*Wi*), has a dominant effect on controlling the modified near-wall turbulence. Specifically, the polymers suppress wall-normal fluctuations while amplifying the streamwise fluctuations. For the coherent structures, the structure configuration is strongly dependent on *Wi* at high drag reduction (>40%). A linear relationship was identified between structure inclination angle, α, (in the TBL log-region), and drag reduction (DR), $\alpha=-0.563DR+46.9$. Faster convergence of cumulative turbulent kinetic energy (TKE) of the POD modes was observed in polymeric cases, which signifies a smaller number of structures containing the total TKE compared to Newtonian flow. This further suggests that polymers are involved in severely mitigating the spatiotemporal evolution of vortical structure in the TBL near-wall region, a process that significantly contributes to the production of skin-friction drag.

TABLE OF CONTENTS

Chapter Page

Chapter Page

LIST OF FIGURES

Figure Page

Figure Page

LIST OF TABLES

Table Page

CHAPTER I

1 INTRODUCTION

1.1 Motivation

Drag reduction methods have become very popular for the past seven decades, as they improve the mechanical efficiency of transportation systems moving in fluids. Polymer drag reduction (PDR) has been known to be effective as an active flow control technique. Consequently, it has found extensive use in applications such as the transportation of crude oil, suspensions and slurries, oil well fracturing operations, biomedical fields, and external applications such as marine vehicles (White & Mungal, 2008; Perlin et al., 2016), for which in 2010 there was a successful application of PDR to improve ship speed on a sailing vessel (Elbing, 2018). However, the knowledge that polymer additives reduce skin friction dates back to the late 1940s.

In 1948, Toms (1948) reported that dissolving a trace amount (10 parts per million) of poly (methyl methacrylate) (PMMA) into monochlorobenzene can significantly reduce the friction drag in high Reynolds number pipe flow. Subsequently, similar observations were made in a wide variety of polymer-solvent pairs. It was observed that under certain circumstances, the percentage drop in friction drag can be as high as 80% (Virk, 1975). PDR across different chemical species shows the effect to be mechanical and rheological, caused by the coupling between polymer dynamics and turbulent flow motions rather than any specific chemical interaction.

The most effective drag-reducing polymer molecules are long chains with flexible backbones, although rigid polymers are also known to cause drag reduction (DR) (Paschkewitz et al., 2005). A comprehensive review of the chronological use of polymers to effect drag reduction being used for various applications is provided in Sellin (1982).

Polymer was commercially used in 1979 as a drag reducer in a 48-inch diameter and 800-mile long Trans-Alaska crude oil pipeline from North to South Alaska (Burger et al., 1982). Since then, polymer additives have been acknowledged for their DR ability. In spite of the mentioned applications, there remain some unresolved fundamental issues that limit the application of polymer drag reduction to various systems. One significant open area of research is the proper scaling of the mean and fluctuating velocity profiles within a polymer-modified turbulent boundary layer (TBL) at high-Reynolds numbers. On the other hand, since the intermittent events and coherent structure of polymeric vorticies are obscured in mean velocity profiles, studying the turbulent structure configuration and modifications with PDR is key to understand the mechanism of drag reduction.

Based on recent challenges and limitations faced in understanding and implementing PDR, three main objectives were selected for the current study. These objectives, which are discussed in the next subsection, are (1) drag reduction performance of mechanically degraded polymer, (2) modifications to TBL mean statistics with PDR, and (3) modifications to TBL coherent structure with PDR.

1.2 Study Objectives

1.2.1 Drag reduction performance of mechanically degraded polymer

As previously mentioned, PDR has significant potential for the transportation and industrial sectors, but the effectiveness of this method is heavily dependent on and limited by one very crucial parameter, which is intrinsic to the polymer drag reduction mechanism. This factor is that of the polymer degradation under immense flow strains, of which turbulent flows are a rich source. Such strain-induced polymer breakdown is referred to as "mechanical degradation of polymer molecule chains." This results in the shortening of the polymer chains, by virtue of their breakdown under stressed states, because of the superimposed strains of the flow field. This is a critical issue because the efficiency of the polymer depends on the polymer molecule chain length, with the effectiveness of the polymer as a drag-reducing agent being proportional to its chain length. Studies, such as work of Habibpour and Clark (2017) show that historically such degradation issues have conveniently been avoided by either assuming such degradations effects to be negligible or by using grades of polymer that are resistant to such chain cleavages, thereby making such degradations to be of secondary importance. However, using such degradation-resistant polymers limits their drag-reducing efficiency and therefore makes their practical application less promising, especially for external applications.

Also, the rheological aspects of the problem suggest that such degradation is a natural cause-and-effect type event if drag reduction is to be affected. Therefore, the characterization of polymer degradation has to be done for a complete and meaningful analysis. This part of the study entirely focuses on degradation due to chain scission induced from high shear rates (i.e. mechanical degradation). Virk (1975) showed that a larger quantity of polymer and higher molecular weight (M_w) results in higher drag reduction until maximum drag reduction (MDR). However, to reduce the cost of polymer usage, smaller quantities with higher M_w is desirable. Recent PDR studies have focused primarily on high molecular weight polyethylene oxide (PEO), as has been the case in external flow studies because PEO has the ability to achieve MDR with a very dilute solution and also the fact that use of PEO conveniently avoids the rheological issues faced with commercial-grade polyacrylamide (PAM). However, polymer degradation has had a significant impact on PDR external applications and even the ability to study PDR within TBLs. Therefore, characterizing the degradation of long-chain polymers and their drag reduction performance is an important area of investigation. This serves as the motivation behind the first goal of the current study. Most of this chapter has been published in Farsiani et al. (2020a).

1.2.2 PDR modification of TBL mean statistics

The classical view of the mean velocity distribution in PDR flows is that below MDR the log-region of the boundary layer is unmodified from the traditional law of the wall for Newtonian fluids ($U^+ = ln(y^+)/\kappa + B$), though shifted outward into the flow (i.e., the constant B increases with increasing drag reduction). Here U^+ is the mean streamwise velocity (U) scaled with the friction velocity (u_τ) and $y^+$is the distance from the wall scaled with viscous wall unit (l_ν), and κ is the von-Karman coefficient. This view was first proposed in Virk (1975), where results from several sources were compiled and suggested that it was valid until MDR is achieved (termed the ultimate profile). The entire ultimate profile beyond the viscous sublayer takes the empirically derived form of $U^+ = 11.7\ ln(y^+) - 17$. This ultimate profile has accurately predicted (within measurement uncertainty) the behavior of drag reduced flows independent of the polymer type, molecular weight, or the type of solvent used (Virk, 1975). The classical view of the velocity distribution at intermediate levels of drag reduction is that beyond the viscous sublayer, the velocity profile follows the ultimate profile until reaching what has been termed the “Newtonian plug”. In the Newtonian plug, the κ is assumed to be the same as in the Newtonian condition, though the intercept constant (B) has increased in proportion to the level of drag reduction. White et al. (2012) provides a schematic of the classical view of how the mean velocity distribution for a wall-bounded flow of polymer solution is modified, which this figure is reproduced in Figure 1-1.

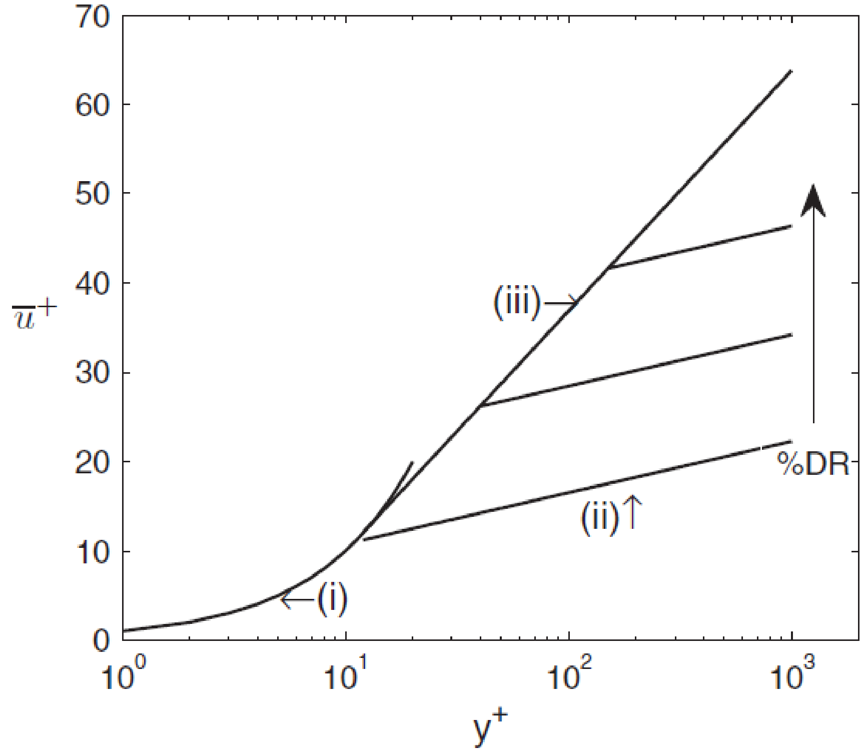

Figure 1-1 A schematic of the behaviors of the mean velocity distribution for a wall-bounded flow of polymer solutions: (i) $U^+ = y^+$, (ii) is the Newtonian "law of the wall" given by $U^+ = \ln(y^+)/0.4 + 5.0$, and (iii) is the "ultimate profile." This figure is a reprint from the work of White et al. (2012).

Since the work of Virk (1975), there have been significant improvements in the ability to accurately measure the velocity distribution in wall-bounded flows. The results from these more precise measurements indicate that there are deviations from this classical view, especially at intermediate levels of drag reduction. Deviations have been experimentally observed in pipe flows (Ptasinski et al., 2001), channel flows (Wei & Willmarth, 1992; Warholic et al., 1999; Escudier et al., 2009), and TBL flows (Fontaine et al., 1992; White et al., 2004; Petrie et al., 2005; Hou et al., 2008), which several of these profiles are shown in Figure 1-2. At high drag reduction (HDR) however, the slope of the mean velocity profile clearly deviates from classical view in the log-law region. In addition, the mean velocity profile was shown to no longer follow the conventional logarithmic dependence at MDR as it does for Newtonian flows (White et al., 2012; Elbing et al., 2013). All of this evidence indicates that turbulent DR is divided into three regimes: low drag reduction (LDR), HDR and MDR processes with each one of them having distinct mechanisms with polymer and flow properties responsible for the deviations in velocity profiles from the classical view.

Most PDR studies have been homogenous polymer solution in pipe flow (e.g., Virk, 1975), direct numerical simulation (DNS) study of polymer solution in channel (e.g., Dubief et al., 2004), or polymer injection in a TBL (e.g., Somandepalli et al., 2010; Hou et al., 2008). The effect of polymer diffusion and changes in the concentration of polymer solutions at different regions of the boundary layer makes it hard to predict, interpret, and compare the experimental data. For example, in the work of Kim and Sirviente (2005), turbulent characteristics of both homogeneous and heterogeneous polymeric flows in a fully developed turbulent channel presented the distribution of the velocity fluctuations and shear stress across the channel. However, they did not seem to indicate substantial differences in the region where the majority of the polymer structures are present. The other limiting factor of proper scaling of the TBL with the properties of the injected polymers is the diffusion of the polymer solution in the developing TBL and degradation of polymers due to chain session. Owing to the aforementioned limitations, current work investigates homogeneous polymer solutions in a developing TBL over a flat plate. Such challenges and gaps in literature with regard to understanding the modifications to mean statistics of TBLs, as well as the deviations observed between experimental and numerical works, motivated this study to investigate the polymer and flow properties in HDR and LDR of homogenous polymer solution responsible for controlling the TBL. Scaling the velocity profiles with the corresponding parameters will lead to a fundamental understanding of the DR mechanism and can have important implications in the area of flow control. In particular, other DR techniques mainly result in flow statistics characteristic of LDR regime (Deng et al., 2016). Knowing how polymers change the dynamics of TBL in HDR regime, will inspire new approaches in controlling the wall-bounded flows. Portions of this chapter have been published in Farsiani et al. (2020a,b).

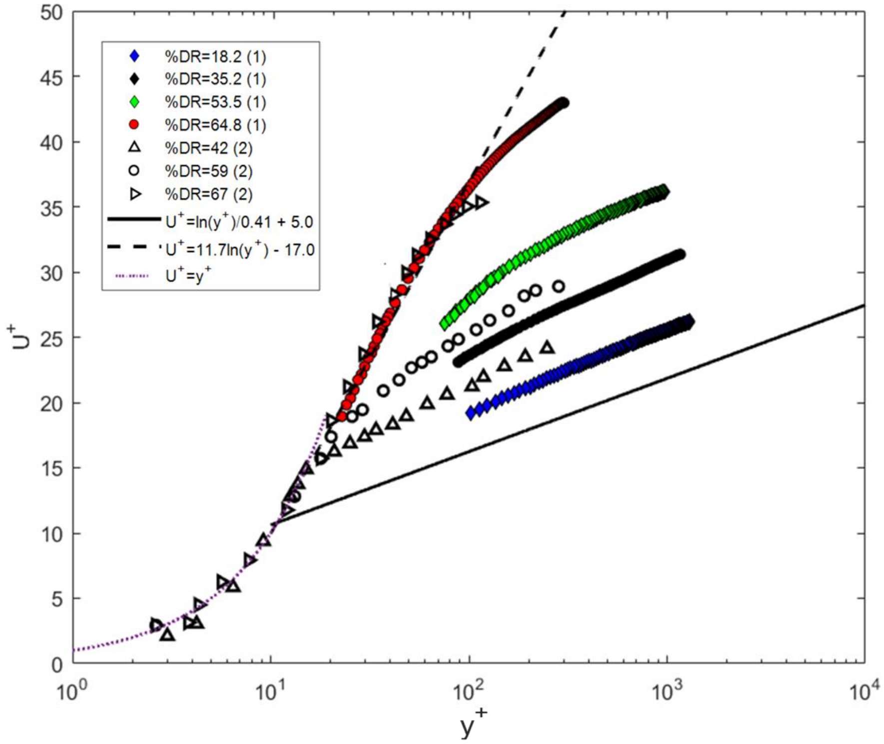

Figure 1-2 Polymeric velocity profiles from a TBL with non-uniform concentration ((1): Elbing et al., 2013) and channel flow with a constant concentration ((2): Escudier et al., 2009), which both show an increasing slope in the log-region with increasing drag reduction for HDR (DR > 40%).

1.2.3 PDR modifications of turbulent coherent structures

Various studies over the past century of TBLs reveal velocity fluctuations in which slow-moving fluid close to the wall is ejected outward and fast-moving fluid farther away from the wall is swept inward towards the wall. This phenomenon is the dominant mechanism for the generation and sustenance of turbulence in wall-bounded flows. The generation of turbulence that increases skin friction drag leads to heavy losses and inefficiency in various applications. For example, the skin friction drag constitutes up to 70% of total drag in ships and over 90% in gas and oil pipelines. Swirling eddies of various scales are responsible for the mechanism that generates and sustains turbulence. Therefore, it is of primary importance to characterize the eddy structure, in particular, the manner in which eddies evolve, regenerate, and sustain turbulence. Understanding the physics and basic dynamics governing these eddies helps develop better control and prediction strategies. For example, predicting the location of the regions that generate turbulence is a potential strategy to control the flow.

Flow statistics and turbulent dynamics are often conceptualized in the framework of coherent structures, such as vortices and streaks. These structures are commonly spotted in both numerical and experimental works. Flow visualization techniques in experiments or DNS describes mechanisms of self-sustaining processes and momentum transport in turbulent flows. Attempts have also been made to establish the relationship between the mean velocity profile and the underlying coherent structures (Lozano-Duran et al., 2012). For viscoelastic turbulence, it is commonly accepted that polymer stresses can cause DR by suppressing the motion of vortices (Dubief et al., 2004; Kim et al., 2008), which offers a convincing explanation for the onset of DR. Much less is known about the transition to HDR for which the slope of the log-law is dramatically augmented and the Reynolds shear stress is modulated (Warholic et al., 1999; Ptasinski et al., 2003). It is hypothesized that the LDR-HDR transition is coupled with the change in the self-sustaining near-wall turbulence cycle. These two regimes of DR are controlled by polymer properties, flow properties, or a combination of the two affecting structures of turbulence and their regeneration process. In this sense, Weissenberg number (Wi) is the main parameter governing polymer properties and sets the ratio of elastic forces to the viscous forces. This makes the final objective of this study to find the effect of Wi in the range of Reynolds number ($800 < Re_\theta < 3000$) in LDR and HDR on coherent structures in the TBL. Portions of this section have been published in Farsiani et al. (2020b).

1.3 Breakdown of the Current Study

Objective 1: To investigate the drag reduction performance of mechanically degraded dilute polymer solution (polyethylene oxide [PEO]).

Objective 2: To study the modifications to the mean and fluctuating velocity profiles with polymer drag reduction.

Objective 3. To study the modified TBL coherent structures with polymer solution in LDR and HDR.

The remainder of this dissertation is divided into six chapters. A review of previous work is presented in Chapter 2. Chapter 3 provides details of the experimental setup, instrumentation, and data analysis methods. Chapter 4 details the characterization of mechanical degradation in polymer drag reduced flow, which provides guidelines and justification for creating a homogeneous polymer ocean in a water tunnel for the following chapters. Chapter 5 presents the experimental study of the modification of mean and fluctuating velocity profiles with the drag-reducing polymer solution, which includes a brief introduction, detailed experimental results, and discussions. Chapter 6 presents an experimental study on the coherent structures in the modified turbulent boundary layer with drag-reducing polymers and also includes a brief introduction, experimental results, numerical methods to analyze experimental data and discussion. Finally, in Chapter 7, the final remarks and conclusions of this work are provided in addition to recommendations for future work.

CHAPTER II

2 LITERATURE REVIEW

The literature review is divided into three sections; review of work done on flow-induced polymer degradation, review of the modification of the mean and fluctuating velocity profiles within polymer drag reduced flow, and review of modified coherent structures with polymer drag reduction. This chapter provides the background and literature review of past studies related to each of these focused areas, which identifies gaps in knowledge related to polymer drag reduction and its modification to the TBL. This dissertation serves to fill these gaps in knowledge.

2.1 Review of Flow-Induced Polymer Degradation

One of the primary limiting factors for using PDR in external and internal flows is polymer degradation. Polymer degradation is subject to many initiating factors such as oxidative and bacterial action, free radical interaction (chemical degradation), thermal degradation, and mechanical degradation (Bailey & Koleske, 1976; Shin, 1965; Bortel & Lamot, 1977). The aging of polymer solution has also been found to contribute to polymer solution degradation (Layec-Raphalen & Layec, 1985). The polymer degradation problem is intensified by the fact that polymers are generally more efficient at reducing drag (i.e. require lower concentrations to achieve the desired drag reduction) the longer the polymer chain, but the longer the polymer chain the more susceptible it is to chain scission.

Internal flows have historically avoided this problem by using stiffer polymers (e.g. polyacrylamides), and some applications have shown an increase in resistance to mechanical degradation with increasing concentration (Habibpour & Clark, 2017). However, the use of commercial-grade PAM is not suitable for investigations involving the influence of molecular weight on drag reduction and mechanical degradation because of their branched-chain formation and the presence of copolymers (Gampert & Wagner, 1985). Instead, PDR studies have focused primarily on high molecular weight polyethylene oxide (PEO), as has been the case in external flow studies, because PEO has the ability to achieve MDR with concentrations ~10 parts per million (ppm) and also the fact that use of PEO conveniently avoids the rheological issues faced with commercial-grade PAM owing to its branched-chain formulation. This is ideal given external flows continuously dilute the polymer solution injected into the developing boundary layer. However, as a result, polymer degradation has had a significant impact on PDR external applications and even the ability to study PDR within TBLs.

Elbing et al. (2011) developed a fundamental scaling law for the evolution of the mean molecular weight within a developing high-shear TBL, which requires an estimate of the steady-state molecular weight for the given local shear rate. This was produced from the universal scaling law for chain scission (Vanapalli et al., 2006), given that the nominal bond strengths for carbon-carbon and carbon-oxygen bonds are 4.1 nN and 4.3 nN (Grandbois et al., 1999), respectively. In light of this scaling law, a review of the literature that has reported PDR modifications to the near-wall velocity profile of a TBL with PEO (Fontaine et al., 1992; White et al., 2004; Petrie et al., 2005; Hou et al., 2008; Somandepalli et al., 2010; Elbing et al., 2013) shows that many of the reported conditions (Fontaine et al., 1992; Petrie et al., 2005; Elbing et al., 2013) experienced significant changes in the mean molecular weight between the injection and measurement locations. This is particularly problematic when studying HDR (DR > 40%). Recent computational and experimental work (see Figure 2.1, which is a reproduction of the findings from Elbing et al.

(2013)) has shown that modifications to the near-wall velocity profile deviate from the classical view that assumes the near-wall momentum distribution is independent of polymer properties. Elbing et al. (2013) showed that the Reynolds number was insufficient to collapse the available experimental TBL data, which suggests that the remaining scatter in the results must be related to polymer properties. These polymer properties are sensitive to the molecular weight, which means that in addition to an evolving polymer concentration distribution, there is also an evolving molecular weight distribution that needs to be accounted for to properly study HDR in TBLs. This has motivated the current work to seek an alternative approach, which is to develop a polymer ocean at a uniform concentration that has been mechanically degraded to a steady-state molecular weight (Farsiani et al., 2020a,b). Then, the developing boundary layer would have a known and uniform polymer concentration and mean molecular weight. However, this requires a proper understanding of the impact of mechanical degradation via chain scission on the drag reduction performance of PEO, which is the focus of Chapter 4 of this dissertation.

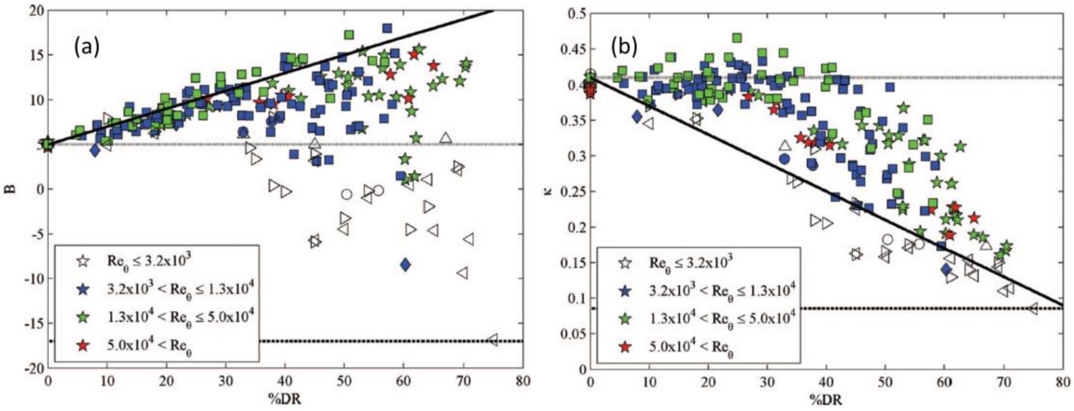

Figure 2-1 (a) The intercept constant B plotted versus the percent drag reduction (%DR). Results shown are from the (☆) Elbing et al. (2013), (◦) Koskie and Tiederman (1991), (◇) Fontaine et al. (1992), (Δ) White et al. (2004), ( ) Petrie et al. (2005), (◁) Hou et al. (2008) and (▷) Somandepalli et al. (2010). The symbol color corresponds to the Reynolds number range as shown in the legend. Dashed lines indicate the Newtonian value (B = 5.0) and the ultimate profile ($B = -17$). The solid line ($B = 5 + (0.2)$ [%DR]) was a linear fit to data presented in Petrie et al. (2005). (b) The von-Karman constant as a function of %DR from several studies (symbols and colors are the same as [a]). The dashed lines correspond to the values corresponding to Newtonian (κ = 0.41) and the ultimate profile ($\kappa = 1 / 11.7 \approx 0.0855$). The solid line is a linear fit to data presented in Koskie and Tiederman (1991). This figure has been produced from the work of Elbing et al. (2013).

While the literature for polymer degradation (mostly for internal flows) is vast, this review focuses on primary papers that influenced the current work. While certain chemical interactions, such as free radical interaction, bacterial oxidation, etc. can degrade long-chain polymers (e.g., Moussa & Tiu, 1994; Fore et al., 2005), the focus of the current study is limited to mechanical or flow-assisted degradation. The flow-induced shear (mechanical force) on the polymer chain can be generated from abrupt changes in flow geometry (e.g. pumps, valves, and perforations; Zaitoun et al., 2012) or large mean velocity gradients such as those experienced at the wall of high Reynolds number turbulent flows (Fontaine et al., 1992; Petrie et al., 2005; Elbing et al., 2009, 2011). Initial studies (e.g. Culter et al., 1975) discovered that it was extremely challenging to produce a setup that could isolate the degradation to the flow region of interest. Even more recent studies have frequently concluded that the majority of the degradation was produced at the entrance to their test facility (Moussa & Tiu, 1994; Vanapalli et al., 2005; Elbing et al., 2009).

Yu et al. (1979) were one of the earliest investigations on the influence of flow-assisted (mechanical) degradation on the molecular distribution. Monodisperse polystyrene and polydisperse polyisobutene samples in oils were tested under high shear rates, which showed that the molecular distribution narrowed for the polydispersed samples and only had a slight broadening of the monodispersed sample. More specifically, the distributions revealed that the breaking of the chains was not a random process. Hinch (1977) laid out a formula detailing the required force to break a molecular chain at a given location of the chain. This theoretical evaluation showed that maximum strain developed in stretching the chain was indeed at its center. Subsequently, Horn and Merrill (1984) showed that turbulence-induced scission of macromolecules in dilute solutions preferentially break at the midpoint of the chain. Moreover, Odell et al. (1983) studied extensional flow produced in cross-slot devices with PEO to show a resulting molecular weight distribution with another peak in addition to the original one at half the molecular weight, indicating the scission of the chain at its midpoint. Much later work using a simulation of flow-induced polymer chain scission (Sim et al., 2007), validated the midpoint scission hypothesis under the condition that the elongation rate was comparable to the critical elongation rate, then the instantaneous segmental tensions attains a maximum at the chain midpoint. This has the consequence of the resulting daughter chains having a rather narrow distribution. However, it was also demonstrated that when the elongational rate is much larger than the critical elongational rate, scission can occur in the partially coiled chains resulting in scission occurring farther from the midpoint. This likely has a significant impact within wall-bounded turbulent flows, where the stress distribution varies significantly from the maximum at the wall to very weak away from the wall (e.g. pipe centerline or outside of a TBL).

Most significantly, Gampert and Wagner (1985) made use of laboratory synthesized straight molecular chain PAM in aqueous solutions to investigate the influence of molecular weight and polydispersity on the drag-reducing effectiveness of the polymer and made several conclusions that are in excellent agreement with the available literature and the findings with PEO in this investigation. However, the work of Gampert and Wagner (1985) differs from this work in that they artificially created polydispersity by mixing the highest and lowest synthesized molecular weight in a single solution. Whereas this study primarily includes the effect of PEO chain scission due to high shear rates and the effect of resulting polydispersity on the drag-reducing characteristics. Another important work by Paterson and Abernathy (1970), concludes that the specifics of post-degradation molecular weight distribution is key in evaluating the influence of degradation on polymer flow properties.

Hunston and Zakin (1980) used turbulent drag reduction (similar to work in Chapter 4), viscosity and gel permeation chromatography (GPC) on polystyrene samples to assess the influence of concentration, molecular weight, and molecular weight distribution on flow-assisted (mechanical) degradation. This showed that the onset of drag reduction provided information about the largest molecules in the flow, while the flow rate dependence was related to the shape of the top part of the molecular weight distribution. This suggests that the work of Vanapalli et al. (2005) with PEO and PAM shows a good correlation between the mean molecular weight and the onset of drag reduction. The work of Vanapalli et al. (2005) is valid when the distribution shape remains relatively constant, which is expected if the scission occurs near the midpoint and there is sufficiently large residence time. Like many previous degradation studies (e.g., Hunston & Zakin, 1980; Moussa & Tiu, 1994; Kim et al., 2000; Kulik, 2001; Elbing et al., 2009), the current work utilizes the drag reduction performance to investigate the degradation.

GPC and other such methods are preferred since they provide direct measurements of the molecular weight distribution, but GPC has proven to be impractical due to being difficult and uncertain for analysis of the high molecular weight PEO aqueous solution samples. One of the main issues that complicate this approach is that while PEO is soluble in tetrahydrofuran (THF), a common eluent for GPC, it is isorefractive with THF. This makes it so that it cannot be seen in that solvent with either index of refraction or light scattering detectors (Elbing, 2018). Another limitation in the use of GPC for estimating the polydispersity comes from its incapability to resolve low molecular weight fractions for PEO molecular weights as low as 2.5×10^5 g/mol (Berman, 1977). Such lower molecular weight fractions are known to significantly affect the number average molecular weight of a sample necessary to evaluate polydispersity (Berman, 1977; Gampert & Wagner, 1985). This renders the use of GPC for high molecular weight samples ineffective and so has not been used in this investigation. Thus, the first part of the current study quantifies the impact of mechanical degradation via chain scission on the drag reduction performance of PEO primarily from the resulting variations in the turbulent drag reduction performance. Based on previous studies using other polymer solutions, the likely impact on the molecular weight distribution is inferred.

2.2 Turbulent Boundary Layer Modification

The classical view of how polymers modified velocity profiles near the wall is presented in Virk (1975), which is a comprehensive experimental observation up to that time, especially, flow statistics and their parameter dependence. Later availability of new research tools, in particular, DNS and particle image velocimetry (PIV), allows access to detailed flow and polymer stress fields, which has led to significant new discoveries in the past two decades. Many of those advances were covered in the reviews of Graham (2004) and White and Mungal (2008). Detailed experiments have characterized two distinct regimes (Warholic et al., 1999), referred to as LDR (DR < ~40%) and HDR (DR > ~40%). The first regime exhibits similar statistical trends to Newtonian flow: the log-law region of the mean velocity profile remains parallel to that of the Newtonian flow but its lower bound moves away from the wall, and the upward shift of the log-region is a function of drag reduction. Although streamwise fluctuations are increased and transverse ones are reduced, the shape of the root mean square (rms) velocity profiles are similar. At higher drag reductions, above approximately 40%, the flow enters the HDR regime for which the slope of the log-law is dramatically augmented and the Reynolds shear stress is small (Warholic et al., 1999; Ptasinski et al., 2003). Despite a long history of research, this area has witnessed a wave of recent advances that pushed the boundaries of our knowledge. These developments, which mostly occurred over the past ten years, were largely triggered by the shift of focus from ensemble flow statistics of turbulence to its dynamical diversity, intermittency, coherence, and transitions between different flow states. In the current study, the mean and fluctuating velocity profiles, as well as coherent structures modified with the drag-reducing polymer solution, are studied. Measurements are conducted in a homogenous polymeric TBL and the effect of polymer and flow properties on mean and instantaneous flow statistics are analyzed and discussed respectively.

2.3 Review on Mean and Fluctuating Velocity Profiles

The fact that the general structure of turbulent flow velocity profile is a spatiotemporal superposition of mean and fluctuating velocities makes it important to study the two, statistically distinct, velocity domains. Such a spatiotemporal decomposition was first introduced by Reynolds in 1895, which consequently led to the formulation of Reynolds Averaged Navier Stokes equation (RANS). A quick review of this equation is sufficient to imply the importance of studying the flow statistics in wall-bounded turbulence. In particular, it is important to see the evolution of velocity statistics as regions further away from the wall are realized. Such a statistical analysis also helps to relay how the near-wall events, may it be in the sense of time, length or velocity, scale with the local characteristic events. Such scaling helps retrieve the physical phenomena involved in the complex sequence of events that govern the near-wall region, where the bulk of the change of streamwise velocity in the wall-normal direction occurs (Prandtl, 1904). Although this dissertation concentrates on the polymeric induced changes to the two velocity profiles, it is necessary for the prospective building purposes that the statistical features of the Newtonian flow be formally introduced to the reader. This is done in the first sub-section, following which, a brief overview is given of how polymer additives modify the near-wall velocity profiles in the classical sense. This section is then concluded by presenting the modern-day arguments over the velocity profiles, which tend to deviate from the classical notion. The deviations between the classical and modern-day view are discussed in light of the literature, which provides the motivation for the current study.

2.3.1 Newtonian near-wall velocity profiles

The matter of investigating the Newtonian near-wall velocity profiles dates back to the first meaningful analysis presented by Ludwig Prandtl (1904) and von-Karman which resulted in the classic log-law $(U^{+} = ln(y^{+})/\kappa + B)$. This has been discussed at length in Schlichting (1960). Thereafter, several works, such as that of Laufer (1951), Eckelmann (1974), and Purtell et al. (1981), have extensively tested the wall-normal variation of the mean flow velocity in the streamwise direction to its logarithmic functional form conformance. Most notably, the attempt of Coles (1962; 1968) was to evaluate the constants of the proposed law. Following such work, it was believed for several decades that the value for the von-Karman constant in the log-law was a constant at 0.41. However, more recent findings place it as low as 0.38 (Nagib et al., 2004), while others place the value to be as high as 0.45 (Zagarola & Smits, 1998). Such a varying nature of the value for von-Karman constant, traditionally assumed to be constant, was first pointed out by Simpson (1967, 1970), who argued that such a variance in the value of the von-Karman constant is subject to the Reynolds number. Moreover, such modifications to the values of the von-Karman constant have also been found to be extremely sensitive to the pressure gradients. This means that even for a mildly varying pressure gradient, the von-Karman constant fluctuates (Nagib & Chauhan, 2008; Bourassa & Thomas, 2009; Oweis et al., 2010). However, for a TBL that evolves under a truly zero-pressure gradient, there is significant evidence that the von-Karman constant adopts a value of 0.41.

There is even less of a consensus on the universality of the slope-intercept of the log-law. While traditional estimates, such as that of Coles (1968) place its value in the 4.9 to 5.1 range, recent claims of it having a value, ranging from 4.0 to 10, have surfaced (George, 2007). As can be seen, by mere mention of a few highlighted works, there still exists a significant difference of opinion on this matter. Moreover, there is yet another school of thought (Ching et al., 1995) that opposes the log-law formulation of mean velocity statistics. Instead, they insist on adopting a power-law form of the mean velocity profiles that do, on the contrary, exist below the given Reynolds number threshold (discussed below). Rest assured, given this phenomenological difference of opinion, the existence of the log-law and that its functional form adopts a scaling with the inner variables, is a well verified and empirically established result, characteristic of truly turbulent flows implying that it (log-law) is a trait for turbulent flow in the limit of infinite Reynolds number (Oweis et al., 2010).

Another important issue with regard to the log-law is its dependence on the Reynolds number. The underlying assumption of the log-law formulation is that there is a sufficiently large separation between the large and small scales. This makes the overlap region (log-law) arguments strictly tenable in the limit of infinite Reynolds number. For a sufficiently low Reynolds number flow, it has been observed that the log-law ceases to exist. Coles (1962) analysis of the wake component indicates that at Re_θ = 600, the log-layer vanishes altogether. Yet another study conducted by Bandyopadhyay and Ahmed (1993) indicates that such a vanishing of the log-layer appears at Re_θ = 425. Regardless, above the given threshold momentum thickness based Reynolds number, the existence of the log-layer has been extensively tested and verified. The fact that the log-layer ceases to exist below a certain threshold could be explained by associating such non-existence of log-layer due to the remnants of the transitional behavior of TBL. However, the matter of its Reynolds number dependence is a very critical and important subject of investigation for TBL studies. Regardless of such contending issues, the fact that the log-layer becomes more and more prominent as higher Reynolds numbers are achieved hints that the log-layer has an active role to play and is, therefore, an integral part of a truly turbulent flow.

Yet another matter of concern with regard to log-layer is the spatial bounds of its existence in the TBL. Recent high-Reynolds number findings on this issue (Marusic et al., 2013) show that conservative limits for the log-layer are $3.0\ (Re_\tau)^{0.5} < y^+ < 0.15\ (Re_\tau)$. It is these bounds for the log layer that the current study adheres to. Respecting the differing opinions on the values of the log-law constants, for the sake of this study and for the purpose of comparing the results presented herein with the established literature, the values of the von-Karman and slope-intercept constants in the log-law are taken to be 0.41 and 5.0 respectively. Moreover, for the sake of satisfying the arguments on the existence of the log-layer, it has been ensured that baseline testing conditions conform to the most conservative of the estimates in this regard.

In contrast to the mean flow, measurements on the fluctuating flow field have been, and still are, a more challenging task. While issues with probe resolution have marred the success of such attempts (Wei & Willmarth, 1989; Lofdahl et al., 1992), growing technological advances have made it possible to resolve such small scale fluctuations to a reasonable accuracy (Metzger et al., 2001). Historically, as has been the case with the mean velocity profiles, the attempt of scaling the fluctuating quantities with the inner variables depicts the classical idea. To this end, the most extensively tested data is that of the streamwise velocity fluctuations, which have been reported on a number of occasions (Purtell et al., 1981; Mochizuki & Nieuwstadt, 1996; De Graaff & Eaton, 2000; Metzger et al., 2001; Morrison, 2007). On almost all accounts, it has been observed that while the streamwise fluctuations collapse universally on inner variable scaling within the viscous sublayer, as the outer region (here refers to log-layer and beyond) of the boundary layer is realized, such a scaling, unlike that of the mean velocities case, fails to collapse the streamwise fluctuations. In fact, it has been observed in all of the studies mentioned above that the fluctuating streamwise velocity profiles appear to be some unknown function of the Reynolds number. However, one consistent finding amidst such baffling observations is that of the location of the peak streamwise velocity fluctuation. As Mochizuki and Nieuwstadt (1996) and Gad-el-Hak et al. (1994) conclude, this location appears to be consistently between $12 < y^+ < 15$. Moreover, within the range of low

Reynolds number regime (i.e. $1000 < Re_\theta < 6000$), such fluctuations appear to be in a very narrow range that is within the measurement uncertainty (Mochizuki & Nieuwstadt, 1996).

Another statistically relevant quantity is that of the wall-normal velocity fluctuations. Like the streamwise velocity fluctuations, these too have been a subject of much scrutiny. Many accounts, notably that of Gad-el-Hak et al. (1994) provide an excellent review on the subject to show that in general, the wall-normal velocity fluctuations show a progressively increasing magnitude with increasing Reynolds number, but that their magnitude in the relative sense with the streamwise fluctuations are significantly lower. Again, it is mentioned that within the regime of low Reynolds number, the variation in the peak value of wall-normal fluctuations is mild, but unlike the streamwise fluctuations, their peak value persists for a larger range of y^+ values.

The general structure of the RANS equation further shows that in addition to the wall-normal and streamwise fluctuations, the correlation of these two quantities, otherwise termed as the Reynolds shear stress, is another important quantity from the flow statistics perspective that affects the mean motion. Reynolds stress $=\rho \langle u_i u_j \rangle$, where ρ is density, $\langle \quad \rangle$ donates as ensemble average and u is fluctuating velocity component. The data of Wei and Willmarth (1989) show that these stresses peak in the buffer region of the TBL. Further investigations (Panton, 1997) and the more recent investigation of Volino and Shultz (2018) attest to the same observations. More interestingly, all these investigations show that the wall-normal fluctuations and the Reynolds shear stress scale well with the inner variables within the inner region of the TBL. Moreover, the inner wall variable normalized magnitude of these Reynolds stresses continue to show a monotonic trend with increasing Reynolds number. This indicates that such statistical parameters are emblematic of the underlying processes that contribute to the generation of skin friction, which is the real focus of this dissertation.

2.3.2 Classical and modern-day view of polymer modified flows

Having mentioned the statistical structure of Newtonian flow at length, now the focus shifts to the modified flow structure of the polymeric flows. The motivation for the current investigation finds its roots in the difference between the classical and the modern-day view of how polymer additives modify the flow structure. Virk (1971, 1975) showed that the primary effect of polymer additives on the velocity structure is to enhance the physical dimensions of the buffer layer while modulating the extent of the log-layer. The natural impact of such modification has been traditionally associated, in the velocity fields, by the shifted log-law intercept value, while keeping the von-Karman value constant at 0.41. However, the more recent investigation of Elbing et al. (2013) showed that while this may be partially true in the mean velocity realms, it is not a universal behavior of the polymer-modified TBLs. In particular, when higher values of drag reduction (> 40%) are realized, there is a significant modification observed with the von-Karman constant, in that it continues to decrease. This may be thought of as an analogy between the observed increase in the von-Karman constant (Zagarola & Smits, 1998), whereby an increasing Reynolds number indicates increasing skin friction drag. It is this discrepancy between the modern-day view and the classical view of the polymer-modified turbulent flows that spark the current study. It is, however, important to note that observation of Virk (1971, 1975) on the universal asymptote of the MDR is a well-tested and verified result in PDR. This asymptotic profile, otherwise called the Virk's ultimate profile, is a logarithmic profile that is steeper than the Newtonian one by nearly a factor of 5, $U^{+} = 11.7\ln(y^{+}) - 17.0$. Such clear variations in the mean profile is an indication that polymer additives interfere with the general flow structure, such as to re-route the flow energetics to re-channel the flow of energy from the mean to fluctuating flow fields.

Since the dominating momentum transfer in turbulence is due to Reynolds stresses, it should be well established by now that any drag reduction process must create a change in the basic structure of TBLs; drag reduction calls for modifying the momentum exchange process between the outer and inner regions of TBLs. Initial investigations on polymeric flow boundary layer structure were done as early as Wells and Spangler (1967) and Wu and Tulin (1972) to determine that polymer additives are actively modifying the near-wall turbulent flow statistics. Reischman and Tiederman (1975) further investigated to find that polymer additives had a pivotal effect on the mean velocity profiles in the buffer zone ($10 < y^+ < 100$) confirming what Virk (1975) observed. Later on, Tiederman et al. (1985) found that polymer additives did not affect drag reduction if entirely confined to the viscous sublayer. However, they do conclude that when the polymer additives interact with the viscous buffer layer, drag reduction comes to effect. Investigations of such sort provided mounting evidence indicating that the buffer layer is central to the structure of turbulence and any reduction in drag must significantly alter its mechanics.

One of the convincing and reliable measurements of fluctuating flow fields were reported in Warholic et al. (2001). It convincingly showed that while streamwise velocity fluctuations in the polymeric flow show little or no variation in the wall-normal direction, as compared to their Newtonian counterparts, wall-normal and Reynolds shear stress are significantly dampened. This observation has been, thereafter, confirmed on multiple occasions (Dubief et al. 2004; Warholic et al., 1999; 2001). An excellent review of this can be found in White and Mungal (2008), as well as Xi (2019), while a more specific and focused argument can be found in Dubief et al. (2004). Tackling this problem from the various rheological models such as the Oldroyd-B model and FENE-P model, Min et al. (2003a; 2003b) showed the necessary modifications to be made to the equations employed to depict the effect of polymers on flow properties at MDR. Furthermore, the reduction in the velocity fluctuations has been numerically confirmed and associated with the resulting polymeric stresses, as previously mentioned in Gyr and Bewersdorf (1990). More recent corroboration of such results on the fluctuating velocity field modulation can be found in Shahban et al. (2018) and Mohammadtbar et al. (2017).

2.3.3 Motivation for study structure of turbulence in PDR.

As has been discussed above, the prime difference between the modern-day view and the classical view is that while the latter holds to be true, it is only true partially; partial in the sense that it fails to explain the observations made for values of drag reduction greater than 40% (HDR) (e.g., works of White et al., 2012 and Elbing et al., 2013). The deviations from classical view has even extended to LDR (< 40% DR) for drag reduction as low as 15% (Elsnab et al., 2019). It is this inconsistency that provides the motivation for diving into the statistical framework of the problem. It is clear that the observed differences imply that a relevant polymer parameter is at work to create these observed deviations. Therefore, it is instructive to observe these differences with the polymeric property that essentially captures the effect of polymer-turbulent flow interaction; the Weissenberg number (*Wi*).

2.4 Review on Coherent Structures

The mathematical structure of the fundamental equation on turbulence (i.e. RANS equation) shows that cross-gradient mixing and momentum transfer processes are an integral part of the near-wall turbulence. This also helps to make the deduction that turbulence has a distinct structure that is responsible for its established properties. Such diffusivity of momentum also shows that the inner and outer regions of TBLs are perhaps interconnected and so the activities of the one tend to influence the activities in the other. Such a conjunctional sequence of events is one of the fascinating properties of turbulence and is exploited in many flow control applications, including polymer drag reduction. Studying the mechanism of polymer drag reduction means to seek an answer on how the polymer additives modify the basic structure of turbulence, which in turn means understanding the basic structure of turbulence in Newtonian flows. There have been various attempts expended on this issue, the most important of which are mentioned below. The view painted here focuses on the topology of the near-wall TBL flows. This means, the current work focuses on the physics of the problem, rather than its mathematics, although mathematics (statistical details) have been primarily used for the inferences made. This serves the motivational phase of this part of the study.

2.4.1 Newtonian coherent structures

It is natural to conduct the current study, given the importance of statistics of near-wall turbulence (discussed above) and the fact that near-wall turbulence also happens to have a distinct structure. There have been several seminal works done in this regard, the earliest and perhaps the groundbreaking work was of Kline et al. (1967). Their flow visualizations revealed distinctive, spanwise distributed streaks of low momentum fluid in the viscous sublayer. Kline et al. (1967) elaborated on the concept proposed by Lighthill (1963) in which the wall-normal velocity fluctuations were thought to be impressed on a spanwise vorticity element, dividing it into stretched and compressed segments. These segments then produce spanwise variations of velocity, hence effecting the observed low-speed streaks.

This work then prompted a series of probe-based and visual-based investigations, most notable of which was that of Kim et al. (1971), Clark and Markland (1971) and Grass (1971). Such investigation further revealed the existence of counter-rotating pairs of quasi-streamwise and transverse vortices, complimented by a set of near-wall events, known as “sweeps” and “ejections”, terminating in highly chaotic “bursting” events. All these investigations were in effect confirming the physical insight of Theoderson (1952). This was shortly followed by investigations of Hinze (1975) that proposed the formation of an unstable shear layer due to the fluid lift-up between the vortex legs. Although the work of Blackwelder and Eckelmann (1979) confirm similar observations, it was the work of Head and Bandyopadhyay (1981) that gave the first meaningful insights and convincing evidence for such a structural make-up of the near-wall turbulence. Like the rest, they leveraged the physical insight of Theoderson (1952), to shed more light on the evolutionary dynamics of the near-wall structures. Firstly they concluded that these structures get stretched and tend to be pushed towards the wall by the mean flow which intensifies the vorticity, causing self-induced velocities to raise these structures through the boundary layer until they reach about a 45° orientation (with respect to flow direction), at which point these opposing actions reach equilibrium, thereby maximizing turbulence production, and then secondly, they also concluded that the outward growth of these structures is limited to the extent of the pre-existing strain field. Kline et al. (1967) provided a mechanistic illustration of this lifting up process, which that illustration has been reproduced in the Figure 2-2.

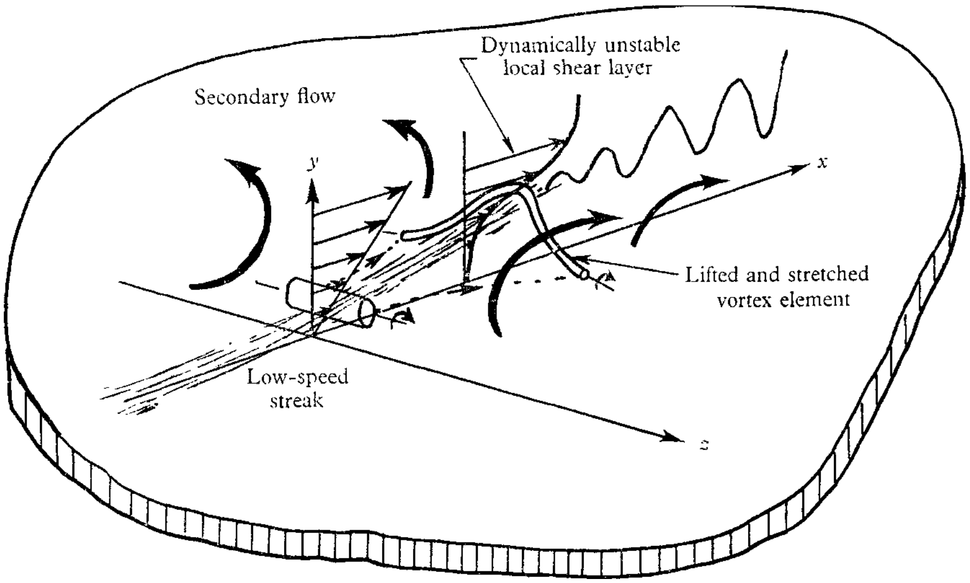

Figure 2-2 Illustration of vortex lift-up associated with an unstable shear layer formation. This mechanistic illustration was reproduced from Kline et al. (1967).

On the parallel, as computational capacities enhanced (Blackwelder & Eckelmann, 1979), the observed phenomenon found their mathematical guarantee. Such developments were leaning in favor of the coherent structure theory. This inspired Smith (1984) to give a comprehensive model capturing the essential kinematics and dynamics of the near-wall turbulent processes. A brief review of that model is in order for the sake of completeness and developing a relevant context to explain the upcoming observations. The low-speed streaks in the near-wall region grow until a perturbation of sufficient strength impresses a local adverse pressure gradient, resulting in localized flow deceleration. The most likely victim of such decelerations is the low momentum fluid streaks because of their inherent inability to negotiate with the adverse pressure gradients. Inflectional profiles form at the low and high-speed fluid interface in the near-wall region, setting them to oscillate under the background perturbations offered by the chaotic state of turbulent flows, thereby oscillating the low-speed streaks. These oscillations are then translated to perturbations in the spanwise vortex sheet encompassing the streaks. This ultimately affects vortex concentrations rolling up and taking shape of the much-observed hairpin vortices. The growth of the hairpin, from here on, is governed by the antagonistic set of events; stretching of vortices by the mean shear flow and the self-induction effects of the hairpin structure. The stretching of the hairpin legs (appearing as counter-rotating vortex pair in the near-wall region) pumps the fluid away from the wall, while gathering more of the slow fluid between them as a consequence of vorticity intensification. This concept was illustrated in Robinson (1991), which has been reproduced here in Figure 2-3. This lifting up of the fluid constitutes the final stages of the burst event as described in Kim et al. (1971).

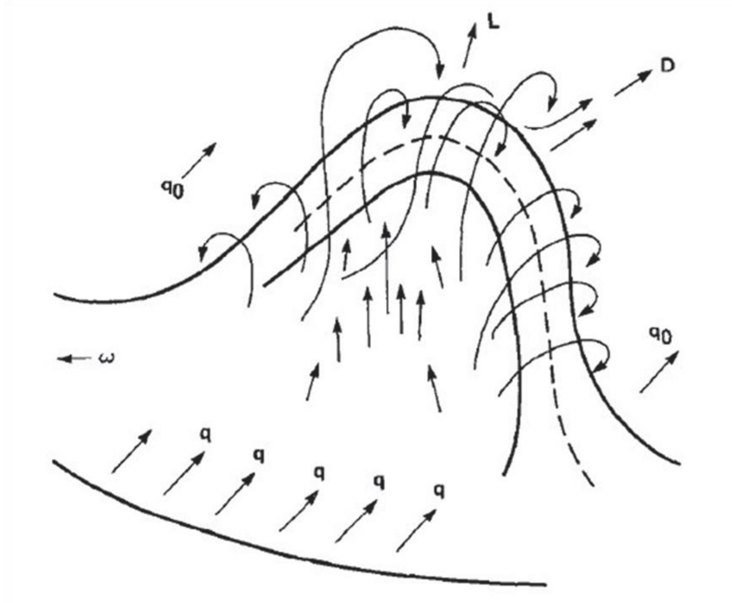

Figure 2-3 Illustration from Robinson (1991) that is a conceptualization of the sweep and ejection events.

More recent investigations, like that of Adrian et al. (2000), have shown that the protruding structures are crucial for the interactive mechanism taking place in the overlap region. This, as an example of Newtonian coherent structures, is illustrated in the Figure 2-2 and Figure 2-3. These figures tend to show that these structures convect at the local mean velocity while evolving in time and space simultaneously. Complementing this model, a statistical survey conducted by Robinson et al. (1989) showed that 70% of the vortices were found in the near-wall region, $y^+ < 100$, with the most intense of them residing within $y^+ < 75$, were streamwise oriented legs of vorticies and 80% of the vortices plotted in the region $80 < y^+ < 180$ were spanwise oriented heads of vorticies. The survey also revealed that the spanwise oriented heads were thicker in diameter as compared to the streamwise vortices; 74% of the spanwise vortices had their diameters between 30 and 70 viscous units and 73% of the streamwise vortices had their diameters between 10 and 40 viscous units.

2.4.2 Polymeric coherent structures

The observations of Toms (1948) would suggest the polymer additives eye for modifying the momentum exchange process between the outer and inner regions of TBLs. Given what has been stated above with regard to Newtonian structures, the streamwise vortices must be altered in geometry, orientation, position, and circulation intensity to affect their contribution to the ejection, sweep, and bursting processes. One of the earliest investigations done with respect to how polymers modify the near-wall turbulent structures was that of Wells and Spangler (1967) and Wu and Tulin (1972). They determined that polymer must be in the near-wall region to effect drag reduction. Reischman and Teiderman (1975) further found that the polymer additives had a profound effect on the velocity profiles within the buffer layer. This indicated that polymers are active in buffer layer and they change the strcuture of turbulence which will be observed in log-layer. On the parallel, the flow visualizations of Achia and Thompson (1977) and Donohue et al. (1972) revealed the modifications to the sublayer structures; the spanwise spacing of the sub-layer low-momentum streak increased with increasing drag reduction. Following the model of Smith (1984), any modified kinematics and dynamics of sublayer streaky structures must affect the ejection and burst events. This was later on confirmed by Schmid (1984) who using “intensity of an event” summed up $\acute{u}\acute{v}$ over all three events to find that, at LDR, such mean intensities differed significantly for the ejection type events as compared to Newtonian flows. A similar conclusion was made for HDR. This offered more support to the observations of Tiederman et al. (1985) that polymer additives inhibit the break-up of low-speed streaks and therefore justify the reduced frequency of the burst events.

Discussing the rheological part of the problem, Gyr (2012) refers to the deficit of the Reynolds stress balance due to the shear and elongational process that alter buffer layer viscosity. Sibilla and Baron (2002) have studied this to computationally link such observations with the polymeric stresses. There has been considerable evidence to suggests that the elastic stresses, termed as a deficit in Reynolds stress balance, dampens the turbulent stresses. Gampert and Yong (1990) produced joint probability density function (JPDF) for the fluctuating wall-normal and streamwise velocities, normalized by the near-wall units, to demonstrate that polymer additives significantly enhance anisotropy in the fluctuating motions. The damping of the wall-normal velocity fluctuations is far more pronounced than the streamwise fluctuations, specifically in the buffer layer region of the boundary layer. Luchik and Teiderman (1988) further found that lower threshold $u'v'$ events in the second and fourth quadrants are damped whereas the higher threshold $u'v'$ events are unaffected. Gampert and Yong (1990) used the time fractions for all the four-quadrant events to characterize the effect of polymer additives on sweeps and ejections to find that these events are suppressed both in terms of their intensity and duration, specifically in the buffer layer region. The attenuated intensity of such events is a natural cause-and-effect type event following a decrease in vorticity and an increase in the size of the near-wall vortices, as predicted by the numerical computations of Gyr (2012).

To this end, such a detailed introduction serves both fundamental and motivational purposes and it substantiates the need for the current study. Much less is known about how the polymer chains modify the structures in the outer regions and their corresponding flow statistics, where significant velocity rise occurs at higher Reynolds numbers. A wide spectrum of structures in this region together with increasing Reynolds number make flow simulations for these regions excessively expensive. Recent investigations such as that of Escudier et al. (2009), White et al. (2012), and Elbing et al. (2013) have also shown that the mean velocity profiles in the log-layer in the HDR regime (i.e. DR > 40%), show trends deviating from that of the LDR regime. This indicates that polymer properties have a subtler role to play than flow properties. Therefore, their characterization is a must for complete and meaningful analysis, thus requiring the need for this study.

CHAPTER III

3 EXPERIMENTAL METHOD

3.1 Test Facility and Model

3.1.1 Water tunnel design

Typical commercial recirculating water tunnels achieve a momentum thickness-based Reynolds number (Re_θ) on the order of 10^3, which is slightly above that required for laminar to turbulent transition. The bounds of the log-layer have been estimated from high-Reynolds number experiments compiled in Marusic et al. (2013) to be

$$3.0\left({Re_\tau}^{0.5}\right) < y^+ < 0.15(Re_\tau). \tag{3.1}$$

The world's largest water tunnel, U.S. Navy Large Cavitation Channel (LCC) (Etter et al., 2005; Park et al., 2003) can achieve $Re_\theta \sim 10^5$, but the operation cost is extremely high. Consequently, facilities that can achieve ($10^3 < Re_\theta < 10^5$) are ideal for studying Reynolds number dependent turbulent phenomena, such as velocity profile modifications in drag reducing polymer solutions (White et al., 2012; Elbing et al., 2013), which was the primary specification for the current facility. The completed facility (schematically shown in Figure 3-1) bridges the gap between commercial water tunnels that are barely turbulent and the world's largest facilities (Lauchle & Gurney, 1984; Marboe et al., 1993; Park et al., 2003; Etter et al., 2005).

The design of the current facility was performed in 2014 (Daniel, 2014) and the installation and validation were conducted in 2016 (Farsiani & Elbing, 2016; Elbing et al., 2018). Here for completeness, is an overview of the water tunnel design, while the full details and analysis are in Daniel (2014). Design criteria for test-section specifications were (i) $Re_\theta \geq 10^4$, (ii) to maximize optical access, and (iii) to minimize inlet flow. Test-section design is driven by the application, operation range, and instrumental suite. The current facility focuses on modifications to canonical TBLs. The maximum length (~1 meter) was set to achieve the required rigidity, flatness, and surface smoothness without excessive costs. Momentum integral analysis with a 1/7th velocity profile on a zero-pressure-gradient (ZPG) flat-plate estimates the outlet boundary layer thickness ($\delta/x = 0.16 {Re_x}^{-\frac{1}{7}}$) to be ≥ 16 mm. Here $Re_x \left(= \frac{U_e x}{\nu}\right)$, is the downstream based Reynolds number, ν is the kinematic viscosity (~10^{-6} m^2/s), x is the downstream distance from the inlet, and U_e is the local freestream (external) speed. The TBL overlap region is unaltered from the log-law $(U^+ = ln\, y^+/\kappa + B)$ when the dimensionless acceleration parameter $K' = (\nu/U_e^2)\, dU_e/dx < 1.62 \times 10^{-6}$ (Patel, 1965). When pressurized $(p_{max} = 276 \text{ kPa})$, the acrylic walls have a maximum displacement of 115 μm (Daniel et al., 2015). The resulting local curvature has a negligible impact on the velocity profile but is nontrivial compared to viscous length scale (l_ν). Thus the wall location must be identified for each operating condition. The stainless steel frame has an average roughness height (R_a) of 0.8 μm. Converting R_a to Colebrook type roughness (k_c) (Schultz, 2002; Acharya et al., 1986) and noting $l_\nu \geq 2.0$ μm, the maximum $k^+ = \frac{k_c}{l_\nu}$ is 0.6 to 1.7. This is acceptable since hydraulically smooth is when $k^+ < 4$ and the majority of the TBL develops on the smoother acrylic windows.

Flow non-uniformity was mitigated with a tandem honeycomb/settling-chamber configuration, an 8.5:1 contraction, and gradual expansion in diffusers (Figure 3-1). The design/selection of the flow conditioning components assumed flow enters some distance upstream of the test-section with high turbulence and swirl. Swirl, which is difficult to remove, is generally mitigated with pressure-drop via a combination of screens, baffles, and/or honeycomb. Honeycomb was selected because screens in water tunnels typically need to be tightly meshed and can foul, resulting in variable tunnel performance.

The pump supplied the pressure differential (*Δp*) to overcome the system losses at the desired flow rate, which required an iterative design process. The volumetric flowrate (0.232 m^3/s) was readily available given the cross-section and maximum speed (10 m/s). A horizontal split case centrifugal pump (S10B12A-4, Patterson) with a 112 kW (150 hp) motor (MP44G3909, Baldor) was selected because it achieved the operating condition, had a low minimum flowrate, low cost, and compact design. Pump frequency is manually controlled with a variable frequency drive (VFD) with a digital display. The complete design details can be found in (Daniel, 2014; Elbing et al., 2018).

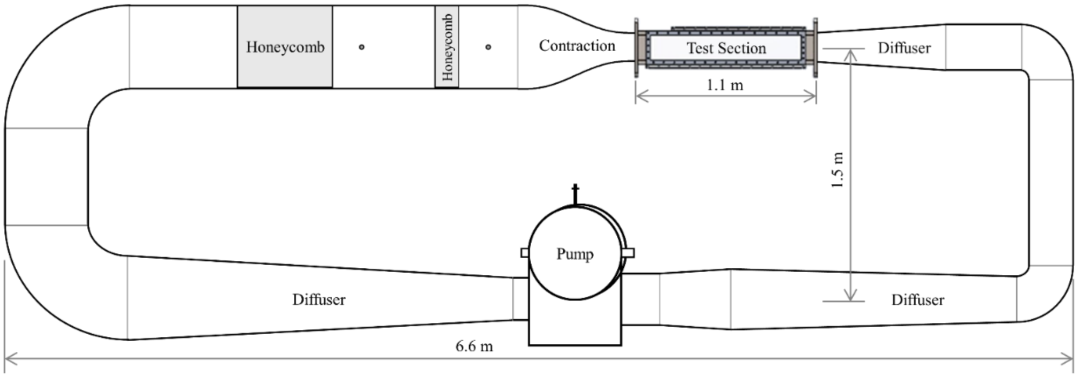

Figure 3-1. Schematic of the high-Reynolds number, low turbulence recirculating water tunnel. Ports downstream of honeycomb sections were for temperature and static pressure measurements.

The total volume (1.47 ± 0.04 m^3) was determined by comparing the changes in conductivity against an established calibration curve, which is explained in detail subsequently. A boundary layer trip (uniformly distributed 122 μm grit) at the test section inlet mitigated transitional effects on the tunnel walls. Measurements were acquired within the flat plate TBL that formed on the test section wall. The coordinate system used throughout the manuscript has the *x* origin at the test section inlet and extending in the downstream direction, the *y* coordinate increasing in the wall-normal direction with the origin at the test section centerline, and z extends in the spanwise direction completing a right-handed coordinate system.

The tunnel was filled with tap water with the top wall removed to vent the tunnel. Filling the tunnel was conducted very slowly for air scavenged purposes. There were pipes connected to at the highest points on each side of the tunnel, which were connected to a pressure vessel that was vented to ambient air to remove the trapped air while filling the tunnel. At the end of each set of experiments, the water was drained through two drainage ports at different heights. One of the drains was at the very bottom leg of the tunnel to ensure all the water was drained. A picture of the entire water tunnel is shown in Figure 3-2. Parts of this section have been published in Elbing et al. (2018).

Figure 3-2. Picture of the installed water tunnel with the pump/motor on the lower leg (in red) and the test section almost directly above on the pump/motor.

3.1.2 Flat plate test model

The test section top and bottom walls were used as the flat plate test model for the TBL studies (Chapters 5 and 6). Each wall was 1.1 m long with $154\ \mathrm{mm} \times 154\ \mathrm{mm}$ cross-sections. The test models were hydraulically smooth, as previously discussed, and made of acrylic for visualization purposes.

3.2 Water tunnel characterization

3.2.1 Total volume measurements

To study the effect of polymer properties on a TBL in a polymer ocean, the volume of the tunnel had to be determined. Most of the polymer parameters are concentration-dependent, which the uncertainty of polymer concentration can be minimized with a polymer ocean (a homogeneous polymer solution concentration through the entire tunnel). This can be done by uniformly mixing the polymer powder into the tunnel. However, knowing how much polymer is needed to achieve a given concentration in the tunnel requires an accurate measurement of the tunnel volume.

The sensitivity of electrical conductivity of water to the salt concentration was used to measure the tunnel volume. Here the rate of change in electric conductivity of the water/salt solution was established using different salt concentrations in a known volume. Then by noting the increase in conductivity with the addition of known quantities of salt, the mass and volume of an unknown reservoir (i.e. the water tunnel) can be computed. A portable conductivity meter (CDH-287- KIT) was used and the rate of conductivity change with salt concentration was measured in a known volume of a bucket with a mass (m) of 18.3 kg mixed with iodized salt (Morton Co). The test matrix for the conductivity calibration experiment is shown in Table 3-1. Proper stirring was applied to have a homogenous solution. Conductivity difference ($\Delta\sigma$) in μS/cm (micro-siemens per centimeter) versus concentration (C) in weight parts per million (wppm) was recorded to establish the calibration curve. Measurements were repeated three times to get the repeatability of the data and the averaged was used as the final calibration curve. The rate of conductivity change with added salt concentration was calculated to be $\Delta\sigma = 1.967C$.

Table 3-1. Test matrix for the conductivity versus added salt concentration calibration test in a known volume (bucket).

m_{add} (g)	m_{salt} (g)	C_{salt} (ppm)	σ (μS/cm^3)	$\Delta\sigma$ (μS/cm^3)
0	0	0	516	0
1.05	1.05	58.13	630	114
3.54	4.59	254.15	1015	499
1.48	6.07	336.10	1180	664
1.94	8.01	443.52	1391	875
2.05	10.06	557.03	1633	1117
2.18	12.24	677.74	1849	1333

The water tunnel was partially filled with water and a certain amount of salt was added to the test section through the open top wall. The top wall was installed and the tunnel fill completed. This step was very important to have the tunnel fully filled with water and get the exact concentration of salt. The solution was set for 3.5 hours to be homogeneously mixed throughout the tunnel. The time needed for the homogenous salt solution was determined previously by estimating the time it takes for dye being added to the water. The pump was operated at 10 Hz to circulate the water for three minutes. Two samples of water/salt solution were taken out from two different sections of the tunnel. The same solution conductivity values from two samples suggest an even distribution of salt in the tunnel. At the end of each trial, the water was fully drained and refilled with fresh water. The test matrix is shown in Table 3-2. *Changes in the conductivity with the addition of salt to the water tunnel and the resulting estimate of the mass and volume of water in the tunnel.* Once the concentration and mass of salt were known, the mass of water could be determined. By having a density of water at the test temperature, the volume of the unknown reservoir (water tunnel) can be determined. The volume of the tunnel was averaged from three repeated tests and determined to be 1.468 m^3.

Table 3-2. Changes in the conductivity with the addition of salt to the water tunnel and the resulting estimate of the mass and volume of water in the tunnel.

Tunnel Calibration					
m_{salt} (g)	σ ($\mu S/cm^3$)	$\Delta\sigma$ ($\mu S/cm^3$)	C_{salt} (ppm)	m_{tunnel} (kg)	V_{tunnel} (m^3)
0	507	0	0		
120	678	163	83.551	1436	1.439
120	667.5	160.5	82.270	1459	1.462
80	616	106	54.334	1472	1.475

3.2.2 Pump characterization

Water tunnel pump performance was compared with the design criteria by running it at different speeds and measuring the free stream flow velocity in the test section. The initial test was with the pump at maximum speed (30 Hz). Centerline velocity in the middle of the test section was measured with particle-image-velocimetry to be 10 m/s. This was in an excellent agreement with the performance estimated from tunnel design and pump selection. The pump calibration curve was plotted by getting the data at different conditions. The freestream velocity was measured in the center of the test section at three downstream locations (x = 0.3, 0.56 and 0.94 m) for four pump frequencies (5, 10, 20 and 30 Hz). These results were originally presented in Farsiani and Elbing (2016) and provided in Figure 3-3, which also shows the linear best fit curve for each streamwise location. Error bars were neglected since they were smaller than the markers with the standard deviation of the mean being <1% of the mean. Standard deviations of free stream speeds for a couple of conditions are shown in Table 3-3. These results demonstrate the linearity between the tunnel speed and the motor frequency as well as the flow acceleration within the test section due to boundary layer growth on the walls. The boundary layer growth will be discussed subsequently, but at this point, it is noted that fitting of this data allows estimates of the velocities at the inlet (x

= 0 m), center (x = 0.5 m) and outlet (x = 0.95 m; the maximum downstream distance where PIV measurements could be acquired). These locations were selected due to their practical usage in designing experiments. The estimated velocities and the corresponding curve fits are provided in Table 3-4.

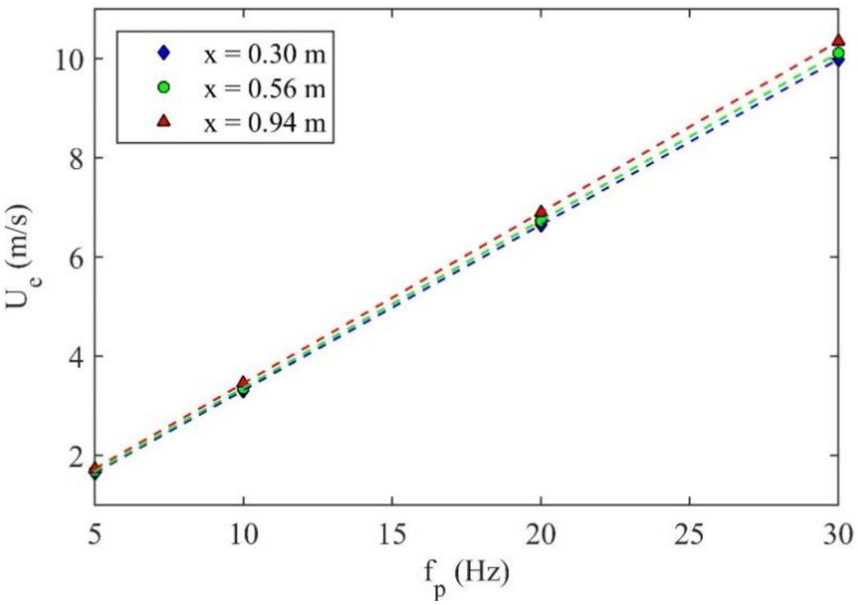

Figure 3-3. The average freestream velocity U_e (i.e. outside of the boundary layer) as a function of pump motor frequency (f_p) measured at three streamwise locations (x). The dashed lines are linear best-fit curves to the data at each streamwise location.

Table 3-3. Mean (avg) and standard deviation (std) of the velocity profiles outside of the wall region.

Pump frequency	x = 0.3 m		x = 0.5 m		x = 0.9 m	
f_p (Hz)	Avg (m/s)	Std (m/s)	Avg (m/s)	Std (m/s)	Avg (m/s)	Std (m/s)
5	1.65	0.003	1.67	0.0035	1.70	0.005
7	2.31	0.004	2.35	0.005	2.36	0.015
10	3.31	0.012	3.35	0.005	3.42	0.019

Table 3-4. Computed velocities and the corresponding best-fit curves at the inlet, middle and outlet of the test section.

		U_e (m/s)				$U_e = m\,f_p + b$	
	x (m)	$f_p = 5$ Hz	$f_p = 10$ Hz	$f_p = 20$ Hz	$f_p = 30$ Hz	m (m s^{-1}/Hz)	b (m/s)
Inlet	0.00	1.61	3.24	6.52	9.80	0.3277	-0.0348
Mid	0.50	1.67	3.35	6.72	10.1	0.3363	-0.0106
Outlet	0.95	1.73	3.45	6.90	10.3	0.3442	0.0101

The manufacturer performance curve for the pump is shown in Figure 3-4, which is consistent with the motor power calculations that were based on the pressure loss estimates. The pump was designed such that at a motor frequency of 30 Hz the test section speed would be 10 m/s. Based on this calibration, at a pump angular speed of 30 Hz, the velocity would be 10.2 m/s. Thus, current estimates show only a 2% deviation between the target design condition and the expected maximum tunnel speed. This is an exceptionally good agreement given that a factor of 3.2 was applied to the calculated losses within the tunnel. This was done during the design phase.

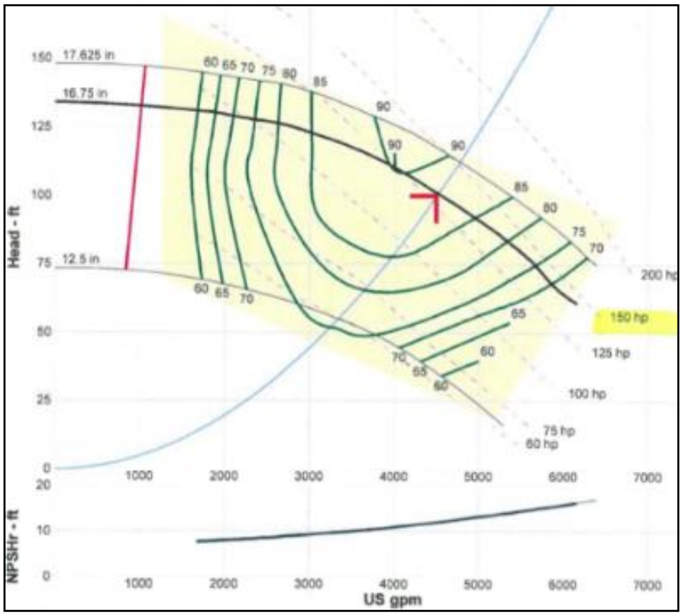

Figure 3-4. Manufacturer pump curve for the centrifugal pump used with the water tunnel.

3.2.3 Inlet turbulence

One of the most important characteristics of the flow quality in the water tunnel is the level of turbulent intensity within the test section. To check the quality of the flow, free stream turbulence intensity should be measured near the inlet. The freestream turbulence at the test section inlet was measured with hot-film anemometry (HFA) sampled at 500 Hz. Spectral analysis was used to provide information about how the energy of the signal is distributed with respect to frequency. By using a fast fourier transform (FFT), the data can be transformed to the frequency domain. This analysis was performed with commercial numerical computing software (Matlab, Mathworks Inc.) To plot the velocity in the frequency domain, the absolute value of the FFT was used to calculate the magnitude, or amplitude, of the velocity array. The energy $E(f)$ can be determined by dividing power by the frequency. The single-sided power spectrum in the time domain $S_{uu}(\omega)$ was computed at pump motor frequencies (f_p) between 1.5 and 4.5 Hz. The measurement duration was 60 seconds. The sample duration was divided into 60 one-second samples, which the FFT was calculated for each one-second sample and the results are the average of all the segments.

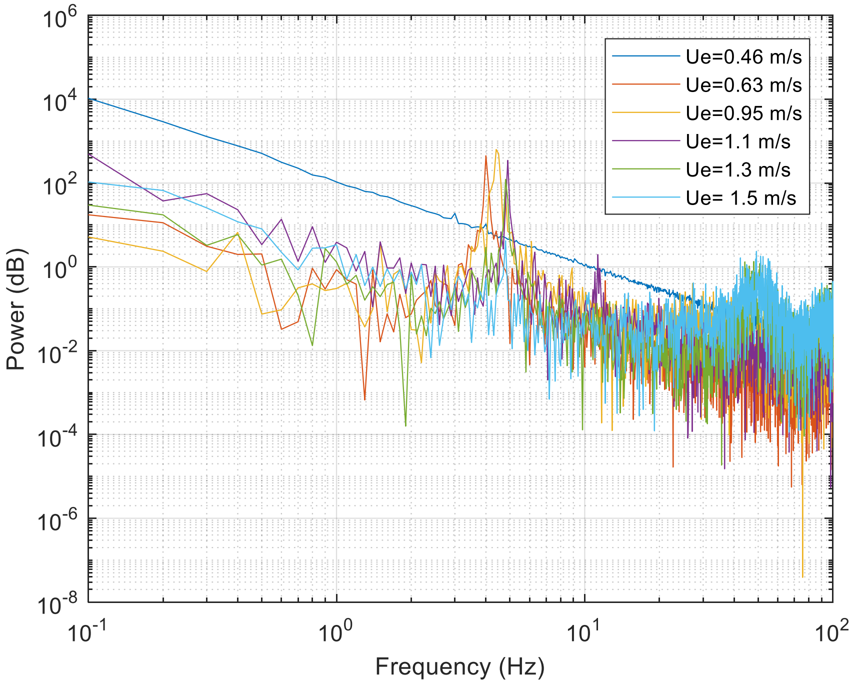

Figure 3-5. Power spectrum versus frequencies over the test range of pump frequencies (1.5 - 4.5 Hz).

In Figure 3-5 the raw spectra showed peaks at low (~5 Hz) and high (≥ 65 Hz) frequencies, which was the frequency spectrum at different pump speeds versus the range of frequencies. The frequency spectrum was transformed to the wavenumber spectrum utilizing Taylor's frozen turbulence hypothesis $kU \approx \omega$; $S_{uu}(k) \approx US_{uu}(\omega)$. This was performed in order to use the traditional turbulence scaling for high-Reynolds number isotropic turbulence (i.e. Kolmogorov's theory of 1941; K41). Here k is the wavenumber $\left(k = \frac{2\pi}{\lambda}\right)$, λ is the wavelength, U is the mean convection velocity, ω $(=2\pi f)$ is the angular frequency, and f is the temporal frequency. K41 suggests that $S_{uu}(k) = g(\varepsilon, \nu, k)$, which dimensional analysis provides the scaling law that $\frac{S_{uu}(k)}{(\nu^3 \varepsilon)^{\frac{1}{4}}} = \varphi(k\lambda_k)$. Here g and φ are unknown functions, ε is the dissipation rate of turbulent kinetic energy (TKE) per unit mass, ν is the kinematic viscosity, and $\lambda_k = (\nu^3 \varepsilon)^{\frac{1}{4}}$ is the Kolmogorov length scale. Noting that the dissipation rate of TKE must be equal to the rate that energy is supplied to the turbulence, ε, is estimated noting that the production rate should scale with the outer variables such that $\varepsilon \propto \frac{U_e^3}{L}$, where U_e is the freestream velocity and L is the height (or width) of the square cross-sectional area of the test section. The test section inlet turbulence data using this scaling is provided in Table 3.5.

Table 3-5 Summary of the unfiltered u_{rms} and the associated turbulence level at each pump frequency tested.

f_p (Hz)	1.5	2.0	2.2	2.5	2.7	3.0	3.5	4.0
U_e (m/s)	0.46	0.63	0.69	0.79	0.86	0.95	1.1	1.3
u_{rms} (mm/s)	0.8	2.2	1.2	1.0	1.2	5.1	6.1	5.1
TI	0.16%	0.35%	0.17%	0.13%	0.14%	0.53%	0.55%	0.39%

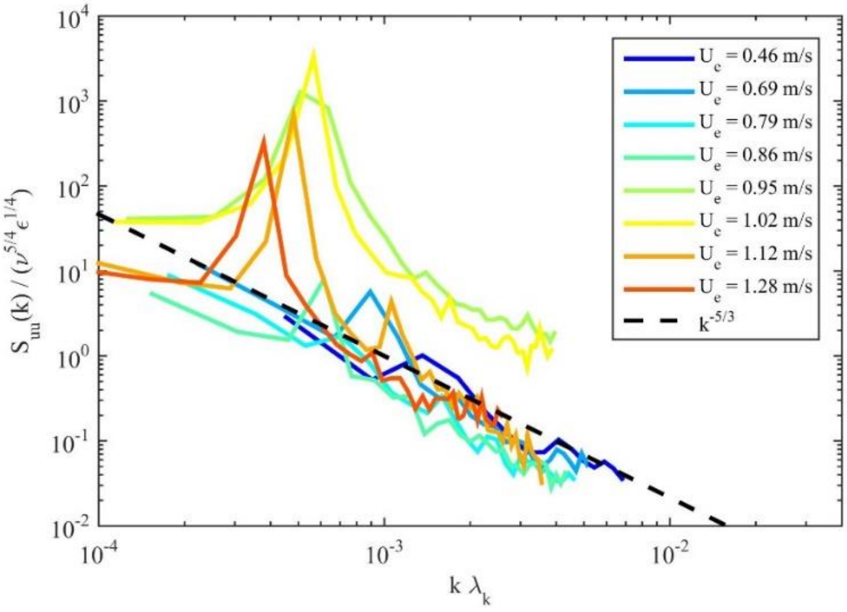

Figure 3-6. Power spectrum at the test section inlet over a range of speeds scaled using traditional isotropic turbulence scaling applying Taylor's frozen turbulence hypothesis to the HFA data. The dashed line shows the famous $k^{-5/3}$ slope from K41 for reference.

Here it is useful to estimate the expected range of turbulent scales, which the largest eddies should scale with the test section cross-section (L = 152 mm) and the smallest scales are on the range of the Kolmogorov length scale ($14.5 \leq \lambda_k \leq 27.5$ μm). With four orders of magnitude separating the production and dissipation ranges, it is expected that the current results should have a measurable inertial range where the spectra are independent of viscosity ($S_{uu}(k) \propto \varepsilon^{\frac{2}{3}} k^{-\frac{5}{3}}$). This is observed in Figure 3-6 with the dashed line added to indicate the famous $k^{-\frac{5}{3}}$ slope predicted for the inertial range in high-Reynolds number isotropic turbulent flow. It is important to note that the data has been truncated to omit frequencies above where Strouhal shedding ($St \equiv f_s d/U_e$) is known to influence the HFA measurement, where f_s is the shedding frequency and d is the diameter. The HFA support shaft diameter was 6.3 mm, which gives a nominal St ~ 0.21 over the corresponding Reynolds number range ($2.9 \times 10^3 \leq Re_d = \frac{U_e d}{\nu} \leq 8.1 \times 10^3$) (Roshko, 1961). The corresponding shedding frequencies for the range of test speeds was $22 \leq f_s \leq 50$ Hz. For each test speed, these shedding frequencies were close to the frequency where the spectra deviate from $k^{-5/3}$ slope. Consequently, data above the shedding frequency have been omitted from the plot, which was below the high frequency peaks (≥ 65 Hz). The higher frequency is likely due to the rigidity of the support structure and its cantilevered configuration, but further investigation was not performed since it was known that the shedding frequency already had contaminated the data and was no longer specific to the tunnel performance.

The final observation from the spectra is with regards to the low-frequency peaks observed at pump frequencies between 3 and 4 Hz but was not present at lower or higher speeds (4.5 Hz was tested but omitted since the shedding frequency contaminating nearly the entire inertial range). This is due to a natural frequency of the pump being excited between 3.3 and 3.4 Hz, in which the structural oscillations appear to be influencing tunnel performance near these frequencies. Consequently, during experimental test planning the range of 3 to 4 Hz should be avoided since the influence of the structural vibrations impacts these speeds. The root-mean-square velocity (u_{rms}) and the corresponding turbulence intensity (*TI*) for each speed tested is provided in Table 3-5.

Note that the reported u_{rms} is without any filtering of the data (i.e. these results include the effects of Strouhal shedding and impact from the natural frequency of the pump). Thus the average TI of ~0.3% is an upper limit of the expected turbulence level at the test section inlet. A bandpass Butterworth filter with a cut off frequencies of 8 Hz and the corresponding Strouhal based shedding frequency reduces the average TI to ~0.13%. Water tunnels are generally considered low-turbulence facilities when the inlet condition is below 1%, thus the current facility is considered a low-turbulence, recirculating water tunnel.

3.2.4 Empty test section mean velocity

As discussed above, the low turbulence level confirms the satisfying flow quality in the test section. However, the other measure of the quality of the flow in the test section is the velocity uniformity. The quality of the flow could be shown with the flatness of velocity profiles for the flow outside of the wall boundary layers. The boundary layer forming on the top and bottom of the test section is desired to be symmetric. This is determined by velocity profiles and boundary layer thickness measurements. Overlaying the velocity profiles from the top and bottom sections at the same locations along the test section and small standard deviation from the averaged velocities proves the symmetry of velocity profiles on each wall.

The mean velocity profile near the center of the test section (x ~ 0.5 m, z = 0 mm) was acquired over a range of pump frequencies (f_p = 5 to 30 Hz). The same field-of-view (FOV) was used for these measurements, so the profiles are composed of three independent measurements acquired either at the top wall, bottom wall, or the middle of the test section. These profiles scaled with the external velocity (U_e) and the channel height (H) are provided in Figure 3-7. From this figure, it is apparent that the velocity profile is relatively flat through the core (center) of the test section. The U_e determined from the three measurement positions (top, bottom, and middle) can also be compared to quantify the deviation. The maximum standard deviation observed at any speed tested was 1.3% of the mean, which is comparable to the PIV uncertainty. Thus, there is negligible mean shear within the test section. Also from Figure 3-7, the symmetry of the velocity profiles on the top and bottom walls can be observed.

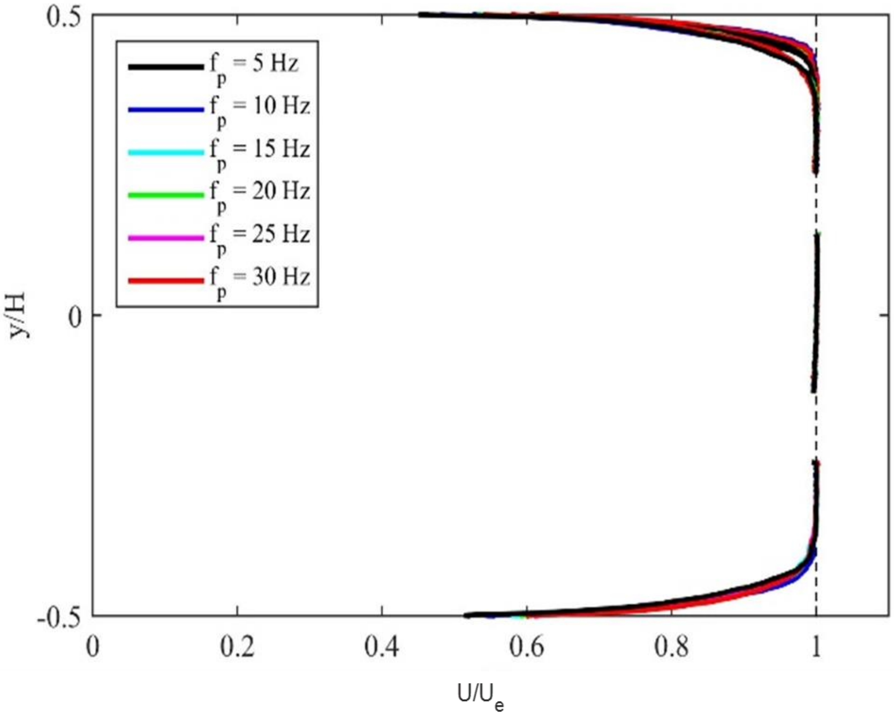

Figure 3-7. The mean streamwise velocity (*U*) profile scaled with the external velocity (U_e) and the test section height (*H*).

3.3 Instrumentation

3.3.1 Particle image velocimetry (PIV)

3.3.1.1 Overview of primary components

The primary instrument used in Chapters 5 and 6 was PIV, which was used to acquire the near-wall velocity vector field within TBLs. In the current work, two PIV setups were used to acquire time-averaged and time-resolved vector fields. Each of these systems and their configurations are described in detail in the following subsections, and Table 3-6 itemizes the key components (lasers and cameras) used in this study.

Table 3-6. Summary of the cameras and lasers used to perform time-averaged or time-resolved PIV in the current study.

Item	**Make**	**Model**	**Type**	**Sample Rate**	**Specifications**
High-speed diode pumped laser	Photonics	DM30-527	Nd:YLF	10 kHz (max)	30 mJ/pulse, 1 kHz full power
High-power laser	New Wave	Gemini 200	Nd:YAG	15 Hz (max)	200 mJ/pulse
High-Resolution Cameras (2x)	Imager sCMOS	LaVision	sCMOS	50 Hz (full res)	2560×2160 pixels, 275 Hz at 1 MP
High-speed Cameras (2x)	Phantom	M110	CMOS	1.6 kHz (full res)	1280×800 pixels, 5,790 Hz at half res

3.3.1.2 Time-averaged PIV

The empty test section mean velocity profile in tunnel characterization section in the current chapter and validation of canonical TBL in Chapter 5 were acquired with time-averaged two-dimensional (2D) PIV. An image plane was illuminated with a 532 nm Nd:YAG laser (Gemini-200, New Wave, Fremont, CA) beamformed into a sheet. Light scattered from 18 μm hollow glass-sphere tracer particles (iM30K, 3M, Maplewood, MN) was recorded with a 2560 pixels × 2160 pixels sCMOS camera (Imager, LaVision, Göttingen, Germany). A spatial calibration was performed with a high precision calibration target (Type 58- 5, LaVision, Göttingen, Germany). The typical field-of-view (see Figure 3-8) was nominally 49×41mm and images were recorded in double-frame, double-pulse mode. The mean velocity profiles from the tunnel performance characterization previously discussed were acquired at three streamwise locations and the top and bottom walls of the test section were considered. The nominal locations on the top wall are shown in Figure 3-8. The velocity vector-fields were computed using standard cross-correlation methods (DaVis8, LaVision) with a final interrogation window of 16×16 pixels with 50% overlap. At least 100 independent vector-field realizations were used for those mean velocity profiles. The displacement uncertainty was ~ 0.1 pixels, which corresponds to ~1% uncertainty in velocity.

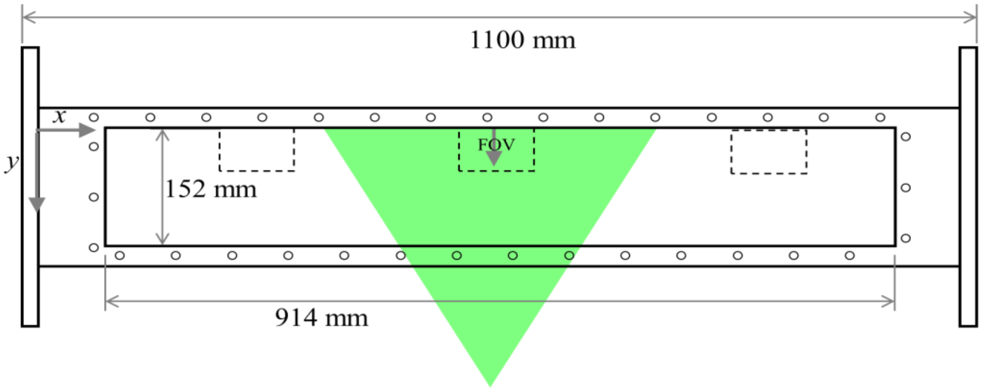

Figure 3-8. Test section schematic of the PIV measurement orientation with nominal locations of the PIV field-of-views (FOV) on the top wall for the tunnel performance characterization.

3.3.1.3 Time-resolved PIV

Time-resolved velocity vector fields were acquired at x = 0.5 m with 2D PIV and are discussed in Chapter 5 (mean and fluctuating velocity profiles) and Chapter 6 (coherent structure analysis). The image plane was aligned parallel to the flow, along the tunnel centerline (z = 0), and illuminated with a sheet of laser light. The laser sheet was formed from the beam of a high-speed Nd:YLF laser (DM30-527, Photonics) that was spread into a sheet with a cylindrical lens as illustrated in Figure 3-9. Hollow glass spheres with an average diameter of 18 μm (iM30K, 3M) and 10 μm (LaVision) were used to scatter the laser light. The scattered light was recorded at different rates based on the free stream velocities from 2.0 to 4 kHz with a high-speed camera (M110, Phantom) that had a maximum resolution of 1280 pixels × 800 pixels. The camera was fitted with a 60 mm diameter, f/2.8D lens (AF Micro NIKKOR, Nikon) that resulted in a nominal field-of-view (FOV) of 10 mm (streamwise) × 15 mm (wall-normal) and spatial calibration of maximum 85 pixels/mm. The images were calibrated with a custom-made calibration target

20 mm × 20 mm. The onboard camera memory allowed for the maximum of 6000 images to be acquired for a single sequence. The PIV timing, acquisition, and image processing were performed using a commercial software package (Davis 8.2.3, LaVision). The images were processed using the standard multi-pass cross-correlation method with decreasing interrogation window sizes. The final window size was 16 × 16 pixels or 32 pixels × 32 pixels with 75% overlap. Based on the particle density and resolution. The PIV uncertainty was quantified following the approach identified in Wieneke (2015), which uses the asymmetry in the correlation peaks when slightly shifted (~1 pixel) away from the optimized displacement to quantify the impact of image noise, including out-of-plane motion. For the current study, the maximum uncertainty was ±0.1 m/s (~ 0.3 pixels).

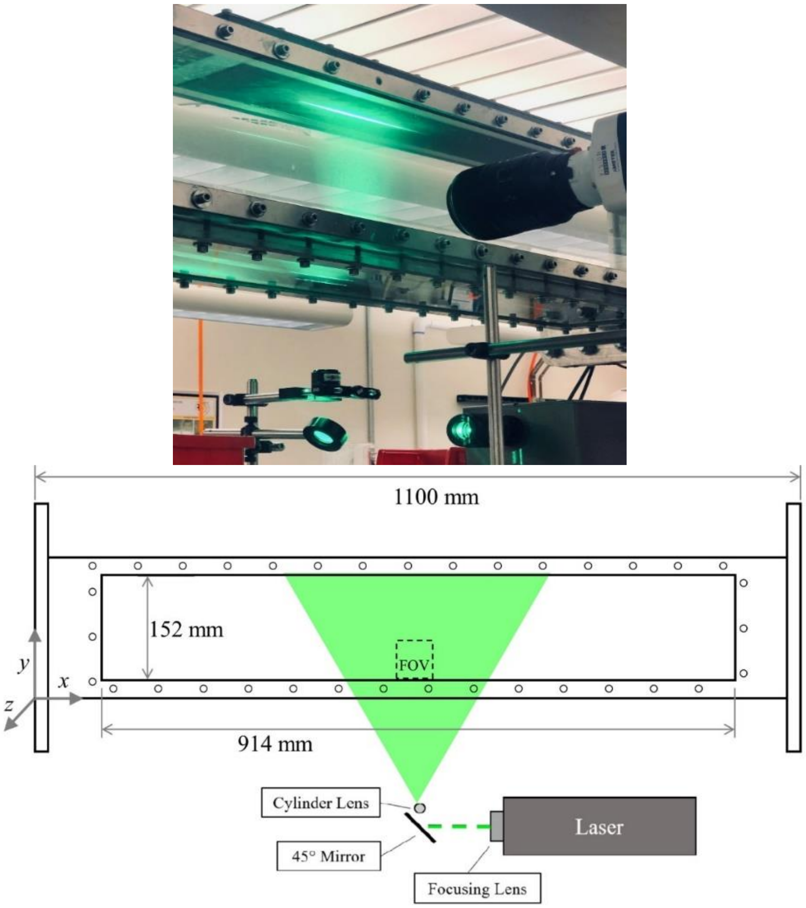

Figure 3-9. (top) Picture of the high-speed PIV system operating in the EFPL large water tunnel. (bottom) Schematic showing the configuration of the high-speed PIV system including the FOV location.

3.3.2 Tunnel monitoring

The water tunnel operation conditions (water temperature, static pressure, and pump motor frequency) were monitored throughout testing. The water temperature was measured with a T-Type thermocouple (TC-T-1/4NPT-U-72, Omega) located 0.92 m upstream of the contraction inlet. The static pressure was measured 76 mm upstream of the contraction inlet at the test section centerline elevation with a differential pressure transducer (PX230050DI, Omega). These measurements were recorded at 500 Hz throughout testing along with pump motor frequency from the variable-frequency-drive via a data acquisition card (USB-6218-BNC, NI) controlled with commercial software (LabView15.0.1, NI). The data acquisition system was also used to record the subset of tests with the hot-film-anemometer (MiniCTA-54T42, Dantec) using a hot-film probe (55R15, Dantec) located at x = 60 mm. This was performed to confirm that the inlet turbulence intensity was below 1% as previously discussed.

3.3.3 Pressure drop apparatus

The test facility was a pressure drop apparatus that was used to characterize polymer properties and acquire gross flow behavior. A schematic of the setup is shown in Figure 3.10 including the pipe as well as the instrumentation. Test samples were placed in an 18.9-liter 316L stainless steel pressure vessel (740560, Advantc), which was sealed and pressurized to ~275 kPa during testing. A dip tube drew the polymer sample from the bottom of the pressure vessel and then pushed it into the pipe flow portion. It consisted of a 10.9 mm inner diameter (d) instrument grade seamless 316 stainless steel pipe (SS-T8-S-035-20, Swagelok) that was divided into 3 sections; the entrance length that was 150d long to achieve fully developed turbulent pipe flow, a 1.05 m long test section, and the end (exit) length that had a V-shaped needle valve at the outlet to control flow rate (this valve was also used to degrade the polymers). The pressure drop across the test section was acquired at various Reynolds numbers with a differential pressure transducer (PX2300-5DI, Omega Engineering). The mass flow rate, and ultimately the average velocity within the pipe, was determined by measuring the mass of a sample on a 35 kg digital balance (CPWplus-35, Adam Equipment) while simultaneously recording the fill time with a stopwatch (RS-013, ProCoach). A more detailed discussion of the setup, instrumentation, and uncertainty quantification is provided in Lander (2018).

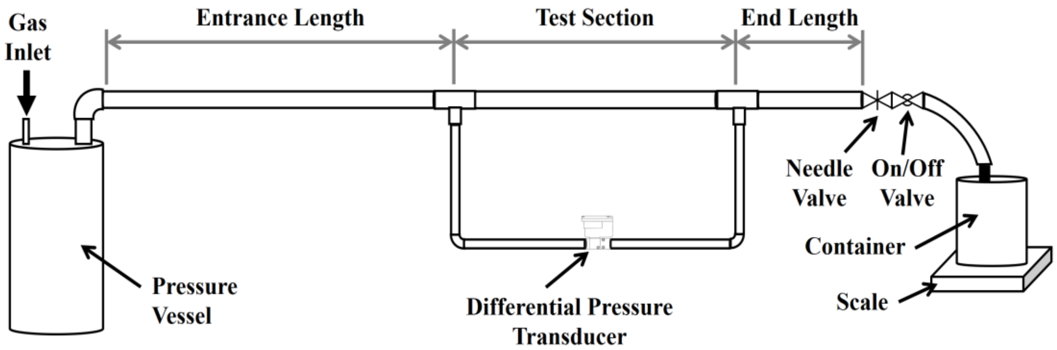

Figure 3-10. Schematic of the pressure drop apparatus used for characterization of the polymer samples as well as mechanically degrading samples.

3.4 Polymer preparation and characterization

3.4.1 Polymer preparation

PEO was the only polymer used in this study, which has a structural unit (monomer) of ($-O-CH_2-CH_2-$) that results in a polymer backbone consisting of carbon-carbon ($C-C$) and carbon-oxygen ($C-O$) bonds. Five molecular weights of PEO were tested with manufacturer specified mean molecular weights of 0.6, 1.0, 2.0, 5.0, and 8×10^6 g/mol (Sigma Aldrich) as well as 4.0×10^6 g/mol (WSR301, Dow chemical). Polymer solutions were prepared by sprinkling the dry powder into a water jet prior to contacting the free surface, formed by the solution in the preparation container, to avoid the formation of polymer aggregates. The hydration times for all the solutions prepared in this study, varied from 8-24 hours. Since the higher molecular weight samples require more time to hydrate than the lower ones, this justifies the selection of the given range of hydration periods. To confirm the sufficient hydration time and homogeneous solution, the drag reduction performance of the hydrated solution was compared with known values. Chlorine in the solvent (water) can cause polymer degradation (Draad et al., 1998; Petrie et al., 2003). Therefore, when solutions required hydration longer than 12 hours the background chlorine was removed by adding a trace amount of sodium thiosulfate, which residual sodium thiosulfate and the resultant products of the reaction with chlorine have been shown to not impact the PDR performance (De Gennes & Gennes, 1979). The total contact time of the solution with sodium thiosulfate varied between 12-24 hours, depending on the M_w being prepared. Stock solutions were prepared at relatively high concentrations (1000-5000 ppm), which once fully hydrated, additional water would be added to dilute the sample to the desired test concentration.

Polymer solution concentrations are broadly categorized as dilute, semi-dilute, and concentrated. In the dilute regime, each polymer chain is sufficiently distant from other polymer chains such that there is minimal interaction between chains. As the concentration increases, polymer chains eventually begin to overlap and become entangled, in which these interactions alter the polymer properties. As the concentration further increases from semi-dilute to the concentrated regime, molecules cannot move freely and significant interpenetration occurs due to the lack of space. These changes are identified from their rheological properties (Bailey & Callard, 1959). The critical overlap concentration C* defines the transition points from dilute to semi-dilute. The overlap concentration can be found from the inverse of the intrinsic viscosity ($[\eta]_0$), $C^* = [\eta]_0^{-1}$, which $[\eta]_0$ can be estimated from the Mark-Houwink relationship, $[\eta]_0 = 0.01248 {M_w}^{0.78}$. Table 3-7 provides the range of molecular weights and concentrations tested for degraded and non-degraded samples in this study as well as the corresponding intrinsic viscosity and C^*. The first overlap concentration was well above the test range at each molecular weight and, consequently, all testing was with dilute solutions.

Table 3-7. Summary of the range of molecular weights and concentrations tested in the current study as well as the corresponding intrinsic viscosity and overlap concentration for the given molecular weight PEO.

$M_w \times 10^{-6}$ (g/mol)	C range (ppm)	$[\eta]_0$ (cm^3/g)	C^* (ppm)
0.6	100 − 500	402	2500
1	500	598	1680
2	50 – 500	1030	975
4	5 – 100	1760	568
5	5 – 20	2100	477
8	50-100	3029	330

3.4.2 Polymer characterization

3.4.2.1 Relevant polymer parameters

To characterize the polymer solution, polymer properties and the parameters modifying the drag reduction of polymer solutions should be studied. There are three main non-dimensional polymer dependent parameters: 1) Weissenberg number $Wi = \frac{\lambda(u_\tau^2)}{v}$, the ratio of the longest polymer relaxation time to a flow characteristic time; 2) viscosity ratio $\mu^* = \mu_s/\mu_0$, the ratio of solvent viscosity to zero shear viscosity of polymer solution; 3) length ratio L of the fully extended to coiled polymer molecules. From the mentioned parameters, flow field parameter (u_τ) can be calculated from velocity profile measurements and the intrinsic drag reduction concept of polymer additives and ν is just dependent on water temperature. Other parameters (relaxation time, viscosity ratio, and length ratio) are less readily available. Relaxation time can be estimated by utilizing an analytical relationship from the literature. Viscosity ratio can be obtained from rheometer data, and the length ratio is a known function of molecular weight. A detailed discussion of all these have been given below.

3.4.2.2 Molecular weight

An experimental method was used to estimate the molecular weight of the polymer solution. In this method, the molecular weight can be determined by passing a diluted sample of polymer solution through the pressure drop apparatus and measuring pressure drop per unit length once fully developed. Friction factor from the pressure drop measurements over a range of Reynolds number are presented in the traditional P-K coordinates, $Re\sqrt{f}\,\frac{\text{and } 1}{\sqrt{f}}$. Newtonian and polymeric data in the range of Reynolds number is plotted in Figure 3-11. From the Non-Newtonian (polymer solution) and Newtonian data, the onset drag reduction shear rate can be identified. Vanapalli et al. (2005) produced a relationship from data compiled from P-K plot. This equation relates the minimum shear rate of drag reduction γ^* to the polymer molecular weight. This relationship is given in Equation 3.2 and 3.3. High molecular weight polymer solution, PEO is used in this experiment. Diluted solution with a concentration of 10 ppm was passed through a smooth round pipe with a diameter of 1.1 cm and a length of 1.05 m. In P-K coordinates the friction law for the fully turbulent flow of a Newtonian fluid in a smooth, round pipe is given by Equation 3.5. Figure 3-11 shows the sample P-K for the molecular weight of $1\times\frac{10^6 g}{mole}$. In Equation 3.2 and 3.3, ν is the kinematic viscosity of the solution (water viscosity for diluted polymer solution), γ^* is the minimum shear rate for drag reduction, d is pipe diameter, and U_{ave} is the average velocity in the pipe. Equation 3.4 shows fanning friction at the onset of drag reduction (f^*), where $\frac{\Delta p}{\Delta x}$ is the pressure drop per unit length of the pipe.

$$\gamma^* = \frac{1}{2}\frac{{U_{ave}}^2}{\nu} f^*. \tag{3.2}$$

$$\gamma^* = (3.35\times10^9){M_w}^{-1}. \tag{3.3}$$

$$f^* = \tau_w / 0.5\rho {U_{ave}}^2 = \frac{\frac{\Delta p}{\Delta x}(d)}{2\rho U^2}. \qquad (3.4)$$

$$\frac{1}{\sqrt{f}} = 4.0\, log_{10}\left(Re\sqrt{f}\right) - 0.4. \qquad (3.5)$$

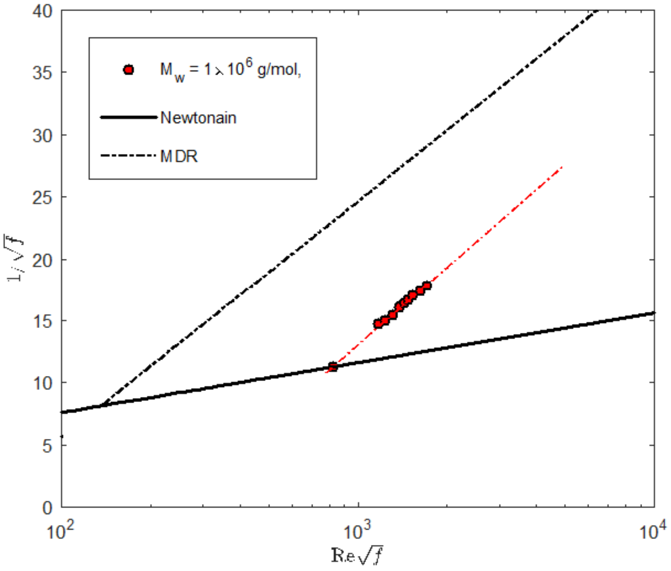

Figure 3-11 P-K plot of polymer solution onset of drag reduction from Newtonian line

Polymer data above the Newtonian line is curved fitted and extrapolated backward until it intersects the classical Newtonian turbulent pipe friction curve (solid orange curve). The onset of drag reduction is identified from the intersection of two curves. From the value of Reynolds number and shear rate at onset of drag reduction (intersection of two curves), which can be related to average molecular weight showed in Equations 3.2 and 3.3. The estimated M_w of the sample was 1.1×10^6 g/mole. This matches quite well with the manufacturer specified value of 1×10^6 g/mole.

3.4.2.3 Relaxation time

The relaxation time λ of the polymer solution, the time it takes for the chains to strech and recoil is related to the elastic energy that is stored in the fluid. This characteristic time is associated to the flow shear rate and other polymer properties and is not easy to be measured. For high molecular weight polyethylene oxide (PEO), two methods were used to estimate the relaxation time of the polymer. Zimm time (Zimm, 1956) and Kalashnikov time (Kalashnikov & Askarov, 1989). Zimm time is calculated from Equations 3.6 and 3.7:

$$\lambda_z = 0.422 \frac{[\eta]_0 \mu_s}{RT} M_w \text{ (s)} \tag{3.6}$$

$$[\eta]_0 = 0.0125 {M_w}^{0.78} \tag{3.7}$$

Here R is the ideal gas constant, T is temperature [℃] or [K], $[\eta]_0$ is intrinsic viscosity (calculated with Equation 3.7). When the polymer solution is diluted and the concentration is below the overlap concentration (C^*), the relaxation time can be estimated with Equation 3.9 (Kalashnikov, 1994). In the other word, when $C^* <<1$, relaxation time is concentration dependent. In Equation 3.9, T_c is the temperature in centigrade and C is polymer concentration (ppm).

$$C^* = {}^{1}\!/_{[\eta]_0} \tag{3.8}$$

$$\lambda_k = \left[\frac{[\eta]_0}{549.5} - \left(\frac{[\eta]_0}{3255}\right)^3 - 0.51\right] exp\left(-\left(\frac{T_c}{50}\right)^2\right) C^{0.5} \text{ (s)} \tag{3.9}$$

3.4.2.4 Viscosity ratio and length ratio

The other polymer solution property is the viscosity that can be obtained from rheometer data. However, here the viscosity ratio of the polymer solution is estimated by Equation 3.10 and 3.11 from the work of Kalashnikov (1994). In these equations, η_0 and η_∞ are viscosity at zero shear rate and infinity shear rate, respectively, and can be obtained from rheology data. When the polymer solution is dilute and high molecular weight, Kalashnikov (1994) presented an empirical relationship for viscosity ratio that is dependent on intrinsic viscosity and concentration of polymer solution.

$$\mu^* = \frac{1}{\Delta+1}. \tag{3.10}$$

$$\varDelta = \frac{\eta_0 - \eta_\infty}{\eta_\infty} = \left[\frac{\eta_0}{135.6} + 0.434\eta_0 - 126\right] C. \tag{3.11}$$

The length of the extended polymer to the coiled polymer is the length ratio that directly depends on the molecular weight of the polymer. The length of the coiled polymer is approximated from Equation 3.12 (Larson, 1999). M_0 is the monomer molar mass that is equal to 44.1 g/mole for PEO, $l_0$is the mean backbone bond length, and M_w is the molecular weight of the polymer. The polymer coiled length is approximated as a Gaussian function that depends on the chain length and the total number of monomers. The analysis leads to Equation 3.12 and consequently, the length ratio can be computed from Equation 3.13 (Larson, 1999).

$$L_{coil} = (0.82 l_0 \eta_0)\left(\frac{M_w}{M_0}\right)^{0.5}. \tag{3.12}$$

$$length\ ratio = \left(\frac{M_w}{M_0}\right)^{0.5}. \tag{3.13}$$

3.4.2.5 Measurement error uncertainty analysis

Propagating all sources of uncertainty results in uncertainties that significantly vary with flow condition resulting in P-K coordinates $Re\sqrt{f}$ and $1/\sqrt{f}$ having typical uncertainties of ~6%. However, at low flow rates (i.e. at and below the onset of drag reduction) the uncertainty increases rapidly to well above 10%. For these reasons measurements at the onset of drag reduction were not attempted, but rather measurements at higher flow rates with an uncertainty below 10% were curve fitted and then extrapolated back to the onset condition. Subsequently, the analysis focuses on the variations of the curve fit slopes, so a more detailed uncertainty analysis on the impact of these uncertainties in the P-K coordinates on the slope and intercept of the curve fits was performed. Here error was introduced to each of the P-K coordinates such that a logarithmic curve fit takes the form of $1/\left(\sqrt{f + \epsilon_o}\right) = C_o\ \ln\left(Re\sqrt{f} + \epsilon_1\right) + C_1$, where C_o, C_1 are constants and ϵ_o, ϵ_1 are the uncertainties in f and $Re\sqrt{f}$, respectively. Some algebraic manipulation and expanding the resulting expression in a binomial form results in

$$\frac{1}{\sqrt{f}}\left(1-\frac{\epsilon_o}{2f}+\cdots\right)=C_o\,ln\left(Re\sqrt{f}\right)+C_o\,ln\left(1+\frac{\epsilon_1}{Re\sqrt{f}}\right)+C_1. \tag{3.14}$$

Neglecting higher-order terms and some addition rearranging reduces the relationship to

$$\frac{1}{\sqrt{f}}=C_o\,ln\left(Re\sqrt{f}\right)+C_o\,ln\left(1+\frac{\epsilon_1}{Re\sqrt{f}}\right)+C_1+\frac{\epsilon_o}{2f^{1.5}}. \tag{3.15}$$

Treating the error sources as being nominally constants, this shows that the uncertainty impacts the intercept more than the slope when $Re\sqrt{f}$ is large (current data $Re\sqrt{f}\sim10^3$). Detailed analysis can be found in Saeed (2019).

3.4.3 Estimation of drag reduction for polymeric flows

In addition, the pressure drop apparatus was used to determine the intrinsic concentration $[C]$ and intrinsic drag reduction $[DR]$ (Virk et al., 1967). The intrinsic polymer properties are used to establish a relationship between the polymer concentration (C) and the resulting drag reduction (DR), $DR/C=[C][DR]/([C]+C_M)$ (Virk, 1971; Choi & Jhon, 1996). Choi and Jhon (1996) showed that these intrinsic drag reduction properties for solutions of PEO-water were universal regardless of the flow geometry and solvent. Thus, the intrinsic properties could be used to determine the drag reduction relative to the Newtonian result within the polymer ocean.

3.5 Data analysis

3.5.1 Two-point correlation

The spatial coherence and the statistical significance of various features within the velocity field were quantified using two-point spatial correlations (R_{uu}) of the streamwise velocity fluctuations. The functional form of (R_{uu}) is

$$R_{uu}\left(x_{ref},y_{ref},\Delta x,\Delta y\right)=\frac{\langle u\left(x_{ref},y_{ref}\right)u\left(x_{ref}+\Delta x,y_{ref}+\Delta y\right)\rangle}{\sigma_u\left(x_{ref},y_{ref}\right)\sigma_u\left(x_{ref}+\Delta x,y_{ref}+\Delta y\right)}. \tag{3.16}$$

Here, x_{ref} and y_{ref} are the spatial locations of the reference point, σ_u is the standard deviation of u at the specified location, $\langle \quad \rangle$-brackets indicate an ensemble average, and Δx, Δy are the streamwise and vertical separation distances from the reference location, respectively. For a true ensemble average R_{uu} is a function of x_{ref} and y_{ref}. For practical reasons, a surrogate ensemble average, $\langle x \rangle = \frac{1}{N}\sum_{i=1}^{N} x_i$ with N = 5000 PIV vector fields is adopted. Here (N) was selected based on the convergence of the correlation curves, the number of points in the ensemble average decreases linearly with increasing separation distance due to the finite-sized FOV, which Taylor's frozen turbulence hypothesis was invoked to mitigate this issue. Inclined motions frequently result in elliptically shaped two-point correlation maps with the principal axis inclined at an angle away from the wall, termed the structure inclination angle. Their identification follows the general analysis of Marusic (2001). Following this, the dominant structure inclination angle (α) can be found from the slope, $\alpha = tan^{-1}(\langle \Delta y/\Delta x_{pk} \rangle)$, where ($\Delta x_{pk}$) is the streamwise separation distance of the peak in the two-point correlation.

3.5.2 Proper orthogonal decomposition (POD)

The principle and equations of POD can be found in many places in the literature and they are only summarized below. In this study, snapshot POD was used on the PIV measured velocity fields in boundary layers in the streamwise, wall-normal plane. In POD, any instantaneous fluctuating velocity field $u(x,t)$ can be decomposed into the form of:

$$u(x,t) = \sum_{n=1}^{\infty} a_n(t)\, \Phi_n(x). \tag{3.17}$$

where $\Phi_n(x)$is deterministic spatial POD modes, and $a_n(t)$ is random temporal coefficients. In snapshot POD, the coefficients $a_n(t)$ are obtained first by solving the eigenvalue problem with a positive definite Hermitian kernel of the form,

$$\lambda_n a_n(t) = \int \left(\int_{\Omega} u(x,t)u(x,t')dx \right) a_n(t')dt'. \tag{3.18}$$

where the integrations are over the spatial domain and a time interval T. For an ensemble of PIV measured velocity fields, the spatial domain could be the whole or part of the PIV field of view and the time domain represents the ensemble or the collection of samples of the velocity fields. The eigenvalues λ_n are real and positive and form a decreasing and convergent series. The POD modes can then be computed through the equation

$$\Phi_n(x) = \frac{\int_T u a_n dt}{\int_T a_n^2 dt}. \tag{3.19}$$

The turbulent kinetic energy (K) is equal to half of the summation of the eigenvalues, i.e.,

$$K = \frac{1}{2\langle u.u \rangle} = \frac{1}{2\sum \lambda_n.} \tag{3.20}$$

Since the POD modes are usually normalized to be orthonormal the POD coefficients (a_n) are related to the eigenvalues by

$$\int_T [a_n(t)]^2 dt = \lambda_n. \tag{3.21}$$

which dictates that the instantaneous fluctuating velocity field with a larger value of a_n^2 contributes more to the eigenvalue λ_n. Therefore, Equation 3.19 provides a possible means to identify what are the instantaneous fluctuating flow structures that contribute significantly to the initial dominant POD modes. It is this equation that the current study is based on to establish the connection between the large-scale instantaneous turbulence structures, most importantly the hairpin vortex packets. The turbulence structures contributing significantly to higher (> mode 10th) POD modes were not sought in this work since they accounts for a much smaller amount of kinetic energy. Since the contribution to the eigenvalue $\lambda_n$comes from a_n^2, instantaneous velocity fields with either positive a_n or negative a_n contain equivalently important information on the flow structures relevant to the nth POD mode.

CHAPTER IV

4 DRAG REDUCTION PERFORMANCE OF MECHANICALLY DEGRADED POLYMER SOLUTION

4.1 Introduction

Polymer degradation has had a significant impact on PDR external applications and even the ability to study PDR within a TBL. Therefore, characterizing the degradation of long-chain polymers and their drag reduction performance is an important area of investigation. Polymer chains scission is indicative of the fact that the polymer molecules actively interfere with the flow dynamics and therefore are engaged in transporting energy of the flow to effect drag reduction. In studying polymer modification to TBLs, researchers have observed deviations from the classical view of how polymer modify velocity profiles (White et al., 2012; Elbing et al., 2013. One of the missing pieces in identifying the source(s) of these deviations is the fact that many studies have not considered the degradation of polymers. Also in the experimental research that directly measures the skin friction drag reduction, the effect of degradation on the performance of PDR using PEO has not been quantitatively and comprehensively provided. In previous studies using other polymer solutions, methods to directly measure the molecular weight distribution of polymers were used and the likely impact of degradation on the molecular weight distribution is inferred (Berman, 1977; Hunston & Zakin, 1980; Gampert & Wagner, 1985).

In the work of Hunston and Zakin (1980), GPC method directly measurements the molecular weight distribution. However, this method has proven to be impractical for high molecular weight PEO due to significant uncertainties in the analysis.

Methods that directly measure the molecular weight distribution and the limitation using them for high molecular weight polymers, such as PEO, were reviewed in Chapter 2. This chapter quantifies the impact of mechanical degradation via chain scission on the drag reduction performance of PEO primarily from the resulting variations in the turbulent drag reduction performance. In the following subsections, the test conditions and degradation method is provided, evaluation of the bulk flow behavior of a degraded and non-degraded sample of polymer is presented and compared with trends observed in the literature. A subset of conditions showed significant deviation in the slope increment (drag reduction performance) between the degraded and non-degraded samples with degraded samples consistently more efficient than the non-degraded samples, even though they had the same mean molecular weight. These deviations were analyzed and scaled with polymer properties. Following the subsections, data analysis of deviations in the polymer performance (slope increment) and their dependency on molecular weight distribution is provided. In the last subsection of this chapter, a summary of these results and conclusions are presented.

4.2 Results

4.2.1 Non-degraded bulk flow characterization

In characterizing the polymer solution in Chapter 3, the molecular weight of the polymer was estimated using pipe flow analysis. Using the pressure drop apparatus described in the previous chapter, the same approach was used to evaluate the drag reduction performance of different polymer solution samples. Again, P-K coordinates ($Re_d\sqrt{f}$ and $1/\sqrt{f}$) were used for analysis, where Re_d $\left(=\frac{\rho V d}{\mu}\right)$ is pipe diameter-based Reynolds number, f is the Fanning friction factor $\left(f=\frac{2\tau}{\rho V^2}\right)$, ρ is the fluid density, V is the mean velocity, d is the pipe diameter, μ is the fluid dynamic viscosity, and τ is the wall shear stress. Assuming fully developed pipe flow, the wall shear stress (τ) is directly related to the pressure drop across a given length of pipe ($\tau = \Delta p\ d/4\ \Delta x$), where Δp is the pressure drop measured over the pipe length Δx. The physical significance of P-K plots is that the ordinate is the ratio of the bulk fluid velocity to the turbulent friction velocity (divided by $\sqrt{2}$) and the abscissa is the ratio of the pipe diameter (outer length scale) to the viscous wall unit (inner length scale) (multiplied by $\sqrt{2}$). The skin-friction curve for Newtonian turbulent pipe flow in these coordinates was well represented by the P-K law, Equation 4.1. Newtonian (water) results from this study are included as well. These results are well approximated by the P-K law, which is also included for comparison.

$$\frac{1}{\sqrt{f}} = 4.0\ log_{10}\left(Re_d\sqrt{f}\right) - 0.4. \tag{4.1}$$

With the addition of a drag-reducing polymer (PEO) solution, the results are shifted above the P-K law. The amount of increase is limited by the empirically derived maximum drag reduction (MDR) asymptote (Virk et al., 1967) given in Equation 4.2. The current study focuses on results within the polymeric region, which is at intermediate drag reduction levels between the MDR asymptote and the P-K law. The data within the polymeric regime are fitted following the form given in Equation 4.3 (Virk, 1975). Here, δ is the slope increment, and W^* is the onset wave number, which both are dependent on the polymer properties. Furthermore, the slope increment (δ) is the change in slope relative to the P-K law slope, and the onset wave number (W^*) can be shown to be equal to the reciprocal of the viscous wall unit at the onset of drag reduction. The onset of drag reduction is identified by the intersection of the P-K law and the polymeric data fitted with Equation 4.3. Note that below this minimum shear rate required to initiate drag reduction, the polymer solutions follow the P-K law, which is indicative of the need for a sufficient amount of shear to stretch the polymer chains and activate the drag reduction mechanism (Dubief et al., 2004; Gupta et al., 2004). The onset of drag reduction for a given polymer type and molecular weight has been shown to have a negligible dependence on the concentration (Virk, 1975; Vanapalli et al., 2005). Current polymeric results using PEO at a $M_w = 2 \times 10^6$ g/mol and at concentrations from 100 to 500 ppm are also provided in Figure 4-1. These results show that the slope increment increases with increasing polymer concentration (C) while the onset of drag reduction (intersection of P-K law and polymeric data fit) remains nearly constant for all three samples tested.

$$\frac{1}{\sqrt{f}} = 19.0\, log_{10}\left(Re_d\sqrt{f}\right) - 32.4. \tag{4.2}$$

$$\frac{1}{\sqrt{f}} = (4.0 + \delta) log_{10}\left(Re_d\sqrt{f}\right) - 0.4 - \delta log_{10}\left(\sqrt{2} d W^*\right). \tag{4.3}$$

While the onset of drag reduction remains constant for a given molecular weight, it is sensitive to the mean molecular weight. Generally, the higher the M_w the lower the Reynolds number at the onset of drag reduction. Vanapalli et al. (2005) compiled PEO data (Virk, 1975) to establish an empirical relationship between the onset of drag reduction shear rate (γ^*) and the mean molecular weight (M_w), $\gamma^* = 3.35 \times 10^9 / M_w$. This allows for the mean molecular weight to be determined if the wall shear rate at the onset of drag reduction is known. The wall shear rate at the onset of drag reduction is determined by calculating the intersection between the polymeric best-fit curve and the P-K law. The intersection provides the corresponding onset of drag reduction Fanning friction factor (f^*) and the onset of drag reduction Reynolds number (Re_d^*). Given the definition of the Fanning friction factor and the relationship between shear stress and the shear rate at the wall ($\gamma = \tau / \rho \nu$), the onset shear rate at the onset of drag reduction can be determined from $f^*, \gamma^* = V^2 f^* / 2\nu$. Thus, the mean molecular weight of the PEO polymer solutions can be inferred from the P-K plots. Table 4-1 provides a summary of the non-degraded conditions tested, including mean molecular weight (M_w) (both the manufacturer specified and that determined from the onset of drag reduction; Vanapalli et al., 2005), the resulting slope increment (δ), onset wave number

(W^*), and the shear rate at the onset of drag reduction (γ^*). Note that most of the calculated mean molecular weights are slightly below the manufacturer specifications, which is consistent with past observations. These results demonstrate that the onset of drag reduction does vary with mean molecular weight since the molecular weights shown are consistent with the manufacturer specified values.

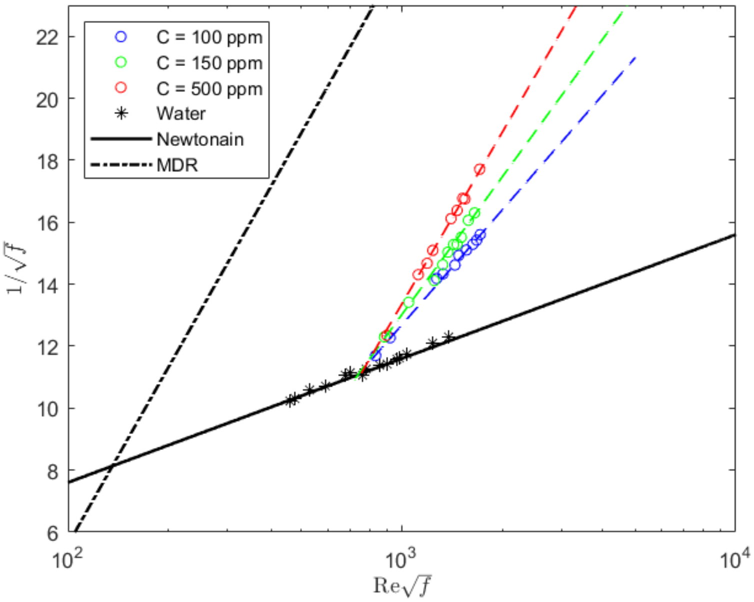

Figure 4-1 P-K plot of 2×10^6 g/mol PEO at concentrations of 100, 150, and 500 ppm, as well as water (Newtonian) data at the same range of $Re\sqrt{f}$. Included for reference are the P-K law, MDR asymptote, and logarithmic best-fit curves to the data within the polymeric regime.

Table 4-1. Summary of non-degraded samples tested in the pressure drop apparatus as well as the resulting slope increment (δ), onset wave number (W^*), and the shear rate at the onset of drag reduction (γ^*). The manufacturer specified molecular weight is provided as well as those determined from the onset of drag reduction (Vanapalli et al., 2005).

M_w ×10^{-6} (g/mol)		C range (ppm)	δ (--)	W^* at C_{max} (m^{-1})	γ^* (s^{-1})
manufacturer	calculated				
0.6	0.55	100 – 500	3.1 – 7.5	85,200	6,090
1	1.1	500	13.5	71,900	3,050
2	1.7	50 – 500	5.2 – 14.5	47,700	1,950
4	3.7	5	6.13	30,900	900
5	4.8	5	7.5	27,800	697

4.2.2 Degraded bulk flow characterization

It is well documented that when the wall shear rate is sufficiently large mechanical degradation via chain scission is possible (Yu et al., 1979; Hunston & Zakin, 1980; Elbing et al., 2011). While a universal scaling law for chain scission based on the molecular bond strength (Vanapalli et al., 2006) is provided, PEO has an established empirical relationship for the shear rate at the onset of degradation (γ_D) for a given mean molecular weight, $\gamma_D = 3.23 \times 10^{18} M_w^{-2.20}$ (Vanapalli et al., 2005). Based on this relationship, if the shear rate exceeds γ_D, the polymer chains will break and the mean molecular weight will decrease. Within the polymeric regime on a P-K plot, this is realized as data deviating from the logarithmic curve at higher $Re\sqrt{f}$ and bending back towards the P-K law (Moussa & Tiu., 1994; Elbing et al., 2009). This empirical relationship was used to design the current pressure drop apparatus (described in Chapter 4) and select the operation range such that no degradation occurred prior to the pressure drop measurement section. However, downstream of the measurement section was a needle valve that controlled the flowrate, which produced sufficiently high shear rates to rapidly degrade PEO via chain scission (i.e. breaking of the carbon-carbon and carbon-oxygen bonds that make up the polymer backbone). Thus, mechanically degraded samples were produced by passing a sample through the pressure drop apparatus with the needle valve in a predetermined position prior to passing them through a second time to characterize the degraded samples.

An example of a characterization of a degraded sample from the current study is provided in Figure 4-2. Here a sample with an initial molecular weight $M_{wi} = 2 \times 10^6$ g/mol was degraded to $M_{wf} = 0.6 \times 10^6$ g/mol. For comparison, results from a non-degraded $M_w = 2 \times 10^6$ g/mol sample are also provided along with the P-K law (Equation 4.1) and the MDR asymptote (Equation 4.2). The impact of mechanical degradation on the polymer behavior is apparent from the onset of drag reduction for the degraded sample shifted to the right (i.e. to high Reynolds numbers and shear rates) compared to the non-degraded sample. This is consistent with Vanapalli et al. (2005) that the lower the mean molecular weight the higher the shear rate at the onset of drag reduction. A summary of the degraded results that had a corresponding non-degraded sample are given in Table 4-2, which includes the nominal initial molecular weight (M_{wi}) and final molecular weight (M_{wf}) as well as the polymeric regime characterization parameters.

Table 4-2. Summary of degraded PEO samples tested in the pressure drop apparatus. Molecular weights listed are based on the nominal manufacturer specifications, see Table 4-1 for corresponding measurements.

$M_{wi} \times 10^{-6}$ (g/mol)	$M_{wf} \times 10^{-6}$ (g/mol)	C (wppm)	$Re \times 10^{-3}$ at $C_{\max}$ range (--)	δ (--)	γ^* (1/s)	$\Gamma \times 10^{-3}$ range (1/s)
5.0	1.0	500	15 – 25	22.5	2800	4.2 − 8.1
4.0	1.0	500	15 – 30	20.6	3000	4.5 − 12
4.0	2.0	50 – 500	12 – 28	4.5 – 11.0	1600	1.8 − 10
5.0	2.0	500	12 – 24	16.6	2000	3.3 − 7.6
5.0	4.0	5	8 – 24	6.1	900	1.2 − 8.8
2.0	0.6	200 – 500	18 – 31	3.5 – 10.1	6090	7.7 − 15
1.0	0.6	500	16 - 27	2.8	7200	1.7-4.9

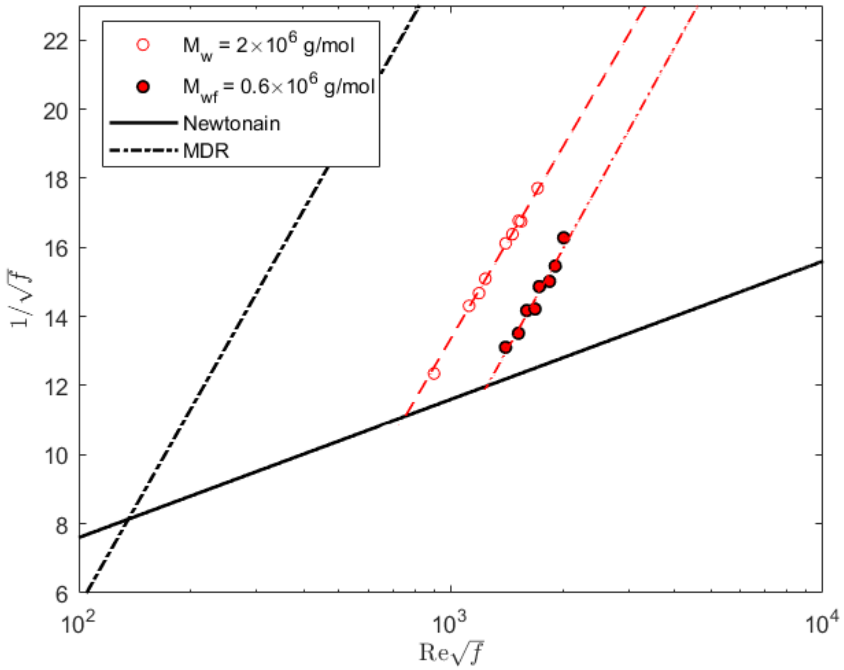

Figure 4-2. P-K plot using PEO at an initial M_{wi} = 2×10^6 g/mol and C = 500 ppm. One of the samples was degraded to a lower molecular weight (M_w = 0.6×10^6 g/mol) while the other was non-degraded.

4.3 Discussion and analysis

4.3.1 Drag reduction performance

PDR generally is defined based on the reduction of the wall shear stress relative to the Newtonian (e.g. water) flow. For pipe flows the drag reduction efficiency of a polymer solution can be quantified based on the change in the slope relative to the P-K law (i.e. the slope increment, δ). Thus, to quantify the impact of mechanical degradation on the drag reduction ability of the polymer, degraded and non-degraded samples with the same onset of drag reduction (i.e. nominal mean molecular weight) and concentration were characterized and their resulting slope increments compared. These pairs of degraded/non-degraded samples with matching mean molecular weights were identified as described in the previous section, and listed in Table 4-2. As an example, three of these degraded/non-degraded pairs are plotted using P-K coordinates in Figure 4-3. These pairs were selected to show that concentration only weakly impacted the deviations of the slope increments, there are some conditions where the matched pairs have negligible variation and other conditions that produced significant variation. Prior to exploring the cause for these observations, the specifics of these representative conditions are discussed.

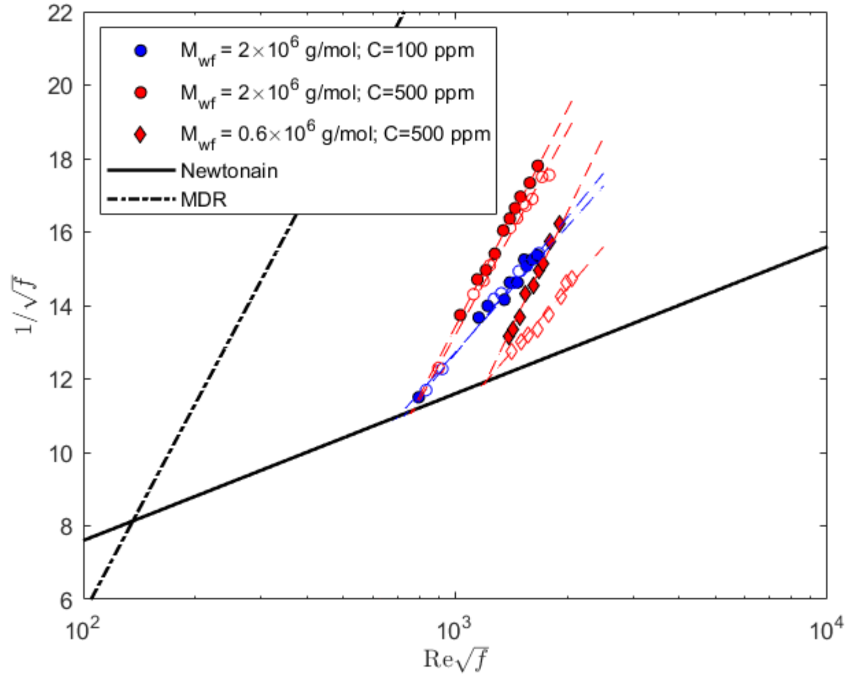

Figure 4-3. P-K plot comparing degraded and non-degraded samples with $M_{wf} = 2\times10^6$ g/mol (degraded samples had $M_{wi} = 4\times10^6$ g/mol) or 0.6×10^6 g/mol (degraded sample had $M_{wi} = 2\times10^6$ g/mol). Filled markers represent degraded samples.

First, the examination of the two pairs in Figure 4-3 that had $M_{wi} = 4\times10^6$ g/mol degraded to $M_{wf} = 2\times10^6$ g/mol with either $C = 100$ ppm or 500 ppm shows excellent agreement between the degraded and non-degraded samples for both pairs. The maximum relative difference between degraded and non-degraded samples was ~5%, which is within measurement uncertainty. However, the deviation appears to increase slightly with increasing concentration, which suggests that the slope increment deviation could have a potential weak concentration dependence. While these first two pairs indicated that mechanical degradation had a negligible impact on the drag reduction performance if the mean molecular weight was matched, the other degraded/non-degraded pair

(M_{wi} = 2×10^6 g/mol degraded to M_{wf} = 0.6×10^6 g/mol with C = 500 ppm) in Figure 4-3 reveals a significant difference in slope increment. Since the concentration was matched with one of the M_{wi} = 4×10^6 g/mol samples, the deviation must be dependent on the initial and/or final molecular weights of the polymer solution. Also note that all of the degraded samples have a larger slope increment (i.e. more efficient at reducing drag) relative to their non-degraded samples, even for the first two pairs that had minimal deviation.

Based on observations from previous work (Gampert & Wagner, 1985), the similarity between the first two degraded/non-degraded pairs indicates that within the range of Reynolds numbers tested (Re < 35,000) the longer chains were not preferentially extended over other comparable, but slightly shorter, chains. Thus the difference in chain size must not have been sufficient to drastically change the flow characteristics of the solution and, therefore, no significant difference in bulk behavior was observed. However, for the other degraded/non-degraded pair, the significantly improved drag reduction performance with degraded polymer suggests that there are longer chains in the degraded sample because the magnitude of drag reduction rather strongly depends on the longest polymer chains in the solution. Gampert and Wagner (1985) showed that a Reynolds number of 20,000 was enough to degrade the fractions of large chains. Since the Reynolds number range of the current study exceeds 20,000, these observations indicate preferential stretching and degradation that suggests that deviations are associated with changes in the molecular weight distribution. This is further examined subsequently.

The slope increment is sensitive to the polymer concentration, polymer-solvent combination, and molecular weight (Virk, 1975). This complicates comparison between individual degraded/non-degraded pairs because the molecular weight sets the range of polymer concentrations that can be tested in a given pressure drop apparatus (i.e. higher molecular weight samples require lower concentrations than lower molecular weight samples). That prevents the possibility of fixing all of the conditions at a single concentration and polymer-solvent combination to study the dependence of the slope deviation on molecular weight. However, Virk (1975) compared numerous combinations of polymer types and solvents and showed that the slope increment is well approximated as being proportional to the square root of concentration. The slope increments from the current results for degraded/non-degraded 0.6 and 2.0×10^6 g/mol samples are plotted versus concentrations (C) in Figure 4-4. The results are well approximated by best-fit curves having slopes of 0.5, which the power-law fit to the raw data produces exponents that were ±5% of 0.5 for all conditions. These results capture the sensitivity of the slope increment to molecular weight as well as the discrepancy observed in Figure 4-3 between the degraded and non-degraded $M_w = 0.6\times10^6$. It also shows that the slope increment for the degraded samples maintain the same $C^{1/2}$ dependence as non-degraded samples, which again indicates that the deviations with degradation must be related to molecular weight distribution.

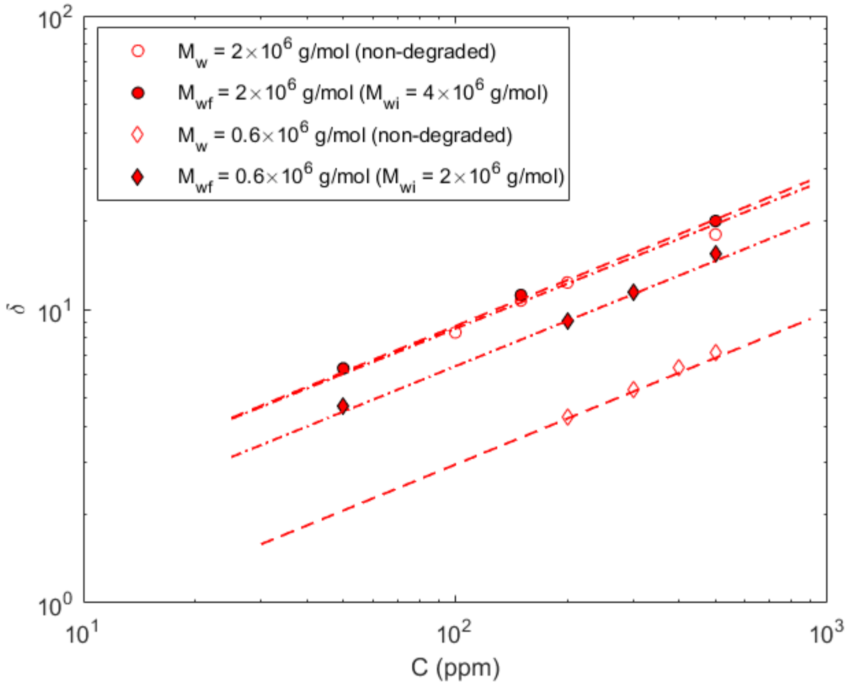

Figure 4-4. Slope increment versus concentration (C) for degraded and non-degraded samples of $M_w = 0.6\times10^6$ or 2.0×10^6 g/mol. The dashed lines are all best fit curves with a slope of ~0.5.

The discussion of Figure 4-3 noted that the deviation between the slope increment of degraded (δ_D) and non-degraded (δ_{ND}) samples must be dependent on the initial and/or final molecular weights of the samples. Since the slope increment deviation ($\delta_D - \delta_{ND}$) should approach zero as degradation approaches zero, a reasonable parameter to scale the deviation is the difference between the initial and final molecular weights. This difference was normalized with initial molecular weight to make the scaling parameter, $\zeta = (M_{wi} - M_{wf})/M_{wi}$. Figure 4-5 plots the slope increment deviation ($\delta_D - \delta_{ND}$) as a function of ζ for C = 500 ppm. The first observation from these results is that for all conditions the degraded slope increment was higher than the corresponding non-degraded slope increment (i.e. the slope increment deviation is never negative). In addition, these results show a relatively small deviation for $\zeta < 0.6$, followed by a rapid increase in the deviation. Note that the slope increments for these conditions ranged from 6 to 22.

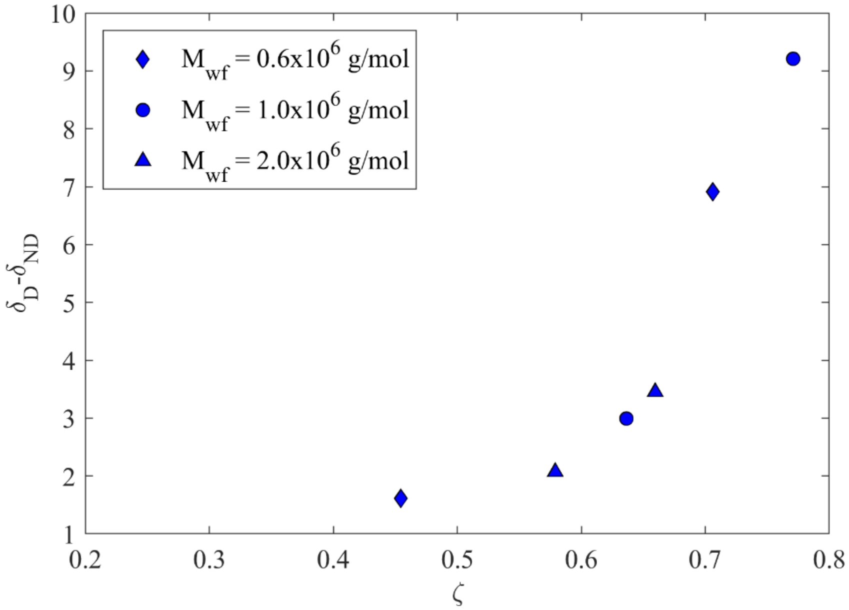

Figure 4-5. The difference between the degraded and non-degraded slope increments for C = 500 ppm plotted versus the normalized difference between the initial and final molecular weights, $\zeta = (M_{wi} - M_{wf})/M_{wi}$.

4.3.2 Polydispersity

Since testing was performed within the same flow operation range (Reynolds number, geometry, etc.), the deviation must be the product of variations within polymer properties. Most PEO polymer properties (e.g. relaxation time, viscosity ratio, length ratio) are primarily a function of the molecular weight and concentration. Since the concentration and mean molecular weight (i.e. onset of drag reduction shear rate) are equal between the degraded and non-degraded PEO samples, the deviation in performance within the polymeric regime must be related to variations in the distribution of the molecular weight. Many studies have discussed the importance of analyzing degraded polymer properties such as the impact of degradation on molecular weight distribution (Paterson & Abernathy, 1970; Hunston & Zakin, 1980). Turbulent measurements, like those in the current study, were used to broaden the range of conditions that could be studied with viscosity or GPC methods (Hunston & Zakin, 1980). Hunston and Zakin (1980) showed that for polystyrene the onset of drag reduction was dependent on the molecular weight with the results biased towards the largest molecules in the sample, and that flow rate dependence was related to the shape of the top part of the molecular weight distribution. This supports the hypothesis that the deviations in slope increment with the PEO samples were likely the product of a change in the molecular distribution (polydispersity) of the samples.

While this suggests that the deviations are related to changes in the molecular weight distribution, it does not explain the consistent improvement of the degraded samples relative to the non-degraded (at the same mean molecular weight) samples. The longer chain molecules have the greatest impact on determining the flow properties of a solution due to their preferential mode of extension (Gampert & Wagner, 1985), which suggests that the current samples (especially those with the largest ζ) had a larger percentage of the longer chain molecules than the non-degraded samples. In general, mechanical degradation narrows the molecular weight distribution if the shear rate is relatively uniformly applied (Yu et al., 1979). Wall-bounded flows (e.g. pipes, boundary layers) do not have uniformly applied shear rates, which results in a relatively small percentage of the chains being stretched to lengths comparable to the polymer contour length (i.e. maximum polymer extension length) at any instance in time (Gupta et al., 2004). However, if the polymer chains are exposed to the turbulent wall-bounded flow for a sufficiently long period of time, a steady-state condition can be achieved once a sufficient number of stretching/degradation cycles are achieved (Elbing et al., 2011). If the elongational rate far exceeds that of the critical elongational rate, then the midpoint scission assumption (Hinch, 1977; Odell et al., 1983) would be violated and the final (steady-state) distribution would be broader than the initial (Sim et al., 2007). Prior to achieving steady-state conditions, the molecular weight distribution would be asymmetric and biased towards higher molecular weights because at each time step some percentage of chains would not have broken yet. This suggests that the current results correspond to an intermediate stage of degradation (i.e. prior to achieving steady-state behavior), which was confirmed by comparing results after multiple passes through the pressure drop apparatus.

The deviation in slope increment for $\zeta > 0.6$ is also indicative of the fact that a mere presence of a few long chain polymer molecules within a solution can be responsible for significantly increasing the drag reduction. That is to say, these small fractions of long chain molecules have a greater impact in defining the flow properties of a degraded sample, than the mean molecular weight of the sample (Paterson & Abernathy, 1970). The validity of this claim, within the specified regime of ζ, is also subject to the Reynolds number range tested, which for the current study was predominately below 30,000. For this range of Reynolds numbers, it could be justified to say that the long chain polymers show preferential extension over the shorter chains and therefore control flow properties of the solutions. Such a behavior is expected to be more pronounced when the disparity between short chains and long chains within a solution is large (disparity in terms of their molecular weight averages). Although Gampert and Wagner (1985) used artificially created polydispersed synthesized PAM solutions, they reached the same conclusions, which provides additional support to the validity of these conclusions.

The functional relationship for the ζ dependence as shown in Figure 4-5, and more specifically the value where significant variation was observed, is most likely specific to the degradation process. If the residence time were increased, it is presumed that a larger value of ζ could be achieved without significant deviations in the slope increment since any variation would be the product of the broadening of the distribution (Sim et al., 2007) rather than an excess of larger molecules. As the ratio of the residence time to relaxation time becomes large, the steady-state molecular weight would be achieved and the impact of ζ is expected to significantly decrease if these assumptions are valid. This was tested by creating a PEO polymer ocean with C = 100 ppm within the Oklahoma State University 6-inch low-turbulence, recirculating water tunnel (Elbing et al., 2018). This allowed the facility to be operated for as long as it was required to achieve a steady-state mean molecular weight (based on the onset of drag reduction). In addition, the speeds were selected so that the steady-state molecular weights matched two of the non-degraded molecular weights (M_{wf} of 0.6×10^6 g/mol and 2×10^6 g/mol). The results for the steady-state degraded samples are shown in Figure 4-6 along with their corresponding non-degraded samples. The deviations in the slope increment for the 0.6×10^6 g/mol and 2×10^6 g/mol samples were $\delta_D - \delta_{ND} < 0.5$ ($\zeta =$ 0.8) and $\delta_D - \delta_{ND} = 1.3$ ($\zeta = 0.5$), respectively. These variations are within the measurement uncertainty and illustrate the difference from that observed in Figure 4-5, which supports the conjecture that these deviations can be mitigated if steady-state conditions can be achieved.

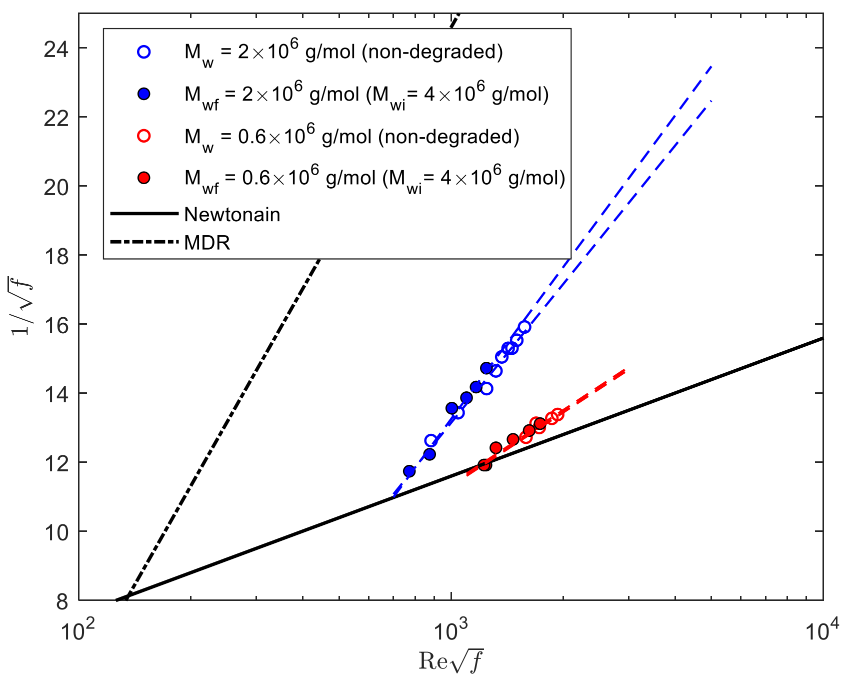

Figure 4-6. P-K plot comparing steady-state degraded samples with *C* = 100 ppm of PEO polymer ocean in a recirculating water tunnel with that of non-degraded samples.

4.4 Conclusion

The current chapter used a turbulent pipe flow experiment to do a comparative analysis between mechanically degraded polymer (PEO) solutions and non-degraded polymer (PEO) solutions at the same mean molecular weight. Degraded samples were produced via passing samples through a pipe that included a precisely positioned V-shaped needle valve. The degradation resulted in an increase in the shear rates at the onset of drag reduction, which Vanapalli et al. (2005, 2006) provided an empirical relationship between the onset of drag reduction shear rate and the mean molecular weight for PEO. The samples were degraded such that they produced mean molecular weights (onset of drag reduction shear rates) that matched available non-degraded molecular weights. Characterization of the non-degraded samples produced bulk flow behavior that is consistent with previous PEO studies in the literature (Virk, 1975; Gampert & Wagner, 1985; Vanapalli et al., 2005; Elbing et al., 2009).

Comparative analysis of the mechanically degraded samples (samples with different initial, but known, mean molecular weights degraded to a specific final mean molecular weight) with the non-degraded samples at the mean molecular weight of the final state of the degraded samples showed that while some conditions showed good agreement in the slope increment between the degraded and non-degraded samples (Figure 4-3), there were conditions that had significant deviations in the slope increment (drag reduction performance). The non-degraded samples consistently produced larger (more efficient) slope increments. The deviation in slope increment scaled well with the normalized difference between the initial and final molecular weights, $\zeta = (M_{wi} - M_{wf})/M_{wi}$, with the deviation increasing rapidly when $\zeta > 0.6$. However, it was expected that the exact value of this acceleration is specific to the degradation method, including the ratio of the residence time to the relaxation time. The deviations in drag reduction performance between the degraded and non-degraded samples (at the same molecular weight) were attributed to deviations in the molecular weight distribution, which was supported by other observations in the literature (Paterson & Abernathy, 1970; Hunston & Zakin, 1980). Furthermore, this behavior is likely enhanced prior to achieving steady-state molecular weight when there would be an excess of longer polymer chains (Gampert & Wagner, 1985), which was the case for the majority of conditions presented. Finally, it was shown that the amount of deviation can be reduced if steady-state conditions can be achieved. However, if the elongational rate far exceeds the critical elongational rate then the final molecular weight distribution could be broader (Sim et al., 2007), which could still impact the drag reduction performance.

These results provide criteria that should be followed if comparisons in drag reduction performance will be made between mechanically (flow-assisted) degraded and non-degraded samples. These results were particularly valuable when using high molecular weight PEO samples at relatively low concentrations (i.e. common drag reduction operation conditions) since the common viscosity and GPC approaches are not well suited for these conditions (Gampert &

Wagner, 1985). This also enables a robust means of establishing polymeric oceans that can be compared with previous non-degraded samples. The results are used for the following chapters to study modified developing TBLs in drag-reducing polymer ocean.

CHAPTER V

5 MODIFICATION OF TURBULENT BOUNDARY LAYER MEAN STATISTICS WITH DRAG REDUCING POLYMER SOLUTION

5.1 Introduction

The objective for the current chapter finds is to identify the changes in the mean and fluctuating velocity profiles with regard to the polymeric flows. The reason for laying out the statistical aspect of the problem is the inconsistency observed between the classical and modern-day view on how polymeric properties influence the statistical framework of near-wall turbulence. The work of Virk (1975) shows that the primary influence of the polymer additives on the flow statistics of the log-region is to increase the slope-intercept constant until MDR. This increase, as per the classical view, was observed to vary monotonically with drag reduction. It was also part of the classical view that as the slope-intercept increases with increasing levels of drag reduction, the extent of the log-layer, also referred to as the Newtonian plug due to it being similar to the velocity profiles of the Newtonian flow, shrinks. The modern-day view, however, provides further, and to some extend contradicting insights on this matter. While the notion of the log-law slope-intercept increasing with increasing levels of drag reduction falls short of capturing the entire picture. Recent studies, such as that of White et al. (2012), Elbing et al. (2013), and Elsnab et al. (2019), show that in addition to the slope-intercept, the slope itself is sensitive to the varying levels of drag reduction.

They show that such changes to the slope depend on the level of drag reduction (DR) in that the slope itself is observed to vary for values of DR > 40%. Elsnab et al. (2019) showed that these deviations in the slope of the log-layer are also observed for the DR levels as low as 15%. It is also important to note that such changes pertain to any given Reynolds number, provided that the Reynolds number is high enough to ensure a sufficient range of scale separation. Studies (Coles 1962; Purtell et al., 1981) show that a conservative estimate of $Re_\theta = 600$ should be attained, at the least, to achieve any measurable log-law region. The deviations in the mean flow statistics provide much of the motivation for the current study. Given that such inconsistency is a well-made observation, it is worthwhile to see how these changes manifest with properties that are indicative of the polymer additive interacting with the local flow properties. As introduced in Chapter 1, the Weissenberg number is critical and insightful parameter with which to observe the aforementioned changes. This forms the main analysis conducted in this chapter with regard to the mean flow statistics in polymeric flows.

Also of interest are the observational changes made with regard to the fluctuating flow statistics. Spalart (1988), as well as De Graaff and Eaton (2000), provide an excellent numerical and experimental source of data, respectively. Since the current work is of experimental nature, De Graaff and Eaton (2000) have been made use for data validation purposes, which in turn builds upon the findings from the numerical simulations of Spalart (1988). In the same manner, for the polymeric data, a comparison between the experimental findings of Warholic et al. (1999) and the computational findings of Dubief et al. (2004) have been made. Firstly, to ensure that the trends are following the literature, and secondly to make important inferences about the observed behavior. As a starting point, it is important to establish the range of logarithmic region in terms of y^+ values for which the data is obtained. For the highest friction velocity based Reynolds number, $Re_\tau = 1400$, (achieved for the Newtonian flow), the lower bound of the log-layer was at $y^+ = 112$, this value was determined using the log-layer extent equation in Marusic et al. (2013). As for the polymeric cases, it is a well-established observation (Virk, 1975; White et al., 2012) that the polymeric effect shrinks the Newtonian plug; the lower bound of the log-layer gets shifted outward continuously while the spatial extent of the log-layer gets progressively diminished. To that end, the data presented in this chapter captures much of the extended buffer layer as well as the entire log-layer.

Having established the range of y^+, this study essentially captures the upper bound of the buffer layer and the entire log-layer region. Consequently, it is worthwhile to see what impact does the polymer additives have on the fluctuating flow statistics, given the relatively narrow Reynolds number range acquired. This allows for the observations made to be classified in terms of the variable representative of the intrinsic polymer properties; the Weissenberg number. It is to say, just as for the mean profiles, the quantification of fluctuating flow statistics has been made in light of the Weissenberg number to ascertain how the polymers impact the fluctuating flow statistics pertaining to the streamwise and wall-normal fluctuations and Reynolds stress.

5.2 Newtonian results

5.2.1 Validation of canonical turbulent boundary Layer

To validate if the facility and model (explained in Chapter 3) provide the canonical TBL, TBL thickness was measured on the top and bottom of the test section. The outer variable scaled velocity profile for the top wall boundary layer is provided in Figure 5-1. The power-law best fit curve to all the data included in Figure 5-1 is

$$\frac{u}{U_e} = 1.01 \left(\frac{y}{\delta}\right)^{1/7.03}. \qquad (5.1)$$

which supports the original assumption from the design phase that the velocity profile can be approximated as a 1/7th power-law profile.

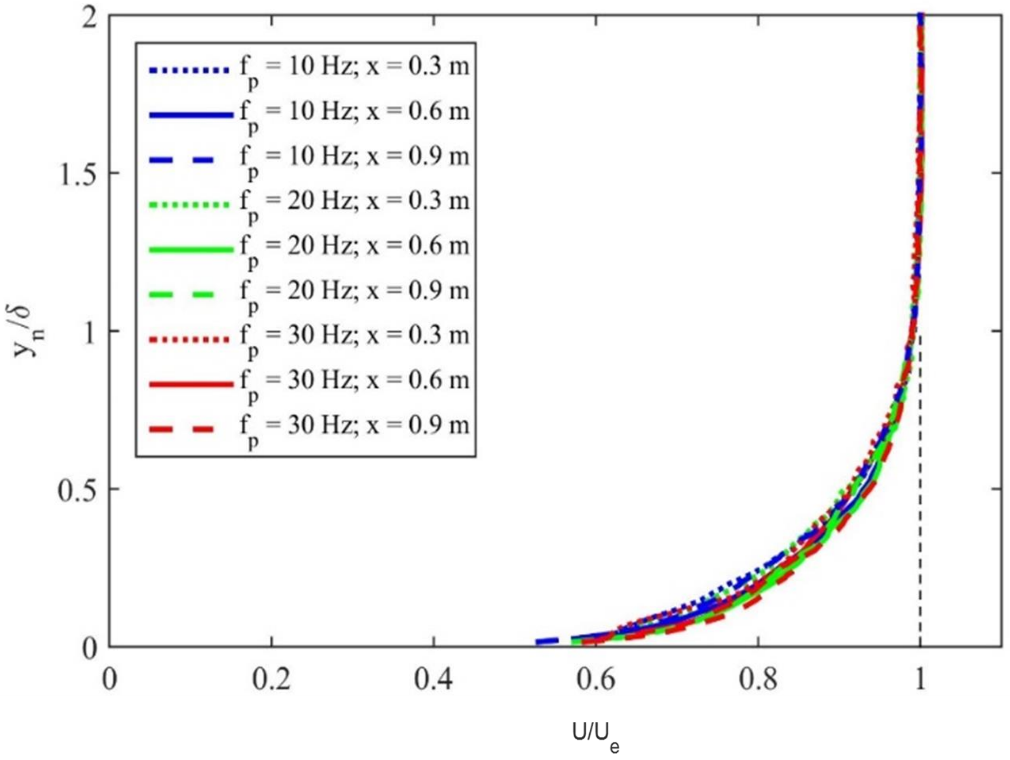

Figure 5-1. Mean streamwise velocity profiles acquired over a range of speeds and streamwise locations scaled with the boundary layer thickness (δ) and the external velocity (U_e).

The momentum thickness (θ), shape factor (H), and other boundary layer parameters are provided in Table 5-1. Beyond x = 0.3 m, θ showed excellent collapse using traditional Reynolds number scaling $\theta/x = 0.0878\ Re_x{}^{-0.1086}$ (see Figure 5-2a). Note that while these scaled results closely follow the canonical curve (White, 2006), the boundary layers were thicker (virtual origins were computed to conform). The curve fit combined with flat-plate momentum integral analysis, $C_f = 2\, d\theta/dx$, allows an estimate of local shear stress, where $C_f (= \tau_w/0.5\rho U^2)$ is the coefficient of friction, ρ is the fluid density, and U is the average streamwise velocity. These results are provided in Figure 5-2b, where $y^+ (= y/l_\nu)$ is the inner variable scaled wall-normal distance, $u^+ (= U/u_\tau)$ is the inner variable scaled velocity, u_τ $(= \sqrt{\tau_w/\rho})$ is the friction velocity, and $l_\nu (= \nu/u_\tau)$ is the viscous wall unit. For reference, dashed lines corresponding to the viscous sublayer $(U^+ = y^+)$ and the traditional log-law $(U^+ = ln(y^+)/\kappa + B)$ with κ = 0.41 and B = 5.0 are included for comparison. Here it is apparent that the measurements do not extend into the viscous sublayer, which is typical of high-Reynolds number TBL velocity profiles. In addition, there is a significant overlap region that follows the log-law with the higher speed (i.e. high Reynolds number) profiles extending to larger y^+ values. It should be noted that there is not a perfect collapse of the data within the overlap region, which is due to the limited accuracy of the θ-gradient, $d\theta/dx$ (<2% change in u_τ collapses the data and the uncertainty of u_τ is ~5%).

Table 5-1. Measured properties of the boundary layer on the top wall of the test section.

x (mm)	U_e (m/s)	$Re_x \times 10^{-5}$ (--)	δ (mm)	δ^* (mm)	θ (mm)	H (--)	u_τ (m/s)	l_v (μm)
302	1.65	5.0	12.4	1.53	1.14	1.35	NA	NA
555	1.68	9.4	11.7	1.60	1.20	1.33	NA	NA
935	1.73	16.2	15.8	2.02	1.53	1.32	NA	NA
302	3.30	10.0	9.1	1.18	0.87	1.35	NA	NA
555	3.36	18.6	11.2	1.32	0.99	1.33	0.34	2.9
935	3.46	32.4	16.1	2.06	1.56	1.32	0.34	2.9
302	6.64	20.0	10.6	1.36	1.01	1.34	NA	NA
555	6.73	37.4	11.8	1.29	1.00	1.29	0.66	1.5
935	6.90	64.5	15.9	1.83	1.43	1.28	0.66	1.5
302	10.0	30.1	9.4	1.21	0.91	1.34	NA	NA
555	10.1	56.2	10.7	1.24	0.97	1.28	0.97	1.0
935	10.4	96.8	17.4	1.81	1.42	1.27	0.96	1.0

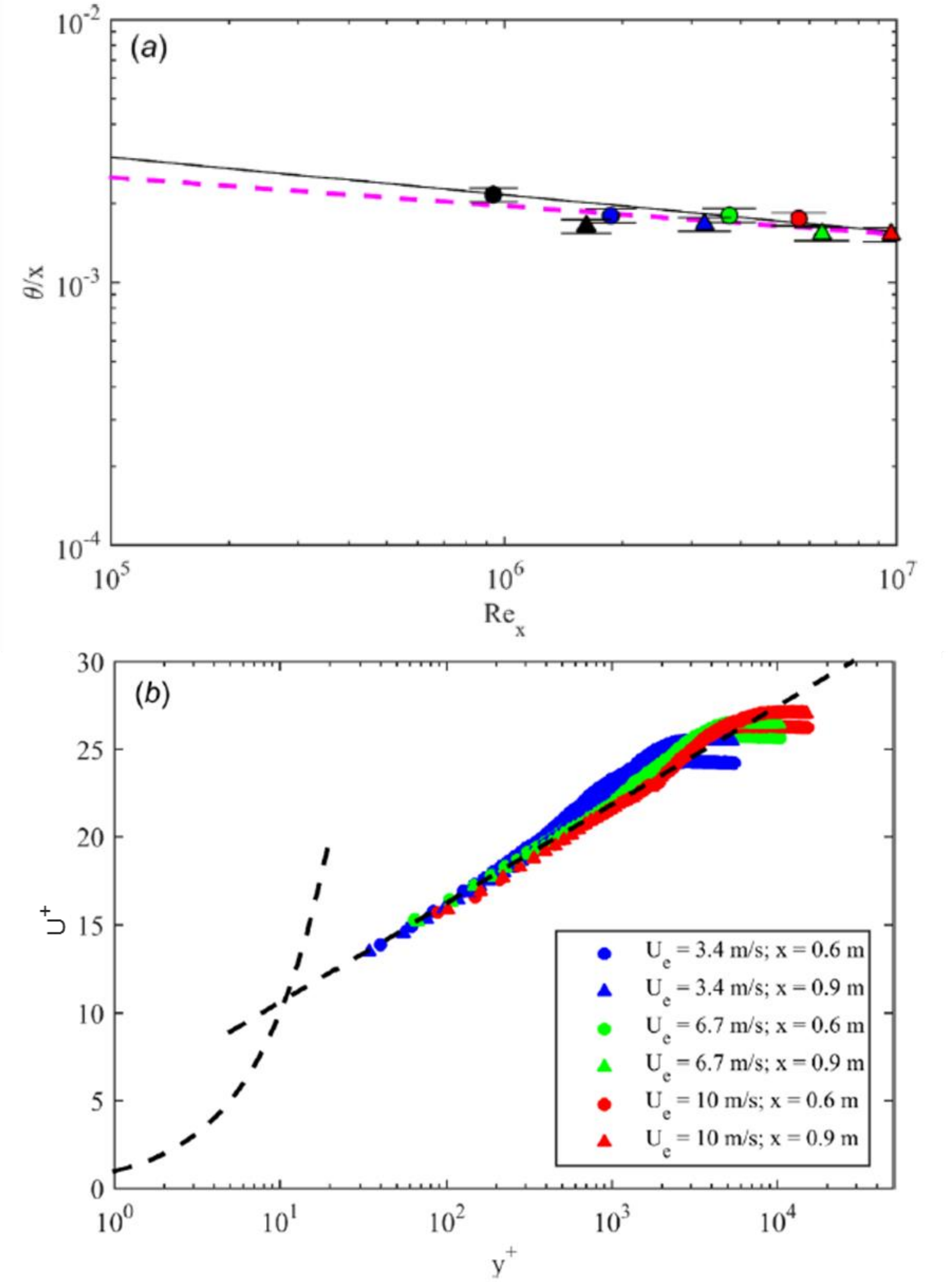

Figure 5-2 (a) Scaled momentum thickness versus Reynolds number with the dashed and solid lines being the power-law fit and canonical ZPG flat-plate solution (White, 2006), respectively. (b) Inner variable scaled velocity profiles compared to the traditional log-law profile with κ = 0.41 and B = 5.0.

5.2.2 Newtonian mean statistics

In view of the literature, the mean flow following the law of the wall is well illustrated. In this work, data from 2D-PIV near the wall focusing on the inner region of the boundary layer is compared with data in the literature (De Graaff & Eaton, 2000; Sillero et al., 2014). In Figure 5-4, mean profiles scaled in inner variables and resolved up to $y^+ = 10$ show very good agreement with the law of the wall in the logarithmic region. The wall shear stress used to determine the inner scales was estimated from the momentum integral analysis for a flat plate. Velocity profiles are repeated in three independent measurements. The maximum standard deviation of the three measurements of free stream velocity U_e for any test speed was within 1.5% of the mean. This is comparable to the PIV uncertainty, thus there was negligible mean shear outside of the boundary layer. Figure 5-4 shows the velocity profile for Re_θ = 800, 2000, and 2900. For these conditions, Reynolds number is relatively low (though comparable to many polymeric boundary layer studies; e.g., Hou et al., 2008) and consequently has a very thin (or possibly non-existent log-region). An indicator function, $\zeta = y^+ \, dU^+/dy^+$, was used to precisely ascertain that the points being correlated depict flow dynamics within the log-region (i.e. region of nearly constant ζ). The indicator function for the $Re_\theta = 2000$ (i.e. main condition used for comparison with the polymeric results) is shown in Figure 5-3 along with the indictor function produced from DNS data (Sillero et al., 2014) at Re_θ = 1968 for comparison. There is good agreement between the current results and the DNS data with the current results having a slightly larger log-region. Based on the indicator function results, the log-region for the $Re_\theta = 2000$ was identified as spanning 80 < y^+ < 230. Given the estimated shear stress at the wall, these conditions have corresponding $Re_\tau (= u_\tau \delta_{99}/\nu) = 350, 800,$ and 1540. Here δ_{99} is the distance from the wall where $U = 0.99U_e$.

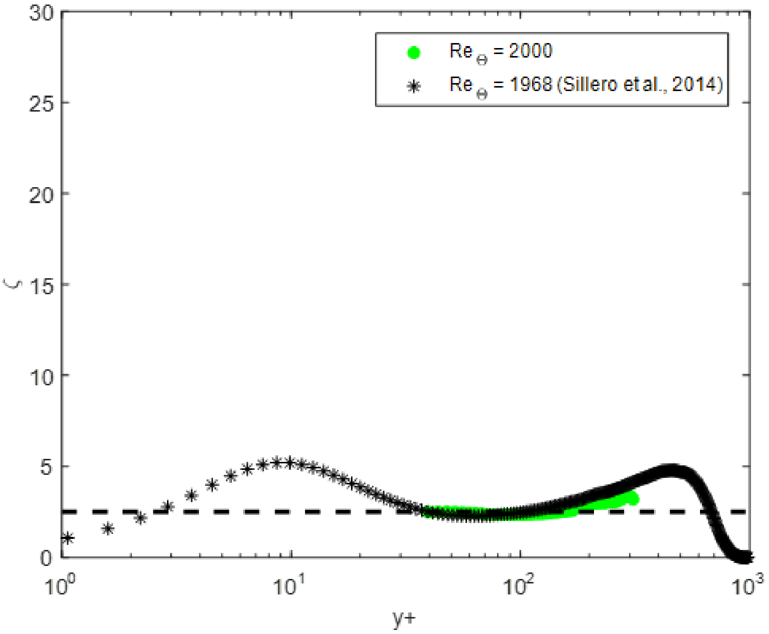

Figure 5-3 Indicator function used to identify the log-region of the turbulent boundary layer. It is compared with DNS data (Sillero et al., 2014), which is at a slightly lower Reynolds number.

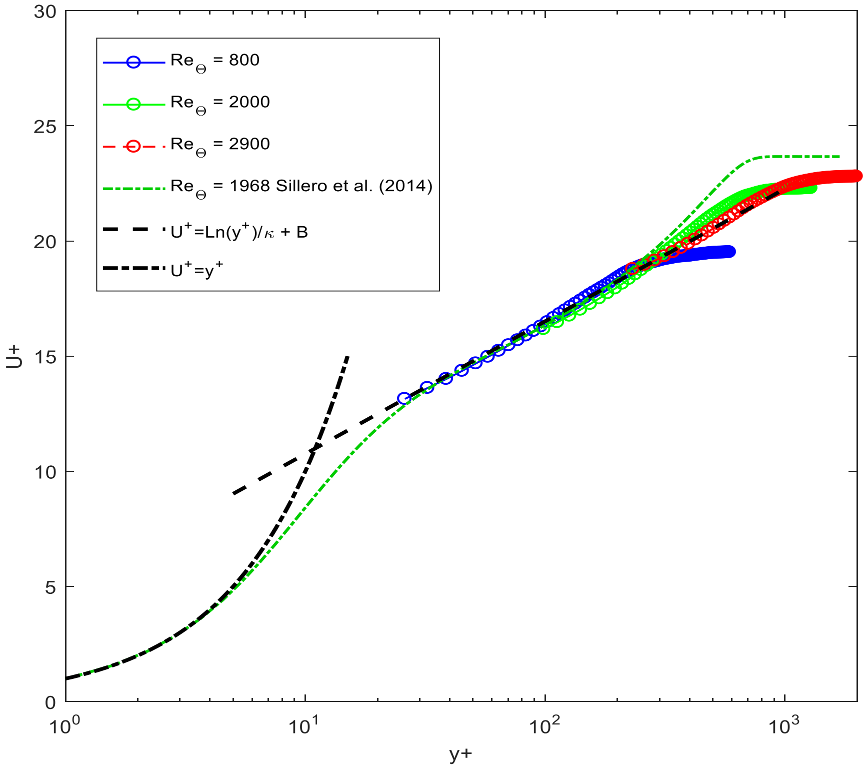

Figure 5-4 Inner variable scaled streamwise velocity profiles for water (Newtonian). The profiles are compared with the viscous sub-layer profile $(U^+ = y^+)$ and the traditional log-law profile $(U^+ = ln(y^+)/\kappa + B)$ with κ = 0.4 and B = 5.0.

To fulfill the conventional obligation of normalizing the Reynolds stresses (streamwise and wall-normal) with the inner scales, profiles have been obtained to resolve the near-wall behavior. These profiles show that the stresses tend to peak in the near-wall region (buffer region). De Graaff and Eaton (2000) showed Reynolds number dependency of Reynolds stresses in the range of Reynolds from $Re_\theta = 1000$ to 13,000. In Figure 5-5, the current work is compared with De Graaff and Eaton (2000) for validation purposes. Here, $\acute{u}\ and\ \acute{v}$ are the root mean square (rms) of streamwise and wall-normal fluctuating velocities, respectively, and $\acute{u}^{2^+}$ and $\acute{v}^{2^+}$ are streamwise and wall normal inner scaled Reynolds stresses, respectively. The near-wall peak occurs at $y^+ = 14$. Current data also shows a weak dependency on Reynolds number over the narrow range of 1000 to 3000. Note that the peak magnitude is not resolved for $y^+ < 15$.

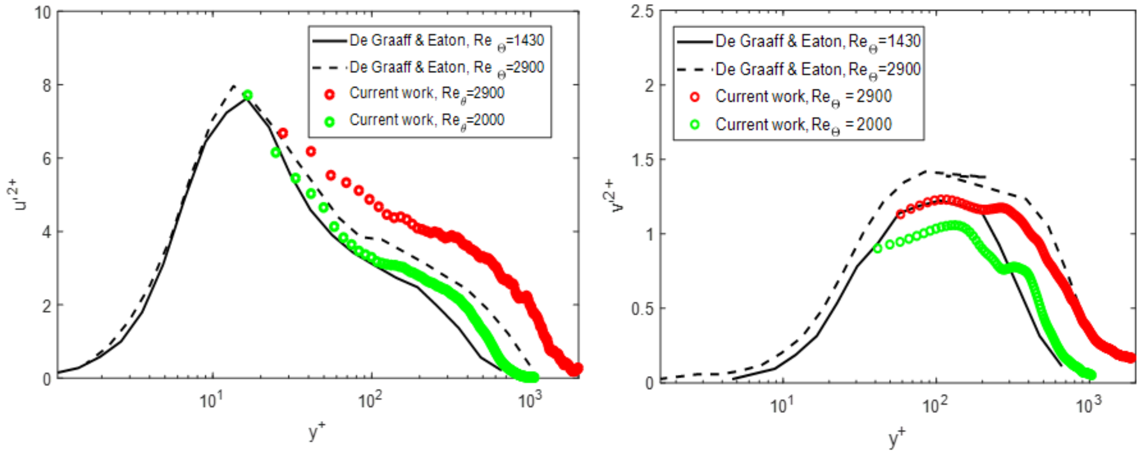

Figure 5-5 Inner variable scaled streamwise ($\acute{u}^{2^+}$) and wall-normal ($\acute{v}^{2^+}$) Reynold stress components for $Re_\theta = 2000$ and 2900 compared with the work of De Graaff and Eaton (2000) at $Re_\theta = 1430$ and 2900.

5.3 Polymeric results

5.3.1 Polymeric mean velocity profiles

The mean statistics have historically been well represented and the reasons for the inclusion of the mean statistics are for the validations of the data obtained with the literature. As can be seen in Figure 5-6, the general trends observed with the data obtained are consistent with the literature in that the overlap region is shown to be of continuously diminishing extent. This also means that the underlying buffer layer gets increasingly thickened with increasing values of drag reduction. Such an effect on the overlap region could be a natural observation to make, given that the buffer layer provides the boundary conditions for the overlap layer. Such a notion is consistent with the LDR regime (< 40%) and HDR regime (>40%), where the log-law intercept appears to change, and the von-Karman constant appears to be sensitive to the varying dynamics of the buffer layer with different rates comparing LDR and HDR. Moreover, the universality of the mean profiles that exist for the Newtonian flow, is lost in the polymeric flows. Having a low *Re* and varying polymer parameter, *Wi*, shows that the rheological properties of the polymer have a growing influence on the mean statistics of the flow. Furthermore, a simple inner variable scaling is insufficient for a collapse of the cases observed with the Newtonian flows and that universality of such mean statistics requires a relevant polymeric property to be included in any such scaling that is attempted.

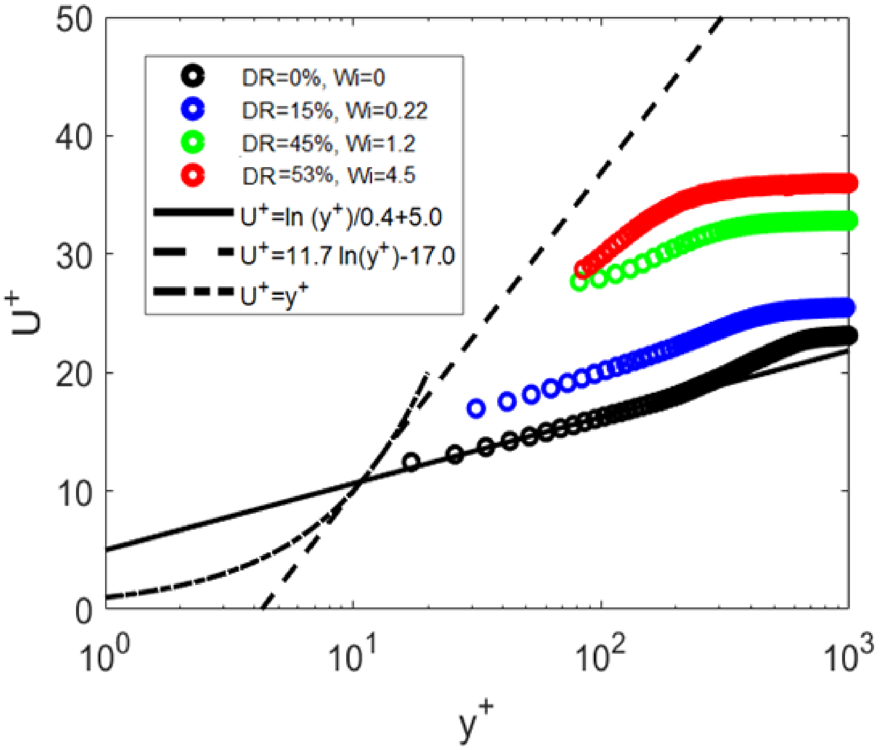

Figure 5-6 Scaled velocity profiles with varying levels of drag reduction and *Wi*. Polymer concentration was constant and homogeneous (200 ppm) and $Re_\tau = 800$ for all conditions. The maximum drag reduction asymptote or ultimate profile (dashed line), the law of the wall (solid line), and the viscous sublayer profile (dot-dashed line) are also shown.

5.3.2 Polymeric fluctuating velocity profiles

The modifications brought into the fluctuating velocity profiles of the Newtonian flows are both interesting and natural to observe. As has been detailed above, the Reynolds stress flow structure has two key components; $\acute{u}$ and $\acute{v}$. Each of these components has its own merits of contribution to the flow dynamics. and, consequently, their modification in the polymeric flows can reveal the scheme of action of polymer additives on the active and inactive parts of the flow. Townsend (1961) proposed that the turbulent motion in the near-wall region consists of the superposition of active and inactive motions. The active motions produce the shear stress and scale on inner variables. The inactive motion is a “meandering” or swirling motion made up from attached eddies of large size that contribute to the Reynolds stress much further from the wall than the point of observation. Since the Reynolds number was low for a significant scale separation, this part of the study focuses on the action of the polymers additives on the active part of the motions. For this, the conventional flow statistics for the fluctuating velocities, scaled with the wall friction velocity are plotted and compared with the Newtonian flows, for the near-wall region. Upon examining these fluctuating profiles, it is observed that the polymeric flows have a distinct mode behavior in that they appear to enhance the streamwise fluctuating velocity while suppressing the wall-normal fluctuating velocities and Reynolds shear stress. In Figure 5-7 the range of DR and Wi is compared with Warholic et al. (1999). This reveals the first details of the potential mechanism for polymer induced turbulent drag reduction in LDR and HDR. The fluctuating velocity correlation terms of the turbulent kinetic energy budget equation is fundamental in redistributing the turbulent kinetic energy from the streamwise direction to other orthogonal directions. The fact that $\acute{u}^{+}$ is enhanced shows that the potential mechanism of the transfer of turbulent kinetic energy is directly targeted by polymer additives, knowing that the Re_{τ} is constant for the current study cases in Figure 5.7. Moreover, the behavior of polymeric cases compared to the Newtonian case confirms that the natural tendency of the Newtonian flow is to attain isotropic fluctuating flow fields in the near-wall region while polymer additives reduce this tendency of the flow (Gampert & Yong, 1990). The fluctuating flow field of the polymeric flow appear to be anisotropic and that this anisotropy is increasingly more prevalent and intense as higher values of drag reduction are realized.

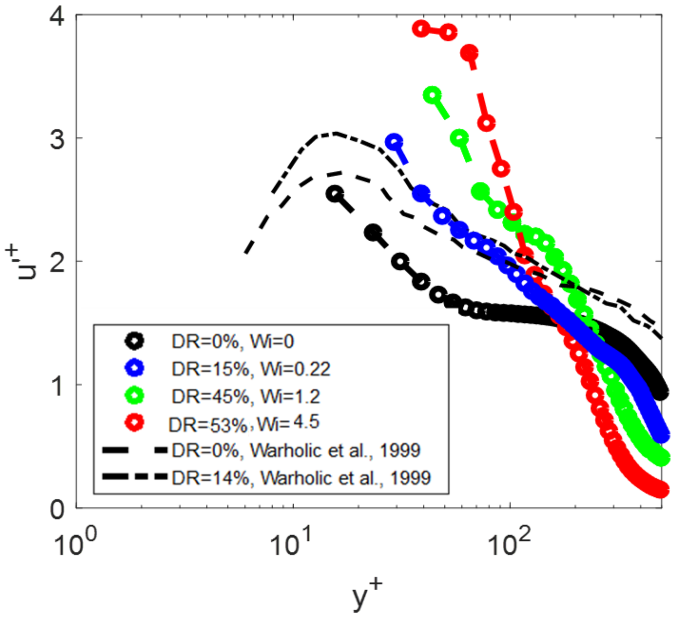

Figure 5-7 Inner-variable scaled rms of the streamwise fluctuating velocity, $\acute{u}^+$, versus the inner-variable scaled distance from the wall, y^+, for varying levels of DR (LDR and HDR) and Wi, compared with the work of Warholic et al. (1999).

The rms of the wall-normal fluctuating velocity relative to the rms of the streamwise fluctuating velocity in inner variable scaling are shown in Figure 5-8 and compared with the simulation work of Dubief et al. (2004). The turbulent velocity fluctuations in the transverse directions exhibit different behavior then in the streamwise direction. The peak of $\acute{u}^+$ shifts away from the wall and its magnitude increases slowly compared to the Newtonian flow when normalized by u_τ. The wall-normal component $\acute{v}^+$ has the opposite trend. In drag-reduced flow, the maximum $\acute{u}^+$ is higher than or comparable with the DR = 0% case, as found in experiments (Warholic et al., 1999). The strong reduction of the transverse fluctuations suggests that polymers preferentially target the vortices, as they produce significant fluctuations.

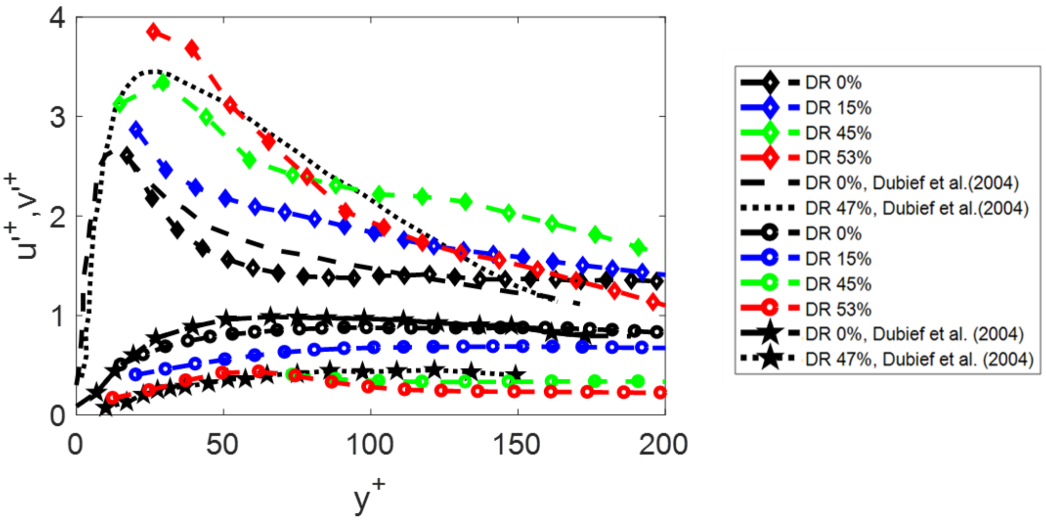

Figure 5-8 Root mean square of the velocity fluctuations scaled with inner variables at DR = 0%, LDR (<40%), and HDR (>40%) compared with the simulation work of Dubief et al. (2004). Dashed lines with diamond symbols are $\acute{u}^{+}$from current work and ones without symbols are $\acute{u}^{+}$from the work of Dubief et al. (2004). Dashed lines with circle symbols are $\acute{v}^{+}$ from current work, and ones with pentagram symbols are $\acute{v}^{+}$from work of Dubief et al. (2004).

The increased anisotropy of fluctuating flow field can also be indicative of the fact that such fluctuations become more and more parallel to the flow direction with increasing drag reduction. This is an indication that the polymer additives do not allow for, or at least prevent the extend of interaction in the cross normal direction, which can be inferred from the reduced wall-normal velocity fluctuations. To this point, it is established that the mode of action of the polymer additives is to re-shape the turbulent kinetic energy distribution from the streamwise direction to the wall-normal direction, in that they suppress the severity of this transfer of energy. This can be inferred from having Reynolds number relatively low ($Re_{\tau} = 800$) and constant ($< 5\%$ deviations) for both polymeric and Newtonian cases.

The fact that these velocities are scaled with the inner variables also shows the growing influence of polymer additives on the active motion part of the turbulent flows. As has been remarked above, the inevitable degradation of the polymer additives limits this study to a narrow range of *Re*. However, being low Reynolds number polymer solution, the effect of polymer on the inactive motions taken to be of growing influence with the increasing Reynolds number has been precluded from the current study. Given the general examination of the cycle of events responsible for the sustaining of the near-wall turbulence at comparatively low Reynolds number regime, the cycle does appear to be autonomous in the sense that it is influenced by the active motion. While the streamwise fluctuations find their contributions from both the active and inactive motions and given the Reynolds number limitation of the current study, the modifications to the wall-normal fluctuations are the sign of the active scale of the involved motions. The fact that they are suppressed, shows that the active scale motions are less intense, which means that the structural features of the involved motions are directly affected.

5.4 Discussion

The results above are the first steps to reveal the initial details of the potential mechanism for polymer induced turbulent drag reduction in LDR (< 40% DR) and HDR (> 40% DR) regimes. The fact that streamwise fluctuating velocity is enhanced as compared to wall-normal, which is significantly suppressed, shows that the mechanism of transferring the turbulent kinetic energy from the streamwise direction to the wall-normal direction is potentially targeted by the polymer additives. Moreover, this means that while in the Newtonian flows the natural tendency of the flow is to attain isotropic fluctuating flow fields in the near-wall region (Gampert & Yong, 1990), the polymeric flows reduce this tendency of the flow. The fluctuating flow field of the polymeric flows are appearing to be anisotropic and, based on discussion in literature (Gampert & Yong, 1990), this anisotropy is increasingly more as higher values of Weissenberg numbers are realized. Although, only conditions with three Weissenberg numbers have been considered here, what is important to note is the range of tested Weissenberg number (or alternatively the DR values). The range of Weissenberg number considered here encompasses the LDR as well as the HDR regime. Therefore, the deduction that polymer additives enhance the anisotropic nature of the fluctuating flow fields for the near-wall region. It is also interesting to note the behavioral changes brought in the streamwise velocity fluctuations. It is shown that while comparing the cases of 15% DR and 0% DR, the statistical differences are more confined to the buffer layer and the streamwise velocity fluctuations approach each other rather closely in the log-layer region and beyond. However, this similarity is lost for the other two conditions that depict the HDR regime. The observed evolution of the statistics with varying DR levels is direct evidence of the increasing buffer layer, which has been recorded in many previous works (Virk, 1971, 1975; Donohue et al., 1972; Graham, 2004). Another important takeaway from the above observations is the fact that the buffer layer dynamics are especially susceptible to the mode of action of the polymers, while the logarithmic layer shows it being immune to the effects of the polymer, at least when in the LDR regime. Although this is an interesting observation, this requires further investigation and shall be discussed at length in Chapter 6.

As has been given a mention above, the trends for the wall-normal fluctuations showed the opposite trend. While the streamwise fluctuations have increased, wall-normal fluctuations have been suppressed as higher *Wi* were achieved. As the first point of focus, the similarity between the DR = 15% case and the Newtonian flow (DR = 0%) was shown in Figure 5-8. The two curves appear to have the same general shape (i.e. the general trend of their variation across the boundary layer). Also, the wall-normal fluctuations for the LDR case remain below that of the Newtonian case at any given distance from the wall. Such an observation is not consistent with the conditions showcasing the behavior in the HDR regime, given the range of Weissenberg numbers, the gradual variations in the wall-normal and streamwise fluctuations at any given distance away from the wall appear to be a strong function of the *Wi*. It is to be reminded that these conditions pertain to a constant Re_τ of 800.

The drastic change in fluctuating velocities with *Wi* is indicative of increased anisotropy of fluctuating flow field and the fact that such fluctuations become more and more parallel to the flow direction with increasing drag reduction (Gampert & Yong, 1990). This is indicated by the reduced wall-normal velocity.

The fact that these velocities are scaled with the inner variables also shows the growing influence of polymer additives on the active motion part of the turbulent flows. As has been remarked above, the inevitable degradation of the polymer additives limits this study to the range of Reynolds numbers that are incapable of achieving large scale separation. Moreover, being low Reynolds, the dependence of statistical modifications of the turbulent fluctuations could be viewed as being depend on the intrinsic polymer property, such as the *Wi*. Given the general examination of the cycle of events responsible for the sustaining of the near-wall turbulence at comparatively low Reynolds number regime, the cycle does appear to be autonomous in the sense that it is at large composed and influenced by the active motion (Jiménez & Pinelli, 1999). This has been leveraged to infer the effect of polymers on the active scale motions of the near-wall region (sublayer and log-region). The fact that the wall-normal fluctuations are suppressed, shows the active scale motions to be less intense, which in turn must mean that the structural features of the involved motions are directly affected. Given what has been observed above with regard to streamwise and wall-normal fluctuations, the polymer additives inhibit the active scale motions by interacting with the energetics of the flow. In this sense then, the next step is to investigate the impact of coherent motions. This was the motivation for Chapter 6.

CHAPTER VI

6 MODIFICATION OF TURBULENT COHERENT STRUCTURE WITH DRAG REDUCING POLYMER SOLUTION

6.1 Introduction

It is well accepted that coherent structures exist in all kinds of turbulent flows, such as jets, wakes, and boundary layers. Statistical descriptions and models of turbulence that ignore or only partially take into account the presence of such coherent motions in the flow usually cannot yield accurate prediction of turbulent flows. Since it is apparent that these coherent structures are responsible for the maintenance (production and dissipation) of turbulence, the study of these structures is of fundamental importance to the understanding of the flow dynamics (Robinson, 1991). One challenge is that the turbulent coherent structures exist at a wide range of scales. Take the TBL for example, previous studies show that at high Reynolds number the very large scale motions can extend to a length of several or even dozens of boundary layer thicknesses in the streamwise direction (Kim & Adrian, 1999; Hutchin & Marusic, 2007) while some vortices can have a characteristic size as small as the Kolmogorov scale, which is usually beyond the resolution of measurements. There are also a number of coherent structures with intermediate scales, such as the hairpin vortices and hairpin packets (Zhou et al., 1999; Adrian, 2007).

Relaying that turbulence exhibits distinctive structural anatomy has prompted several attempts to visualize such structures. It was not until the observations of Head and Bandyopadhyay (1981), which leveraged the physical insight of Theodorsen (1952), that the first convincing visual evidence of the near-wall three-dimensional (3D) hairpin/horseshoe vortices were produced. They detailed the evolution of these vortices influenced by events of stretching due to mean shear flow and the resulting induced velocities due to their intensified vorticity, causing them to lift-up in the wall-normal direction. Subsequent comparative studies (Brown & Thomas, 1977; Deshpande et al. 2019) would suggest that the observation of Head and Bandyopadhyay (1981) was made for the dominant structure that developed through the TBL at a 45° orientation. Such concrete observations led to a proposed model (Smith, 1984) that puts these 3D vorticity structures at the center of the momentum exchange process (i.e., they facilitate, and potentially control, the momentum exchange between the inner and outer regions with the outer region here including the log-region and beyond) of a TBL. Another investigation (Adrian et al., 2000) revealed that such structures organize themselves to form long and meandering super-structures that are correlated spatially to produce regions of uniform momentum located in the TBL log-layer. Such super-structures have long been observed in moderately buoyancy-driven geophysical TBLs and the inner-outer coupling is tied to strong thermal updrafts (Jayaraman & Brasseur, 2019). However, in the absence of buoyancy-driven thermals, as is the case in incompressible TBLs, understanding how near-surface coherent structures modulate outer layer dynamics is still a topic of active research with implications to flow control.

Given the centrality of such 3D vorticity structures to the characteristics of the near-wall TBL dynamics, it is natural to explore how these dominant coherent structures are modulated during polymer drag reduction (PDR) to explain the observations of Toms (1948). Several successful attempts, such as Tiederman et al. (1985) and Wei and Willmarth (1992), found that polymer additives in the near-wall region increase the spanwise spacing of the low-momentum streaks with a concomitant decrease and increase in the spatial frequency of the “burst” events and diameters of the vorticity structures, respectively, as drag reduction (DR) increases. Experimental observations such as Warholic et al. (2001) suggested a deficit in Reynolds shear stress for polymeric flows. This deficit was later linked computationally to polymeric stresses (Sibilla & Baron, 2002) as they engaged the pressure strain and diffusion terms of the Reynolds stress transport equation to enhance anisotropy of the fluctuating velocity field in the near-wall region (Gampert & Yong, 1990). This is in sharp contrast to turbulent flows over rough surfaces that exhibit an increase in drag and an accompanying decrease in fluctuating flow field anisotropy of near-wall turbulence (Shaban et al., 2018). Such developments suggest that polymer rheology is another key factor impacting PDR just as roughness scales impact drag enhancement.

Polymers have a natural tendency to relax and maintain equilibrium conformations but tend to be stretched when in shear flow. However, to effect drag reduction, such relaxation times have to be greater than the local turbulent flow time scales. This effect is quantified by the Weissenberg number; a ratio of the polymer relaxation time to the flow time scales. Polymer stretching has been found to provide counter-torques that oppose the motion of hairpin/quasi-streamwise vortices (QSV), rendering them less intense (Dubief et al., 2004; Kim et al., 2007). This helps to explain the improved stability of the near-wall streaks, inhibited Q2 events (pumping of the hairpins), and, consequently, the damped Reynolds shear stresses. The reduced swirling strengths of the vortices are also expected to alter the auto-generation cycle of the hairpins, assuming the modified cycle would have a critical strength threshold of the initial vortices required for its self-sustained continuation (Zhou et al., 1999). Flow simulations of Kim and Sureshkumar (2013) have shown that this is the case with polymer molecules being actively engaged in re-routing the energetics of the flow to result in drag reduction.

Such a morphological introduction to PDR provides both fundamental and practical motivation for the current study. Much less is known about how the polymer additives modify the dynamics of dominant structures (that extend through the log-region and beyond) and the corresponding flow statistics. A wide spectrum of structures in this region, together with increasing

Reynolds number, make flow simulations for these regions computationally expensive. While earlier investigations revealed that in the HDR (> 40%) regime the velocity profiles deviate from the classical view of polymer drag reduction modifications, a recent investigation shows that statistically significant variation in log-layer slope occurs even at DR levels as low as 15% (Elsnab et al., 2019). Deviations from the classical view, which indicate that polymer properties must play a role, show that the characterization of the polymers is critical in analyzing modifications to the flow structures. Since many of the polymer properties are sensitive to the polymer concentration (e.g., Weissenberg number), the current study was performed with a developing TBL in a polymer ocean (uniform concentration) of polyethylene oxide (PEO) in which the effect of polymer properties introduced by Weissenberg number are studied.

In this chapter, the modification of dominant coherent structures that extend through the log-region of a drag reduced TBL is studied from time-resolved particle-image-velocimetry via examination of two-point correlations and proper orthogonal decomposition. Measurements were acquired in polymer oceans (uniform concentration, 200 ppm) at drag reduction levels corresponding to the LDR regime, the HDR regime, and at an intermediate level (~40%). This chapter is divided into two primary sections; (1) two-point correlations of polymeric velocity profiles compared with that of water (Newtonian, DR = 0%) and (2) the connection between dominant proper orthogonal decomposition (POD) modes and instantaneous turbulence structures. These results show that with increasing drag reduction the inclination of these dominant coherent structures decreases, their streamwise extent increases and the fluctuations in the correlations are suppressed (especially at HDR). These observations are examined in comparison with the coherent structure literature (Newtonian and polymeric).

Ultimately, the current study aims to understand and provide insights on how polymer affects the coherency of induced motions as well as controls their spatial extent in the log-layer region and beyond. The remainder of this chapter provides results and discussion (Newtonian and polymeric) and finally, the conclusions are summarized. The majority of this chapter has been published in Farsiani et al. (2020b).

6.2 Newtonian results

6.2.1 Newtonian two-point correlations

The reference location for the two-point correlations shown in Figure 6-1 was fixed within the log-region ($y^+_{ref} = 148$), though on the outer edge for the lowest Reynolds number. In Figure 6-1, the correlations from the three Reynolds numbers (Re_θ = 800, 2000, and 2900) are shown with the streamwise separation length scaled with δ. The same overall trend is observed for all three Reynolds numbers; the peaks decrease with increasing wall-normal separation (Δy), the streamwise separation (Δx) for the peak correlation increases with increasing Δy, and the correlations are asymmetric about $\Delta x = 0$. Coherent motions with streamwise aligned orientation would suggest upstream-downstream asymmetry about $\Delta x = 0$ (zero streamwise separation) and progressively decreasing peak value of correlations with increasing wall-normal separation (Δy) along the angle of their inclination. In the current study, the dominate structure inclination angle found from the peak locations with various separation distances was 46.9° ± 4°. It is important to note here that the mean structure angle within the log-region is well established in the literature (Robinson, 1991; Deshpande et al., 2019) to be between 15° and 18°. However, when an isolated dominant structure has been considered, their inclination angle has been found to be ~ 45° (Head & Bandyopadhyay, 1981; Deshpande et al., 2019). Given that the region correlated in the current study extends from the log-region to the outer region, this suggests that the measured angle corresponds to the dominant structure extending through the log-layer to the outer regions. The subsequent polymeric analysis compares the deviations of these dominate structures with increasing drag reduction.

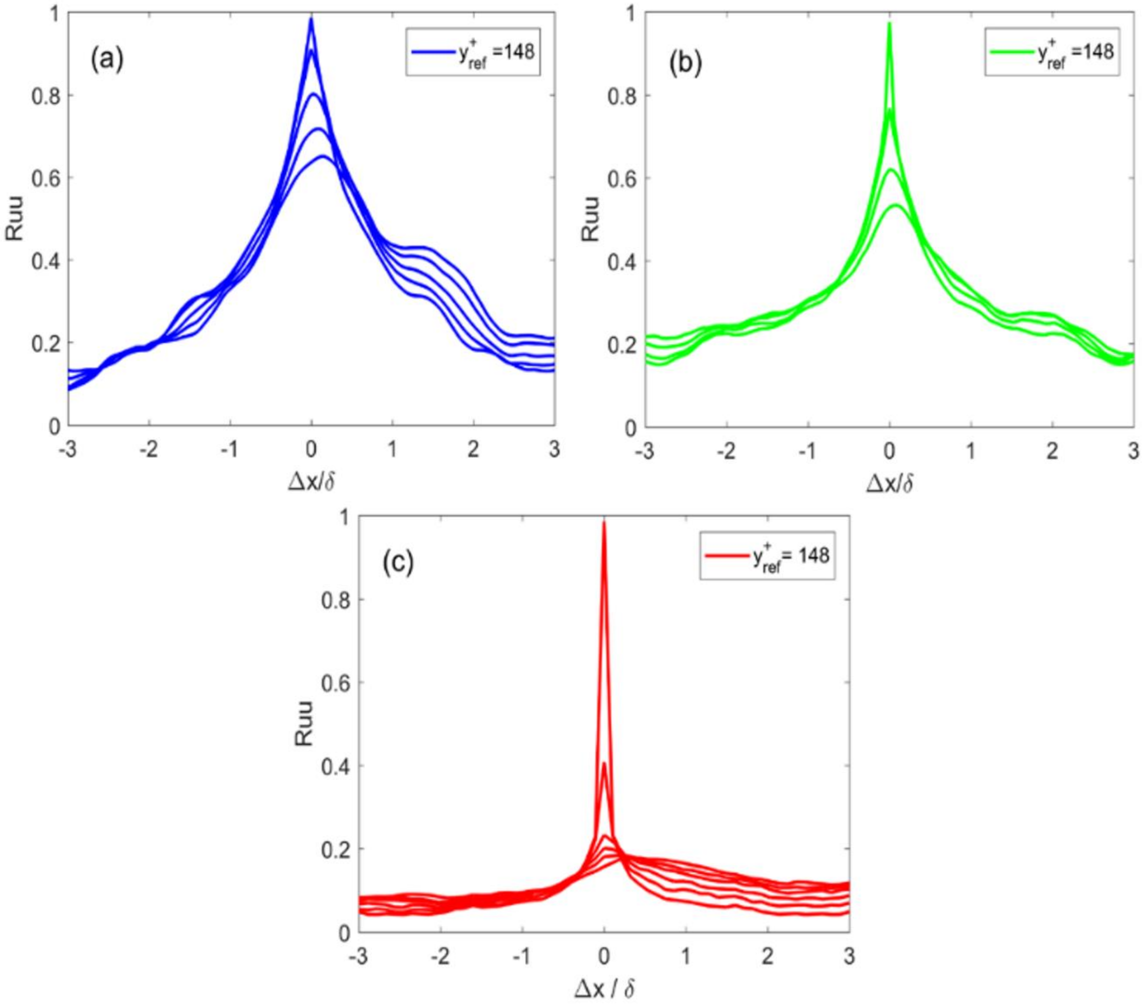

Figure 6-1. The two-point correlations at a fixed inner variable scaled wall-normal reference location ($y^+_{ref} = 148$) with maximum $\Delta y^+ = 100$ for Re_θ of (a) 800, (b) 2000, and (c) 2900. Note that each of the consecutive lines show a spatial spacing of $y^+ = 20$.

In Figure 6-2, the variational traits of the flow correlations in purely streamwise direction ($\Delta y^+ = 0$) are compared with correlations with $\Delta y^+ = 100$ for three different reference heights. The reference heights have been kept the same for the two cases. Figure 6-2a depicts the correlation of motions at the lower and upper bounds of the log-region as well as the correlation of log-layer events with that in the outer region. The decrease in the correlation peak quality factor $(f_0/(f_2 - f_1))$, where f_0 is the frequency of resonant peak, f_1 is frequency value 3 dB down from peak value with $f_1 < f_0$, and f_2 is frequency value 3 dB down from peak value with $f_1 > f_0$ in Figure 6-2a indicates that coherence in these motions is higher and persist over enhanced streamwise lengths in the outer log-region of the TBL. This reinforces the idea of the linked formation of hairpins in a packet like the organization to produce such strong flow patterns in the outer log region and beyond. Moreover, peaks have a slight positive offset about $\Delta x = 0$ in Figure 6-2a, showing that the responsible structures for these correlations lean downstream. Also, purely streamwise correlations in Figure 6-2b, showing a progressive increase as upper portions of the log-layer are realized. This indicates the growing influence of uniform momentum zones (Adrian et al., 2000) on flow patterns in the upper bounds of the log-layer.

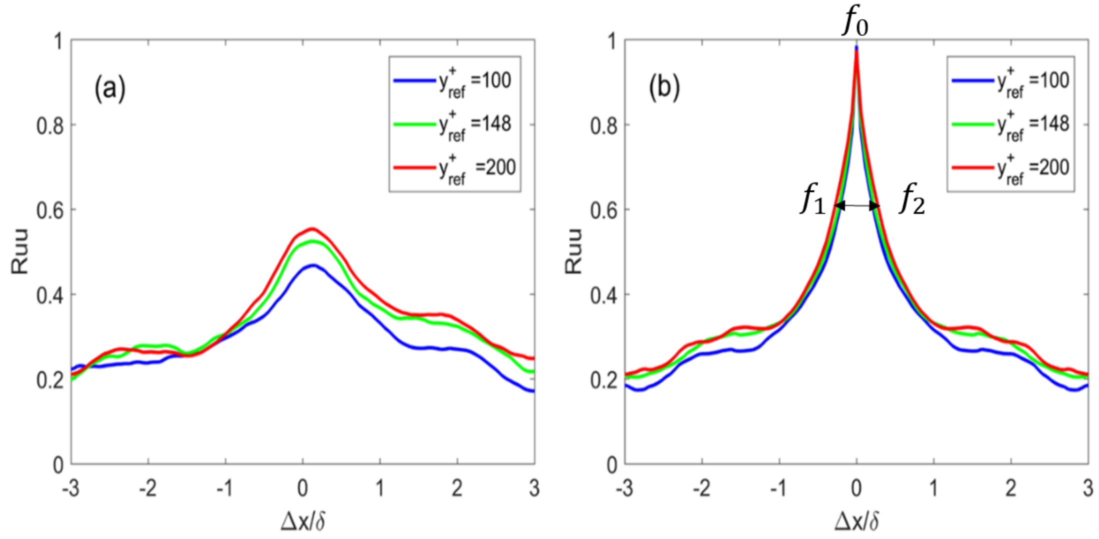

Figure 6-2. Two-point correlations of the streamwise fluctuating velocities in water (Newtonian) at Re_θ = 2000 for varying reference heights and (a) $\Delta y^+ = 100$ and (b) $\Delta y^+ = 0$.

6.3 Polymeric results

6.3.1 Polymeric two-point correlations

There is a general consensus that polymers significantly enhance the anisotropy of the turbulent fluctuations in the near-wall region (Gampert & Yong, 1990; Warholic et al., 2001). Given this streamwise bias of flow statistics, Figure 6-3 shows the streamwise scale of the flow structures in the log-region within the LDR regime (DR = 20%), the boundary between LDR and HDR (DR = 46%), and within the HDR regime (DR = 62%). Here the wall-normal separation was fixed at $\Delta y^+ \cong 100$ with the reference locations selected to relate the flow statistics within the upper half of the log-layer and potentially extending to the outer-wake region for all the DR regimes. Comparison between the LDR regime (Figure 6-3a) and that of water (DR = 0%; Figure 6-2a) shows minimal variation. However, the differences relative to water progressively increases moving from LDR (Figure 6-3a) to the LDR/HDR boundary (Figure 6-3b) and then to HDR (Figure 6-3c). The same general trend is observed as DR levels increase; their peak values increase while the peak quality factors (sharpness) decrease as upper regions of the TBL are correlated. This is particularly apparent for DR = 46%, where not only the streamwise-spatially averaged R_{uu} increases with y_{ref}, indicative of an increase in the span of uniform momentum zones, but the different curves also show a tendency to converge at streamwise separation distances closer to the peak ($\Delta x/\delta \sim 0.7$).

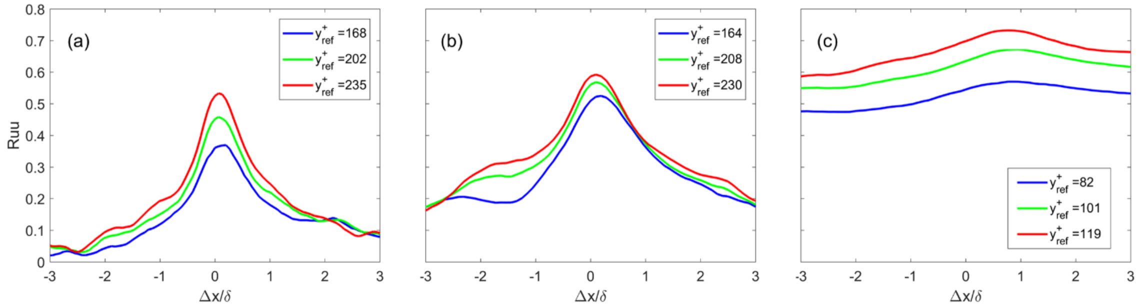

Figure 6-3. Two-point correlations with a fixed wall-normal separation ($\Delta y^+ = 100$) and y_{ref} within the log-layer $(82 \le y^+_{ref} \le 235)$ at drag reduction levels of (a) 20%, (b) 46%, and (c) 62%.

When comparing DR = 46% and DR = 62% cases, the change in the trends is observed and deviations in the trends indicate that the polymer additives are significantly influencing the structure within this region of the TBL. These deviations potentially arise from the modulations in the viscous length scale (l_v) due to the polymer additives as well as outer boundary layer scales. As was shown in the Chapter 5, for HDR the log-layer is significantly reduced and, consequently, the coherence between the inner and outer regions of the TBL are enhanced as seen by strong velocity correlations in Figure 6-3c. Figure 6-3c shows a significant increase in R_{uu} with the increased correlations persisting over a significantly larger streamwise scale, which suggests that the flow becomes more streamwise dominated with increasing DR (Warholic et al., 2001). Also, note that the variation in magnitude of the correlations with streamwise separation occurs over a relatively narrow range as the outer regions (higher y_{ref}) are approached. This remarkable stabilization of the streamwise correlations points to the possible existence of unusual prolongations in the streamwise direction of the uniform momentum zones, which were originally reported to exist in Newtonian flows. To confirm this, one needs visualizations of the flow field over a sufficiently large spanwise-streamwise plane that is currently unavailable. While the streamwise fluctuating velocity correlations increase noticeably in the streamwise direction, it is important to also note its increase along the wall-normal direction (i.e. the spatial scale increases in both the streamwise and wall-normal directions, though more rapidly in the streamwise direction).

Figure 6-4 shows the correlations of the streamwise fluctuating velocities with only streamwise separations (i.e. $\Delta y = 0$), which reveals additional details of how the polymers modify the flow statistics. Note that for clarity only one y_{ref} was selected for each DR level in Figure 6-4, and the selections were such that it depicts the events within the log-layer. Again, the deviations in the flow statistical trends are mild between water (DR = 0%; Figure 6-4a) and the LDR regime (Figure 6-4b), but as the DR level increases the differences become more apparent. In particular, note that the correlations persist longer spatially in the streamwise direction as DR increases. While the averaged normalized correlations increase with increasing DR, the fluctuations in the correlations are progressively reduced. This strongly suggests that the flow stabilization is spatially more prevalent with increasing DR. The extent of such laminarization expands in the *x*-*y* plane as a dominating effect of the polymer additives, which has been well-known to restructure the flow energetics (Sibilla & Baron, 2002; Graham, 2004).

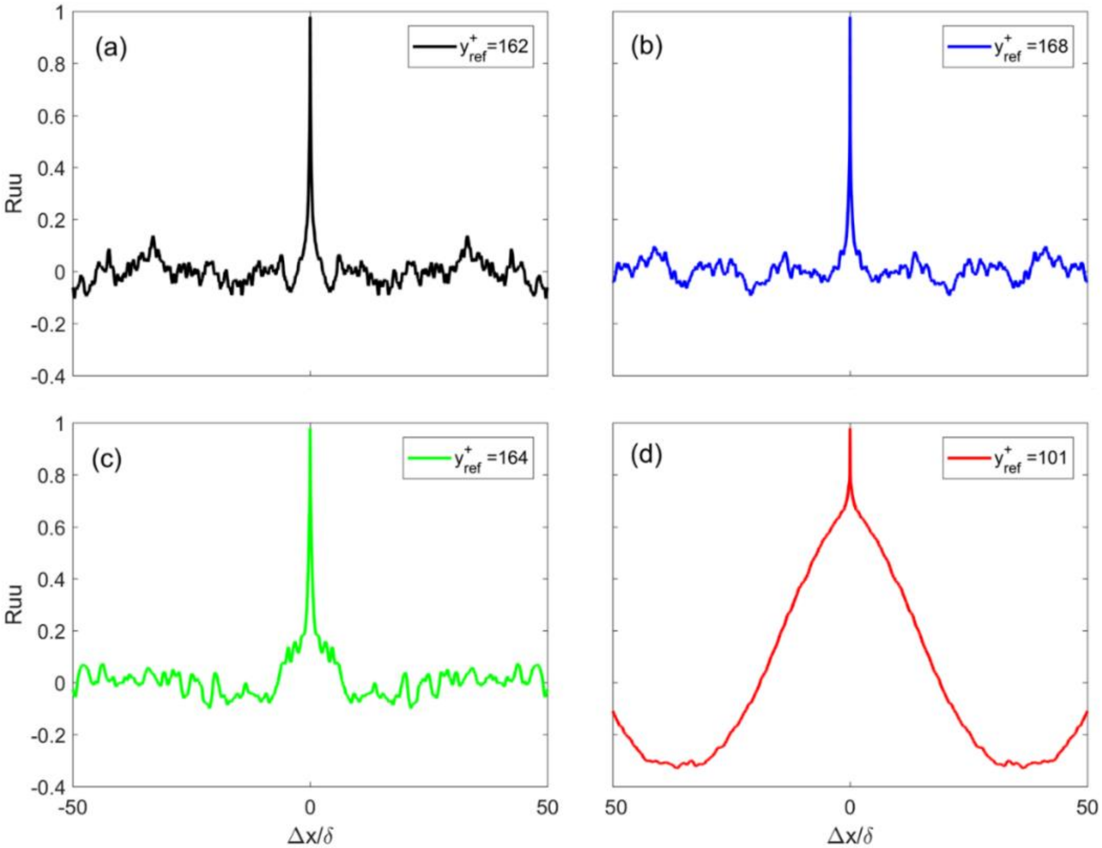

Figure 6-4. Two-point correlations of the streamwise velocity fluctuations with $\Delta y^+ = 0$ and $101 \leq y^+_{ref} \leq 168$ with (a) DR = 0%, (b) DR = 20%, (c) DR = 46%, and (d) DR = 62%.

As noted in the discussion for Figure 6-3, previous findings (Gampert & Yong., 1990; Meinhart & Adrian, 1995; Warholic et al., 2001; Kim et al., 2008) documented that the polymer additives make the flow more parallel with the streamwise direction with increasing DR. Consequently, the dominate flow structure inclination angle within the log-layer is plotted versus drag reduction in Figure 6-5. This shows that the maximum inclination angle of the dominant structure within the log-layer (~45°) occurs with DR = 0% (water), and the minimum inclination angle (~10°) occurs with DR = 62%. Linear regression analysis shows that the slope and intercept were statistically significant ($p < 0.05$) with the slope and intercept being −0.563 ± 0.085 deg/% and 46.9° ± 3.2°, respectively, with 95% confidence. Extrapolation of this linear-fit to a zero inclination angle results in a maximum drag reduction of 77%. This suggests that the existence and the ensuing spatio-temporal evolution of vortices represent a major chunk of events in near-wall turbulence that are responsible for energy exchange between the mean and turbulent flows and therefore a significant rise in skin friction drag as compared to laminar flows, which lacks both in the former process and the latter effect. Such vortical interactions have been found to be an integral part of the autonomous cycle of near-wall turbulence (Ebrahimian et al., 2019). The flattened orientation of the near-wall structures means significant bias of the flow scales in the streamwise direction with increasing DR. One immediate inference from the observed anisotropy is that these structures tend to rise less through the TBL. This would suggest that the velocity induction effects, responsible for lifting these structures through the TBL, have been curtailed as they are weakened by the presence of the polymers (Dubief et al., 2004). This is consistent with the DNS findings of Kim et al. (2007), which suggests that polymers provide torques opposing the motions of the vortices, and thereby, reducing their ability to influence events associated with their strength. Dubief et al. (2004) proposed a mechanistic explanation that stability of the momentum streaks was enhanced at the expense of weakened vortex structures; polymers stretch as they wrap around the vortices, extracting energy and re-injecting it into the near-wall ($y^+ > 5$) momentum streaks. The wrapping action is consistent with polymers providing torques, opposing vorticity intensification. If this were to be true, the structure inclination angles would decrease, as observed in Figure 6-5. This makes their contributions to the flow statistics more in the streamwise direction rather than the wall-normal direction (i.e. reduces their inclination angle), thereby reducing the momentum transfer between the outer and inner regions of the TBL.

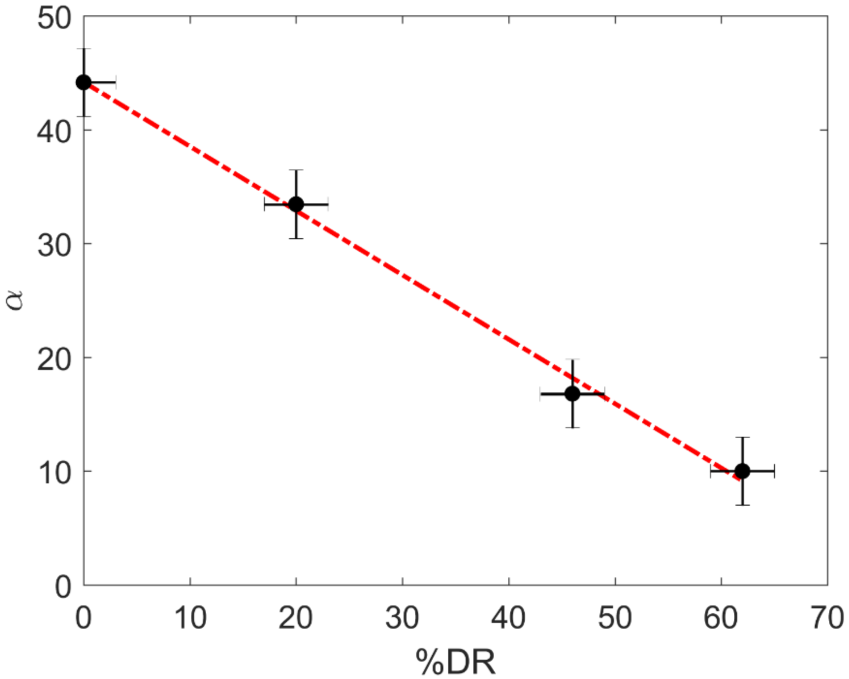

Figure 6-5. Dominant structure inclination angles within the log-layer plotted versus DR level. Data from polymer oceans at a concentration of 100 ppm with molecular weight varied and $Re_\theta = 2000$. Dashed line is the linear best-fit curve to the data.

6.3.2 Vector field visualization

For visualization, the PIV data were extended beyond the experimental field of view to allow for study of the scales of interest. Following the work of Zaman and Hussain (1981) and Saxton-Fox and McKeon (2017), a fixed convection velocity was used to ‘convect’ the PIV snapshots data. In the case of an isolated coherent structure in a turbulent flow, convecting the full shear flow with a single convection velocity equal to the centerline velocity of the structure maintained the closest approximation to the later shape of the structure (Zaman & Hussain, 1981). Figure 6-6a shows the vector field of one snapshot. Extended visualization of the instantaneous streamwise velocity is shown in Figure 6-6b. These figures focus on a dominant structure, observable as large inclined features in the streamwise velocity field of Figure 6-6. The centerline velocity of this structure, $0.8U_e$, was used as the visualisation convection velocity. The same approach was used to plot the vector field of polymeric turbulent boundary layer for DR = 53%.

The higher inclination of structures can be observed from the extended vector-field in Figure 6-7. The structures are dampened and elongated in the streamwise direction compared to the Newtonian case. In the Newtonian case, the size of a structure in the streamwise direction is shown to be on the order of the boundary layer thickness (δ). However, in the polymeric case (Figure 6-7), the size of structures is more than 4δ. The elongated drag reduced structures agree with the results from two-point correlation in the last subsection.

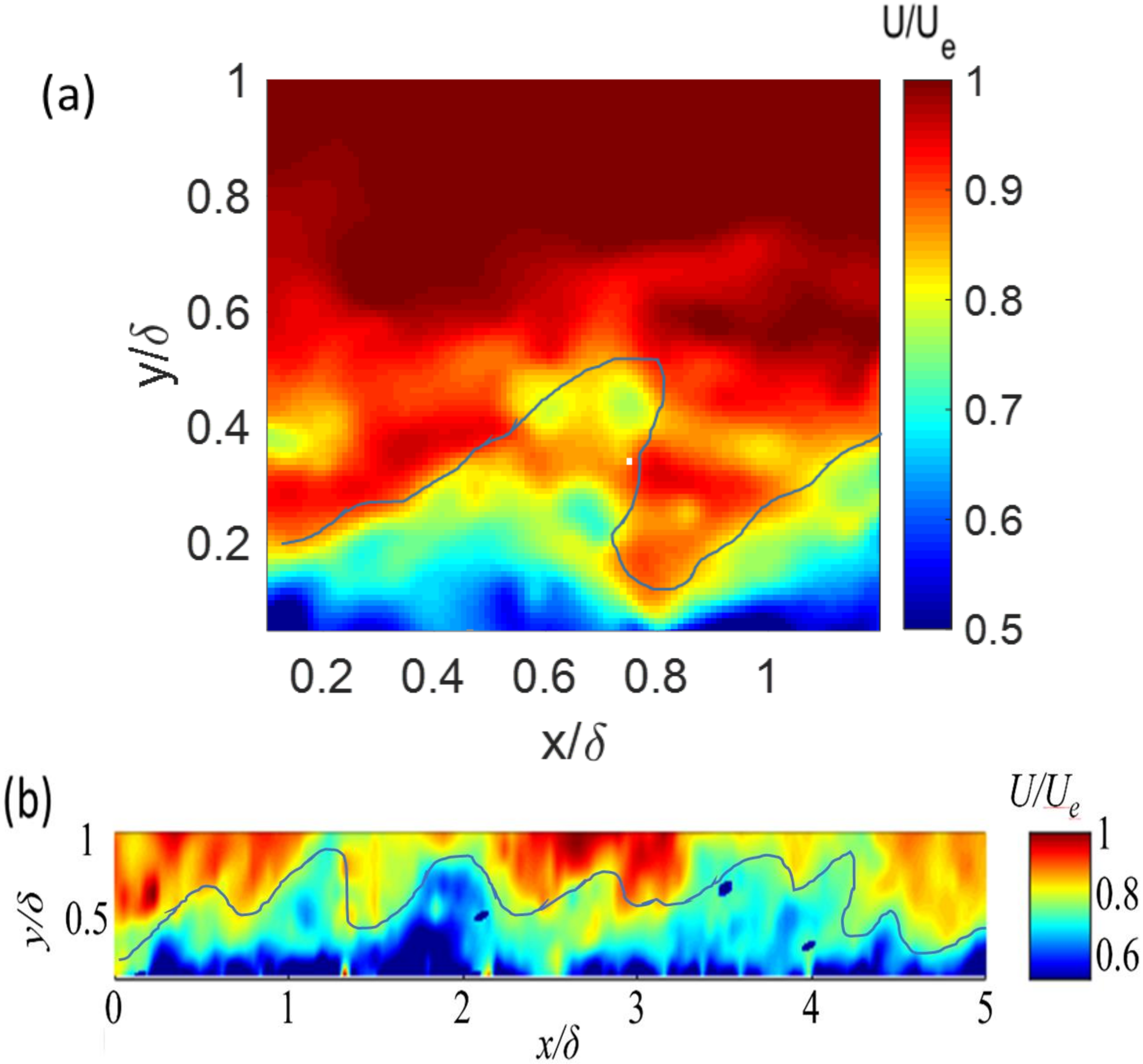

Figure 6-6 Visualization of the instantaneous streamwise velocity shown from PIV data in the *x*-*y* plane. Contour plot of the velocity field from the camera FOV is shown in (a). An extended velocity field using convection velocity is shown in (b).

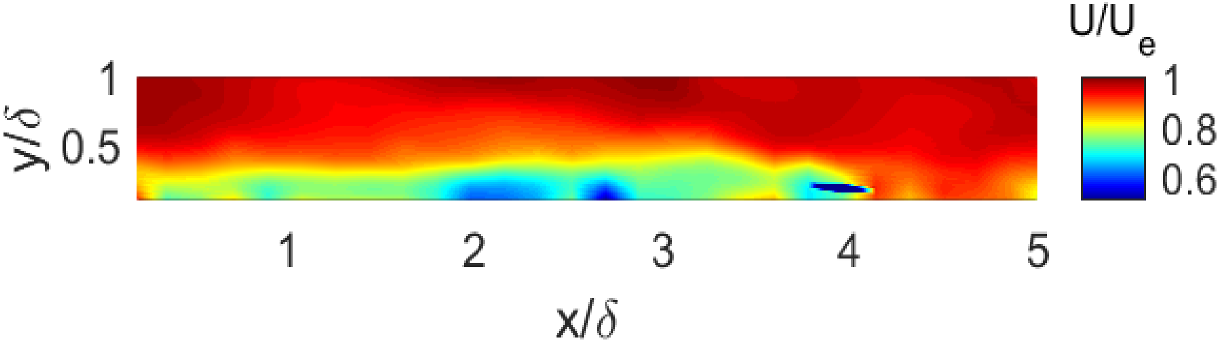

Figure 6-7 Contour plot of an extended velocity field using the structure convection velocity for a polymeric case with DR = 53%.

6.3.3 Power spectrum

For the classical turbulent energy cascade in the Newtonian turbulent flow, larger scale structures transfer the turbulent kinetic energy into smaller scale structures until the smallest scale (dissipative scale), exhaust as heat loss due to viscosity. Spectral analysis is used to provide information about how the energy of the signal is distributed with respect to frequency (here the velocity fluctuating in the turbulent boundary layer with respect to time), and by using a fast fourier transform (FFT), the data transformed to the frequency domain. To explore how the flow is influenced by drag-reducing polymer additives and how polymers contact with flow structures, the frequency spectra for polymeric (LDR and HDR) cases are compared with the Newtonian case. To investigate the multiscale interaction between flow structures and polymers, streamwise power spectrum density function of Newtonian and polymeric cases is shown in Figure 6-8. In this figure, the window period is T= 0.8 seconds for each case with sample rate $f_s = 3$ KHz. The sample duration was divided into segments of 5 signals and the FFT was applied for the average of each segment for noise reduction purpose. In Figure 6-8a, large scale structures shift to higher frequency with increasing drag reduction. A rise in spectra for each condition around 20-40 Hz is observed and it should be noted that the results below about 10 Hz are not of value as they are processing artifact.In Figure 6-8a, the peak in the low-frequency is decreasing with increasing drag reduction, which is consistent with the fact that the drag and consequently the Reynolds stresses are lower. In Figure 6-8b, the data is scaled using outer variables. As it is shown in this figure, the data is collaps until $f/\delta U_e = 1$, which is corresponding to the frequency of a structure the size of δ.

In general, the addition of polymer is to decrease the contribution of high frequency fluctuations to the turbulence. It suggest that at large and intermediate scales, polymers absorb turbulent kinetic energy from flow structures to store it as the elastic energy and dissipate it by elasticity (Barnard & Sellin, 1969; Van Doorn et al., 1999). Also, from the figure is shown that the energy cascade is altered with the presence of polymers, i.e. part of the energy income does not follow the classical Kolmogorov cascade towards viscous dissipation which is indicative of increasing the anisotropy of turbulence with increasing drag reduction.

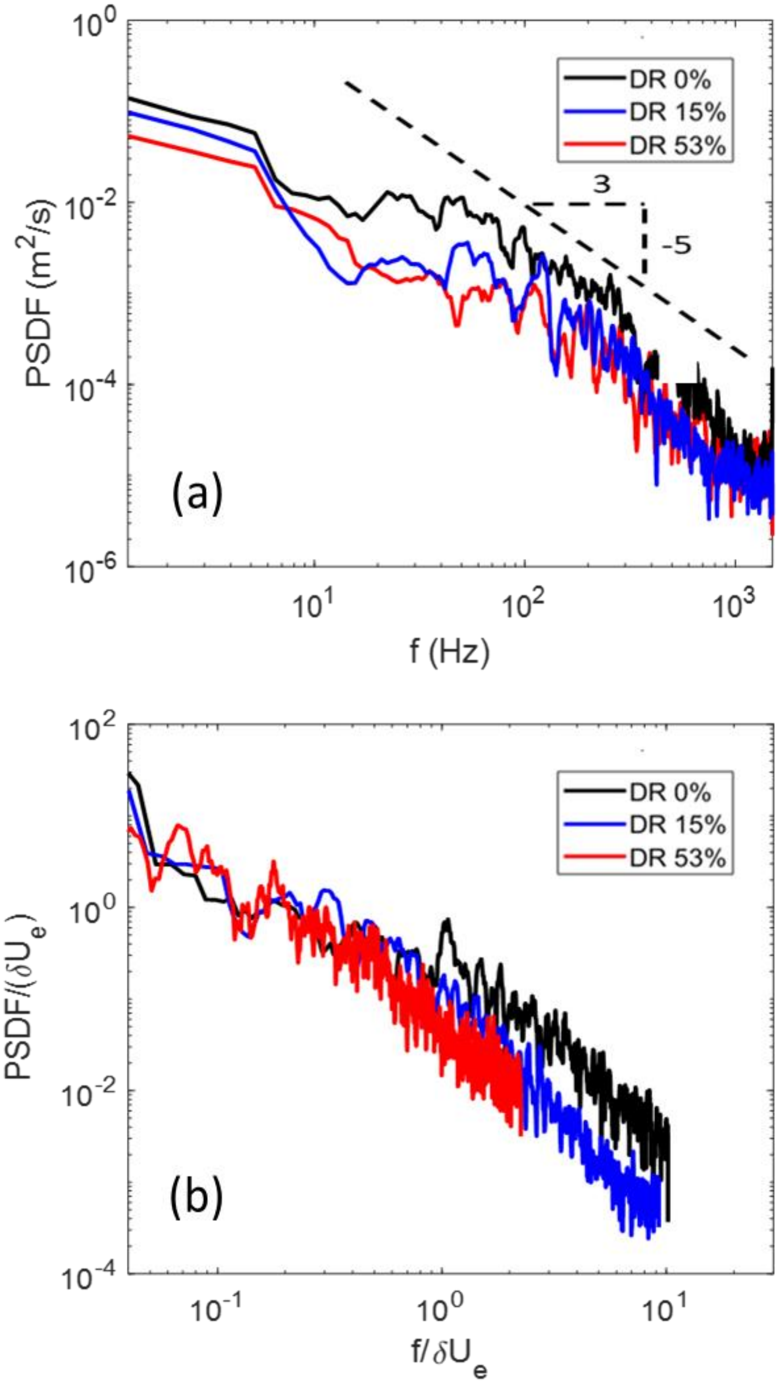

Figure 6-8 (a) Power spectra density function (PSDF) of streamwise fluctuating velocity in frequency domain at $y/\delta = 0.3$ for Newtonian, LDR and HDR turbulent boundary layer and (b) scaled power spectra of streamwise fluctuating velocity with outer variables at $y/\delta = 0.3$ for Newtonian, LDR and HDR turbulent boundary layers.

6.3.4 Proper orthogonal decomposition of dominant modes

6.3.4.1 Newtonian dominant POD modes

Proper orthogonal decomposition (POD) proposed by Lumley (1967) to objectively identify coherent structures in a turbulent flow has contributed significantly to the understanding of a smooth-wall turbulent boundary layer (TBL). POD extracts a complete, orthogonal set of spatial eigenfunctions (i.e. modes) from the measured second-order correlation function. These POD eigenmodes provide an optimal basis for expansion of the flow in the sense that energy convergence is more rapid than any other linear representation. The combination of the most energetic POD modes is associated with the large-scale, energy-containing structure of the flow.

In the current work, the contributions of the POD modes to the total turbulent kinetic energy is investigated. In Table 6-1 present first 10 modes TKE capturing 56% of total kinetic energy for the data set at $Re_\theta = 2000$. The first mode accounts for more than 1/5 of the total energy while the first two modes together account for almost 1/3 of the total energy. The energy contribution from any of the other modes is significantly smaller. The cumulative energy of the 1000 modes which represent 99% of total energy is shown in Figure 6-9. Similar energy contributions of POD modes were also observed in other studies (Liu et al., 2001; Wu & Christensen, 2010). Should be noted that this section focuses on the turbulence structures contributing strongly to the dominant modes in the log-layer and beyond.

Table 6-1 Fractional energy contributions of the first 10 POD modes for Newtonian flow (water) at $Re_\theta = 2000$.

Mode (n)	1	2	3	4	5	6	7	8	9	10
Energy (%)	24.56	8.39	5.71	4.31	3.10	2.78	2.00	1.77	1.66	1.45

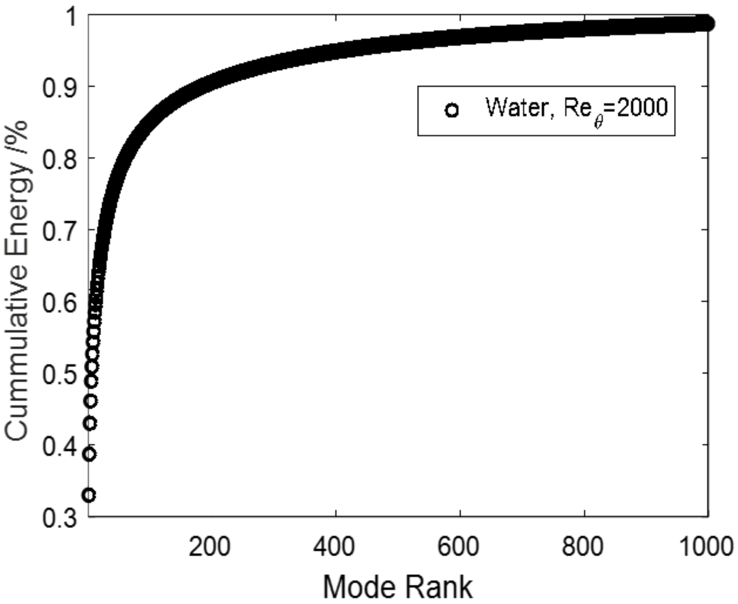

Figure 6-9 Cummulative energy of the first 1000 POD modes capturing 99% of the total energy for Newtonian flow (water).

POD modes of the flow streamwise and wall-normal velocity fluctuations are presented in Figure 6-10 and Figure 6-11. The first mode is the mean, so here modes 2 to 9 are presented, which characterize the most important coherent structures. from these modes, one can observe that modes 2 to 4 show the elongated structures that have streamwise length scales of several boundary layer thicknesses while modes 5 to 9 are more likely to represent the coherent vortices. Also, smaller sizes of the vortices can be observed at higher modes.

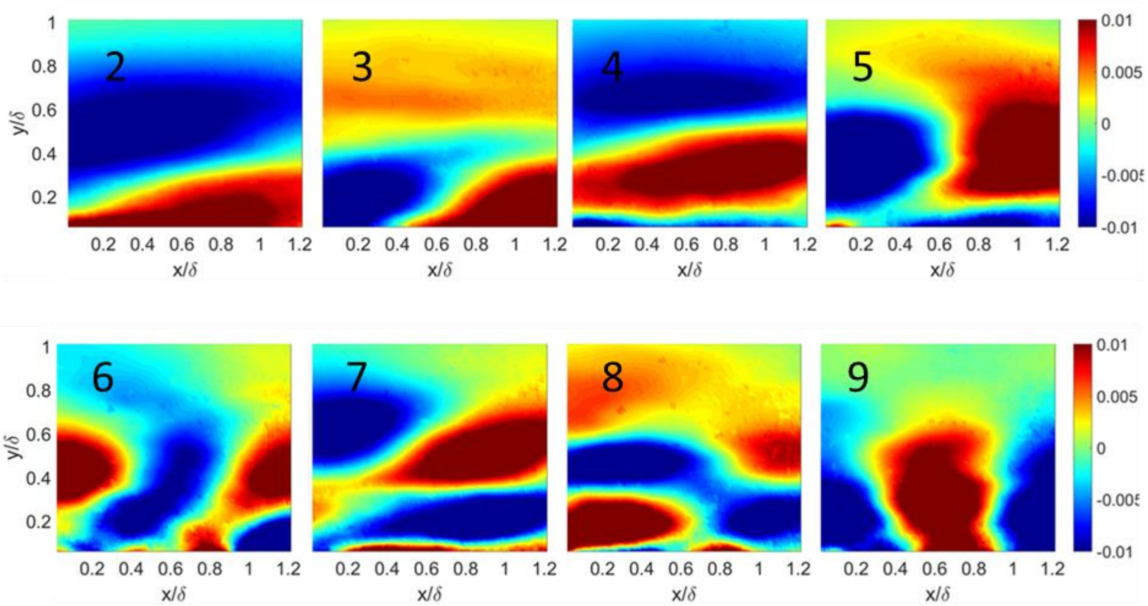

Figure 6-10 POD modes (mode 2-mode 9) of streamwise velocity component for the Newtonian (water) flow.

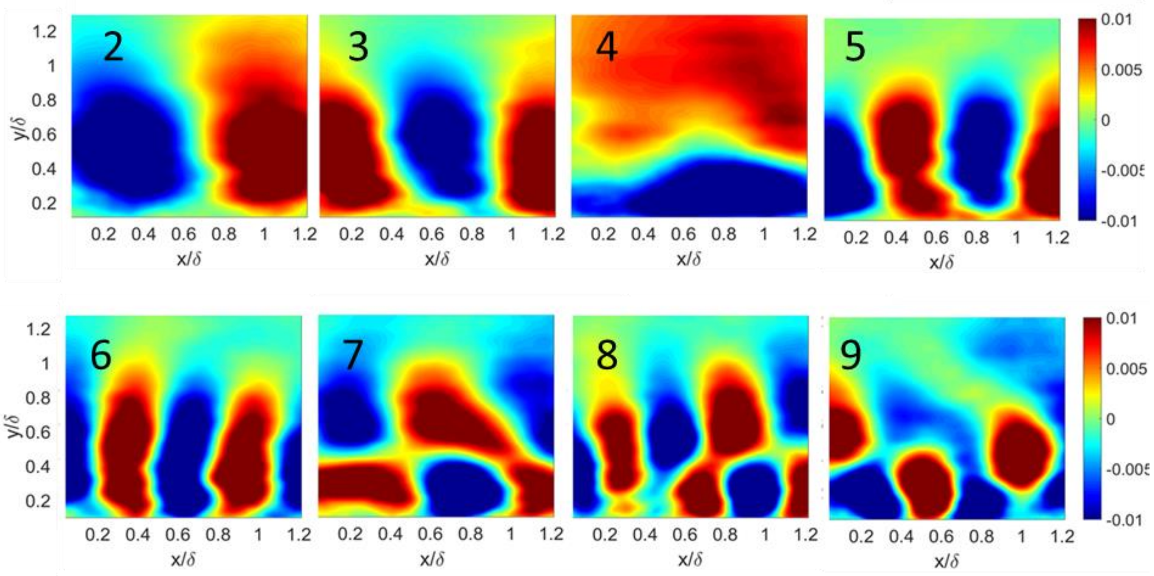

Figure 6-11 POD modes (mode 2-mode 9) of wall-normal velocity component for the Newtonian (water) flow.

Higher modes have a less coherent shape, which can be attributed to the fact that the vortices are smaller in size than the boundary layer thickness, and they tend to become more randomly and homogeneously distributed in the boundary layer. Dominant POD modes at different rank clearly reveal a cascade of scales in the TBL.

6.3.4.2 First POD coefficient

The scatter plot of the first POD coefficients, $a1$ normalized by its rms value, σ_{a1}, are presented in Figure 6-12. An instantaneous fluctuating velocity field with a positive or negative $a1$ value means that its reconstruction using the first POD mode will represent a Q2 or Q4 event, respectively. The Q2 events, in which $\acute{u}^{+} < 0$ and $\acute{v}^{+} > 0$, correspond to the upward movement of the slower fluids near the wall to larger y^{+}, which causes a local reduction in the streamwise velocity and is often termed “ejections.” Meanwhile, the opposite Q4 events are called “sweeps” (Wallace, 2016). If $a1$ is large for a particular field, the fluctuating velocities tend to illustrate an extended region of strong Q2 (or Q4) event. As shown in Figure 6-12, *a1* values are almost within 1.5 times σ_{a1} and there are only a small amount of velocity fields with the coefficient larger than twice σ_{a1}. However, since the contribution to the first eigenvalue comes from $a1$, those few velocity fields with large $a1$ values carry a significant weight in defining the first POD mode. Therefore, the instantaneous turbulence structures in these velocity fields are the dominant structures associated with the first mode. It can also be observed that the distribution of $a1$ is approximately symmetric between positive and negative values, indicating roughly equal contributions from Q2 and Q4 events to the first POD mode.

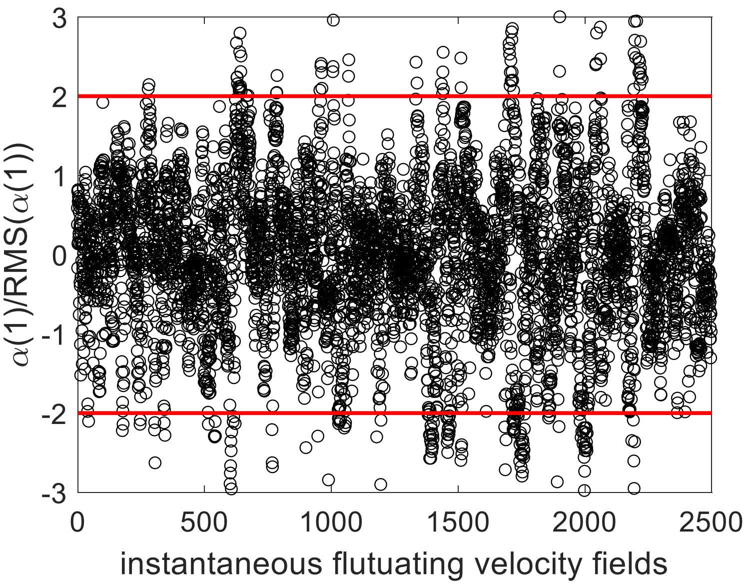

Figure 6-12 Scatter plots of the normalized (by rms value of $a1$, σ_{a1}) first POD coefficient, $a1$, for all the instantaneous velocity field snapshots.

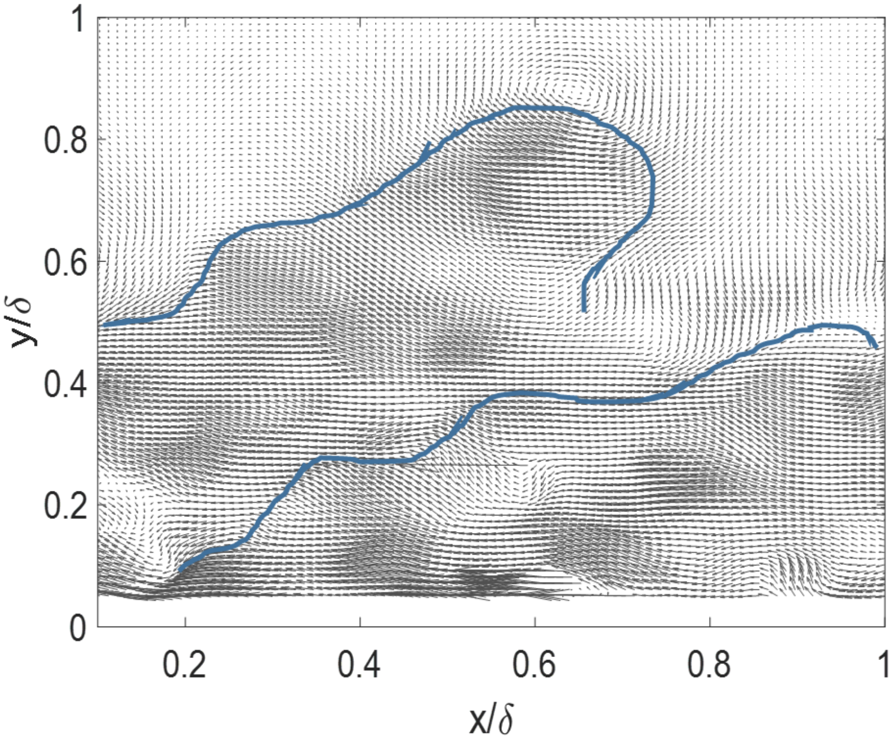

Figure 6-13 An instantaneous fluctuating velocity vector field with a large positive POD coefficient of $a1 = 2.0\ \sigma_{a1}$ for the first POD mode. The dominant structures are outlined for visual clarity.

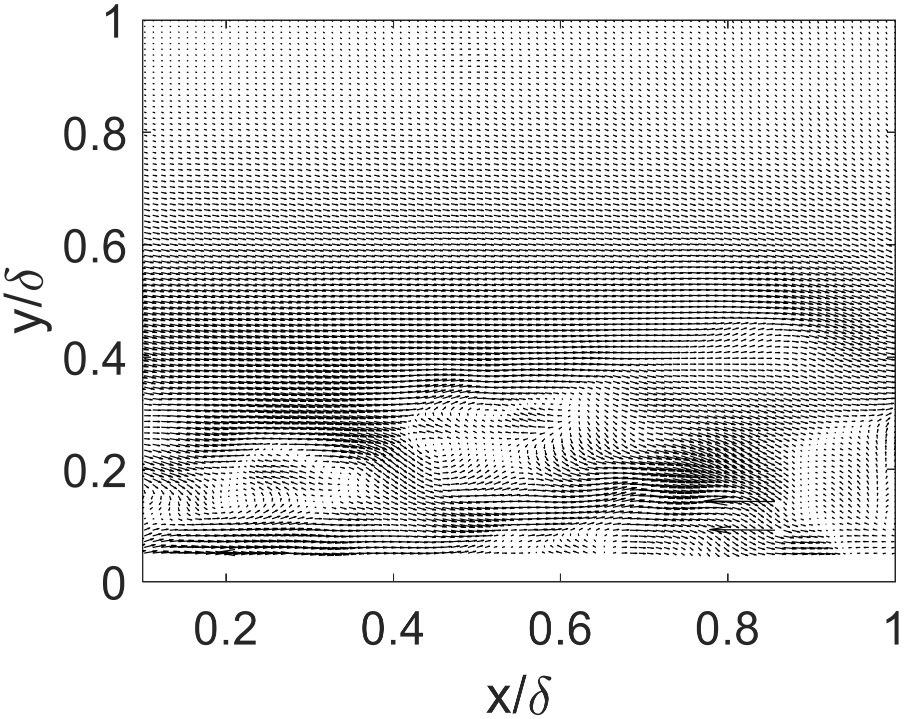

Figure 6-14 An instantaneous fluctuating velocity vector field with a large negative POD coefficient of $a1 = -2.0\sigma_{a1}$ for the initial POD mode.

An instantaneous fluctuating velocity field with a relatively large positive coefficient for the first POD mode ($a > \sigma_a$) is shown in Figure 6-13. The main feature of this field is a large-scale Q2 event that extends beyond 0.6δ in the wall-normal direction. Hairpin packets-structures in the figure can be observed considering Q2 vectors are associated with the hairpin vortex packet. These structures are similar to the hierarchy of hairpin vortex packets described in Adrian (2007). Based on the focus of this work in the log-region and beyond, the hairpin vortex packet thus appears to be the best structure to describe those instantaneous flows that contribute significantly to the first POD mode with positive and negative coefficients. In Figure 6-14, which is from a larger negative coefficient, there should be vortices within this Q4 event, but these vortices do not appear to be organized like in Figure 6-13. The distribution of *a1* shown in Figure 6-12 is approximately symmetric, even for large values, and it may indicate that these large-scale Q2 and Q4 events are PIV samplings of the same large-scale turbulence structure that is best described by the hairpin vortex packet (Adrian, 2007). However, further studies using three-dimensional velocity measurement techniques such as tomographic PIV (Elsinga et al., 2006) are needed to investigate the three-dimensional topology of these large-scale structures.

6.3.4.3 Polymeric dominant POD modes

It is known that the characteristics of isotropic turbulence can be changed due to the addition of polymers, especially for the inhibition of small-scale vortex structures (Gampert & Yong, 1990). POD was used to observe the different scales of structures in drag reduced flow as well as its comparison with their Newtonian counterpart. The first observation was to compare the energy content of modes of DR = 53% and Wi = 4.5. The individual energy content of polymeric and Newtonian POD modes are listed in Table 6-2. The average amount of turbulent kinetic energy in the projection of modes is equal to the corresponding eigenvalue (λ) and the result from Newtonian data showed that the first eigenmode contains (on average) 33% of the fluctuating kinetic energy for the Newtonian fluid flow, whereas it contains 52% for polymer solution flow. It should be noted that in this section the compared Newtonian and polymeric flow are at $Re_\theta = 2900$. Coherent structures are seen as the sum of several eigenmodes that possess the dominant energy of the flow. From Figure 6-15, it is shown that more eigenmodes are required for the Newtonian condition to converge to 90% of the total energy relative to the PDR case. From the convergence of accumulative energy for both Newtonian and polymeric flows, the POD energy spectrum reveals that the flow field can be described by fewer spatially distributed structures and the faster convergence of the polymeric flow indicates that the scales of the structures are not as broad as in Newtonian flow.

Table 6-2 Percentage of energy contributions for the first 10 POD modes for DR = 0% (Newtonian) and DR = 53%. ($Re_\theta = 2900$)

Mode (n)	1	2	3	4	5	6	7	8	9	10
DR = 0%	33.47	10.01	5.85	4.06	3.34	2.82	2.45	2.13	1.82	1.51
DR = 53%	52.69	6.92	4.65	3.55	2.17	1.94	1.61	1.38	1.20	1.01

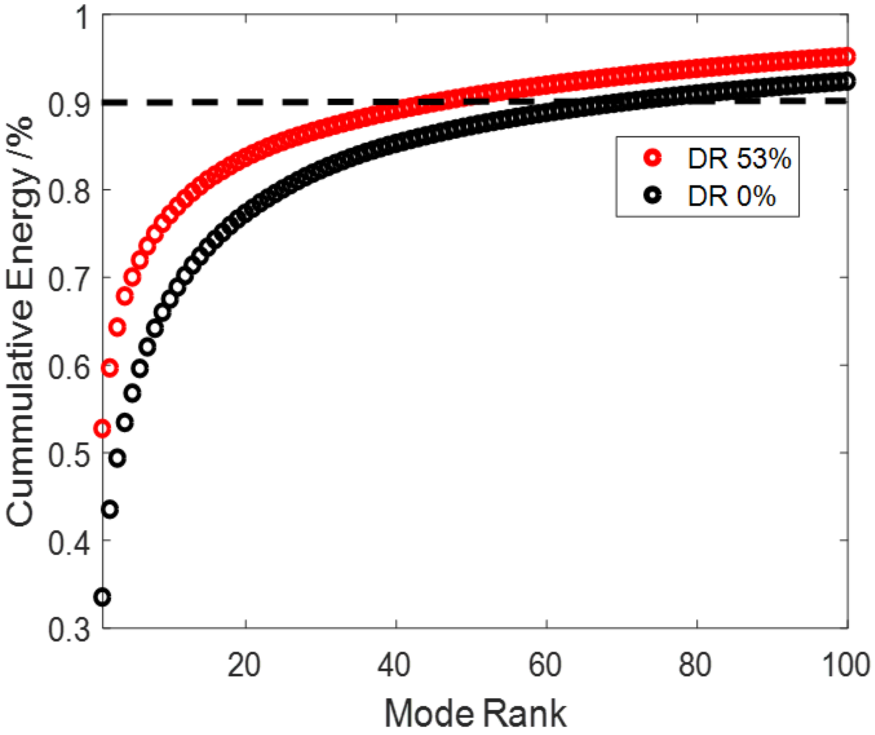

Figure 6-15 Cumulative energy of POD modes for Newtonian (water) TBL and 53% polymer drag reduced TBL at $Re_\theta = 2900$.

The scatter plot of the first POD coefficient, $a1$, normalized by its rms value, σ_{a1}, for polymeric TBL are presented in Figure 6-16. Values of $a1$ are predominately within 1.5 times σ_{a1} like the Newtonian case, and a small amount of velocity fields have coefficients larger than twice σ_{a1}. It is expected that with higher POD coefficient $a1$, the instantaneous velocity field is more similar to the vector field of the first POD mode and bigger flow structures tend to exist in that field (Liu et al., 2001). A velocity field with a large $a1$ value is plotted in Figure 6-17, from this figure the contributions from Q2 events to the first POD mode are damped, showing that the Q2 event extended much less from the wall than the Newtonian TBL. The random structures or incoherent vorticies are not appeared, which supports the observed weak fluctuations in the two-point correlation of streamwise fluctuating velocities.

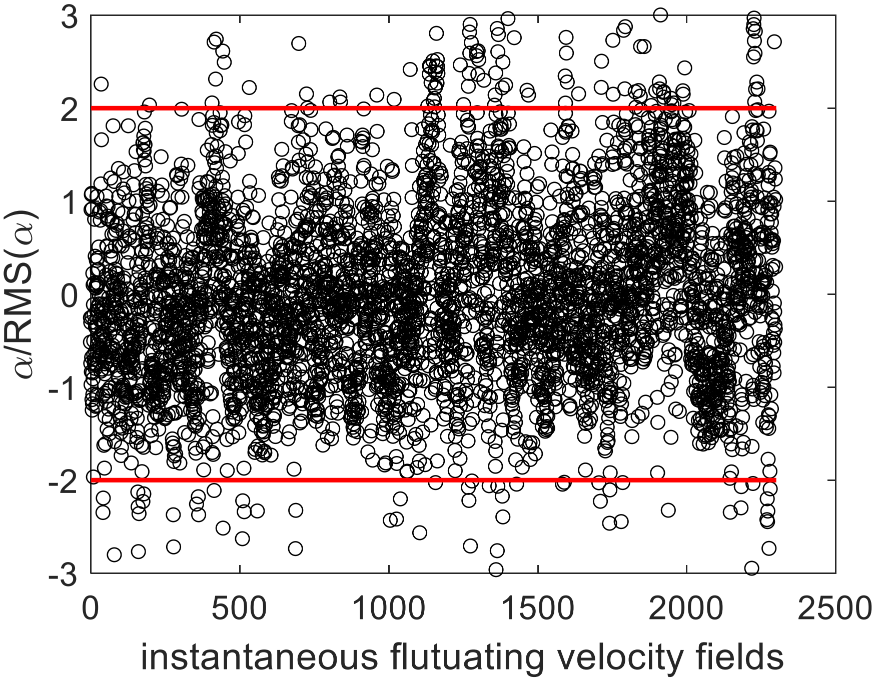

Figure 6-16 Scatter plot of the first POD coefficient, $a1$, normalized by its rms value, σ_{a1}, for all the instantaneous velocity fields of the 53% drag reduced TBL.

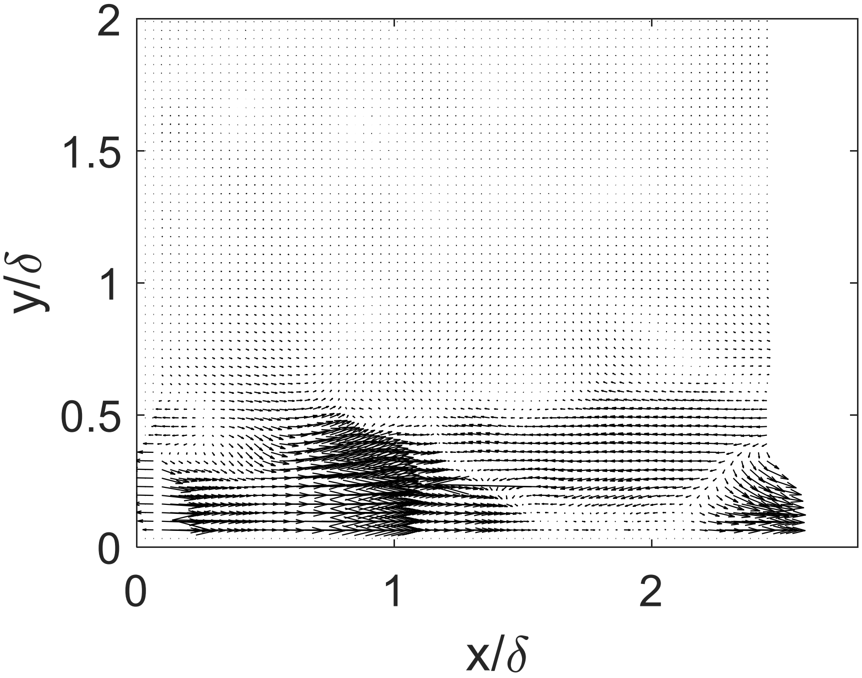

Figure 6-17 An instantaneous fluctuating velocity field with a large positive POD coefficient of $a1$ = 2.0 σ_{a1} for the first POD mode in a polymeric TBL (DR = 53%).

To particularly understand the effect of polymers on the size of the turbulence structures, a qualitative estimate of the character of the structures, in terms of their streamwise coherence, was obtained from the two-point correlations in section 6.3.1. An analysis of two-point correlations has revealed a modification of the average elongation of the near-wall streamwise vortices as well as spacing or frequency of the dominant coherent structure and their inclination angles. Figure 6-18 shows the first five POD modes for 53% drag reduction and the Newtonian case. The size of the structures are drastically changed with drag reduction. The structures are more correlated while their size decreases at higher modes in both streammwise and wall normal direction. In this figure, the y-origin is at the wall, and the x-origin is 0.455 m from the test section inlet and the center of camera FOV is at the 0.5 m (downstream of the test section inlet). The configuration of the structures and their coherency for Newtonian TBL compared to polymeric TBL appears to be consistent with the trend observed from the two-point correlations of the streamwise velocity component in the section 6.3.

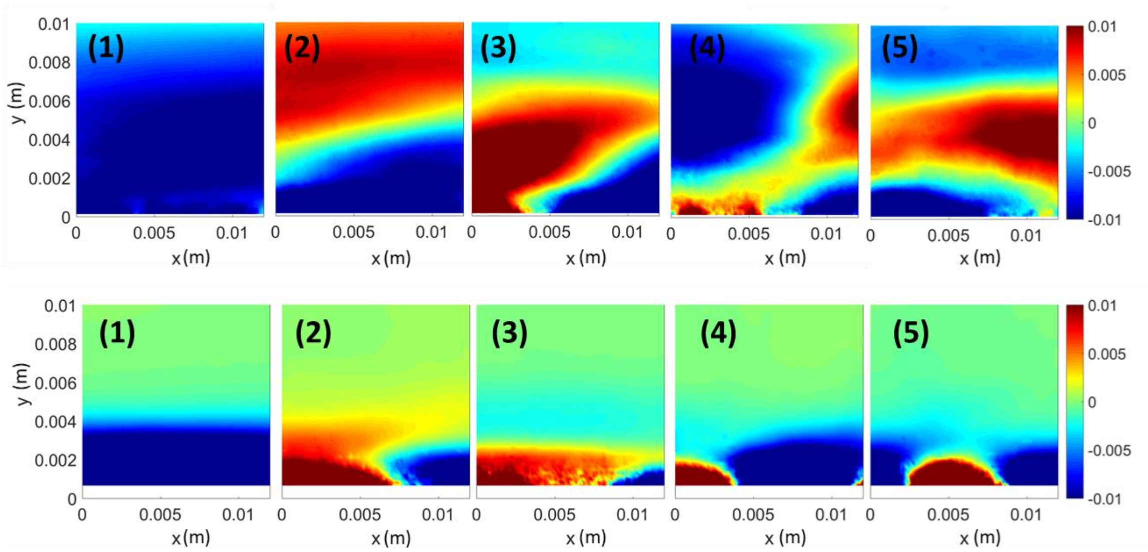

Figure 6-18 First five POD modes of the streamwise velocity for (top) Newtonian TBL and (bottom) polymeric TBL with DR= 53%.

6.4 Summary and conclusions

Modification of the dominant coherent structures in a polymer drag reduced TBL was investigated by examining the flow statistics near the wall. Coherent motions/structures are 3D regions of flow exhibiting significant correlations between flow parameters (Sillero, 2014). This definition was incorporated to infer orientations of dominant structures within the TBL log-region by computing two-point normalized correlations of streamwise velocity fluctuations. Results for both the Newtonian and polymeric flows were obtained, compared, and analyzed. Mean velocity profiles identified the extent of the log-regions and compared well with DNS data at a similar Reynolds number (Marusic, 2001). The Newtonian results were consistent with available literature with the dominate structure inclination angle being 46.9° ± 4° (average from $Re_\theta = 800$, 2000, and 2900) though it should be noted that the mean structure angle within the log-region is between 15°

and 18° (Robinson, 1991; Deshpande et al., 2019). Log-regions farther from the wall showed progressively improved correlations. This indicates that the uniformity of momentum zones has expanded in *x*-*y* plane (possibly associated with large scale motions (LSMs)).

Trends in the two-point correlations for the polymeric flows deviated from the Newtonian flows, particularly at HDR (>40%). Much like that of the fluctuating velocity fields in the buffer and viscous sublayer, flow scale anisotropy was progressively enhanced in the upper bounds of the log and outer-wake regions; structures have significantly enhanced streamwise scales. This anisotropy is particularly prominent for regimes of DR close to MDR. Correlations show the reduced range of variations for a given streamwise scale as DR increases, suggesting the stabilizing effect of polymer additives on the flow statistics. For the same extent of the TBL, the correlations in polymeric flows were found to be marginally higher than the Newtonian flows for LDR. These trends were then found to deviate appreciably for HDR. The details of how the momentum zones (likely due to LSM) tend to develop as Weissenberg numbers increase, is inferred from the normalized correlation plots at three DR levels (20%, 46%, and 62%).

Normalized correlations purely along the streamwise direction ($\Delta y = 0$) corroborate the stretching of streamwise scales of the flow with increasing DR, but also show suppression in the fluctuations of the correlations. This indicates that polymer additives are actively engaged in suppressing the fluctuating content of the flow structures at higher frequencies. This serves as an experimental verification of the flow simulations featuring weakened vortices, due to opposing torques by polymer body forces (Kim et al., 2007). Such vortices would then contribute less to the auto-generation process of hairpins (White et al., 2012). Such attenuation of the fluctuating turbulent motions would suggest that the offspring shedding process of the primary hairpins (flow structures) has been curbed and that this restriction becomes stronger in HDR flows. However, modes of action on these structures by polymers are rather selective, based on the intrinsic polymer and flow properties. Swirling-strength based time scales of the vortices suggest that the shorter the time scale, the stronger the structure. This would increase the local Weissenberg numbers and therefore the probability of being attenuated by the stretching action of the polymers. Since the most intense of these vortices are in the buffer-layer, in the LDR the effect of polymers would remain primarily within the buffer-layer. This would explain the mild transition in observation between DR = 0% and DR = 20% for all correlations in the log-region. Mild transitions, however, do not suggest that there is "virtually" no effect of polymers additives on the log-layer. It is clear that the "domino effect" of the weakened hairpin/quasi-streamwise vortices or QSVs is to make the log-region structures more inclined towards the flow direction. But as higher Weissenberg numbers are achieved, the polymers start effecting the less energetic vortex regions (heads and necks) found in the log-layer, directly. This could be attributed to the polymer relaxation times being significantly larger than the largest time scales associated with the vortex structures of the TBL. The reduced offspring shedding activity of the vortices can potentially explain the enhanced correlations observed over long streamwise scales (Figure 6-3 and Figure 6-4). The fact that the structures are far apart, is compensated by their flattened orientation. Being targeted by the polymers based on their strengths, vortex structures with similar strength could weaken simultaneously, which aids in preserving the coherence of the dominant eddy structure.

Figure 6-5 shows the dependence of the structure inclination angle on DR. Decreasing averaged inclination angle of coherent structures with the streamwise direction show that anisotropy of the flow scales increases in proportion to the reduction in skin friction and so reducing momentum transfer between the outer and inner regions of the TBL. Weakened vortices near the wall (log-region) due to the presence of polymers bias their contribution to the flow statistics towards the streamwise direction. Moreover, the flattened inclinations, shown in Figure 6-5, suggest a linear relationship between such structure angles (in the TBL log-region) with increasing DR, $\alpha = -0.563DR + 46.9$. Extrapolation of this fit predicts a maximum drag reduction of 77%. This further suggests that polymers are involved in severely mitigating the spatiotemporal evolution of vortical structure in the TBL near wall region, a process which significantly contributes to the production of skin-friction drag.

The effect of DR studied using snapshot POD analysis at $Re_\tau = 800$. One dimensional POD analysis in the *y*-direction has revealed that the convergence of POD modes obtained for the drag-reduced flow is slower compared to Newtonian. The first three modes capture around 60% and 53% for polymeric and Newtonian flows, respectively. This trend and the faster convergence of the POD modes obtained for the drag reduced flow can be attributed to a decrease in the range of length scales due to drag reduction. POD allows the distribution of energy to be evaluated as a function of scale. It decomposes the flow field into modes having various scales. POD captures the patterns (structures) that contribute to the TKE. A faster convergence signifies a smaller number of structures that contain the total TKE compared to Newtonian flow. It should be noted that the dominant modes are still a large-scale structure as they capture a significantly large fraction of the fluctuating energy.

CHAPTER VII

7 CONCLUSION

For a comprehensive overview of the current study, a brief review of how the investigation was conducted and the major conclusions drawn from the results obtained, are presented below in the order of chapters listed.

7.1 Aim 1

Drag reduction performance of mechanically degraded dilute PEO solutions

This part of the current study used a turbulent pipe flow experiment to do a comparative analysis between mechanically degraded polymer (PEO) solutions and non-degraded polymer (PEO) solutions at the same mean molecular weight. Degraded samples were produced via passing samples through a pipe that included a precisely positioned V-shaped needle valve. The degradation resulted in an increase in the shear rates at the onset of drag reduction, for which Vanapalli et al. (2005) provided an empirical relationship between the onset of drag reduction shear rate and the mean molecular weight for PEO. The samples were degraded such that they produced mean molecular weights (onset of drag reduction shear rates) that matched within ±10% of available non-degraded molecular weights.

Characterization of the non-degraded samples produced bulk flow behavior that is consistent with previous PEO studies in the literature, such as that done in Virk (1975), Gampert and Wagner (1985), Vanapalli et al. (2005), and Elbing et al. (2009). Comparative analysis of the mechanically degraded samples (samples with different initial, but known, mean molecular weights degraded to a known final mean molecular weight) with the non-degraded samples at the mean molecular weight of the final state of the degraded samples produced the following primary conclusions:

- While some conditions showed good agreement in the slope increment between degraded and non-degraded samples, there were conditions that had significant deviations in the slope increment (drag reduction performance) between the degraded and non-degraded samples, with the non-degraded samples consistently larger (more efficient).
- The deviation in slope increment scaled well with the normalized difference between the initial and final molecular weights, defined as ζ with the deviation increasing rapidly when $\zeta > 0.6$. However, it is expected that the exact value of this acceleration is specific to the degradation method, including the ratio of the residence time to the relaxation time.
- The deviations in drag reduction performance for degraded and non-degraded samples at a given molecular weight were attributed to deviations in the molecular weight distribution, which was supported by other observations in Paterson and Abernathy (1970) and Hunston and Zakin (1980). Furthermore, this behavior is likely enhanced prior to achieving steady-state molecular weight, when there would be an excess of longer polymer chains as discussed in Gampert and Wagner (1985). It indeed was the case for the majority of conditions presented.

- The amount of deviation can be reduced if steady-state conditions can be achieved. However, if the elongational rate far exceeds the critical elongational rate then the final molecular weight distribution could be broader, as in Sim et al. (2007), which could still impact the drag reduction performance.

7.2 Aim 2

Modification of the TBL mean statistics with drag-reducing polymer solution

Time-averaged and time-resolved PIV data was used to obtain the trends in the mean and fluctuating flow statistics in polymer ocean over a flat plate. Using a polymer ocean avoided uncertainty of the polymer parameters since they are sensitive to the local concentration of polymer. As a baseline, the tests were first conducted for Newtonian flow (DR = 0%) and then compared with the established literature for Newtonian TBL flow (De Graaff & Eaton, 2000). Experiments were then conducted with polymer oceans to observe differences in the mean streamwise velocity statistics and fluctuating flow statistics corresponding to streamwise fluctuating velocity statistics, $\acute{u}$, wall-normal velocity fluctuations, $\acute{v}$ and $\acute{u}^2$. The statistics were captured for the near-wall region that encompassed the upper bounds of the buffer layer and the log-layer structure. This part of the study produced the following primary observations and conclusions when compared to Newtonian flows.

- While the von-Karman constant for the log-law remains relatively unchanged for the LDR regime with only the slope-intercept increasing in proportion to drag reduction, the von-Karman constant progressively decreased with increasing Wi numbers (0.22, 2.5, 4.3). This served to identify and enforce the difference between the modern-day view and the classical view of PDR.
- The changing mean statistics of the log-law is indicative of the varying dynamics of the extended buffer layer, which serves to provide boundary conditions for the log-layer.

Also, it was observed that with a progressive increase in the *Wi* number, the log-law continued to be of a diminishing spatial extent.

- For the fluctuating flow statistics, the observations made with regard to streamwise fluctuations show that they increased. This observation was made when scaled with friction velocity.
- While an increase in streamwise fluctuations were observed, wall-normal fluctuations were severely suppressed. This indicated that the flow was becoming increasingly parallel with increasing DR. This can be related to the cross gradient momentum diffusivity that is reduced.

7.3 Aim 3

Modification of TBL coherent structures with drag-reducing polymer solutions.

The study presented in this chapter used two-point correlations of the streamwise velocity and proper orthogonal decomposition to investigate the impact of polymer flow additives on the near-wall turbulent flow structure. Flow measurements were taken over a flat plate using time-resolved PIV. Following the approach of Marusic (2001), the correlations have been modified to capture flow statistics in the streamwise direction as well as wall-normal direction. The reference values for these locations were chosen to depict the correlation of events in the logarithmic region for Newtonian flow and their modifications with drag-reducing polymer additives. Analysis of the flows has produced the following primary conclusions.

- Much like the anisotropy of the fluctuating flow field in the viscous sublayer and the buffer layer, flow scales in the logarithmic region tend to experience significant bias in the flow direction. This is apparent from the large scale streamwise distances that the correlations take to get to zero.

- The polymer additives are observed to preferentially target the high-frequency structure content of the flow. The drastic suppression of the fluctuations in streamwise correlations for the DR = 62% case (depicting events near the MDR asymptote) points towards this wiping out of high-frequency content, given that polymers primarily target the strength aspect of the vortical structure by providing counter torques to their rotation, corroborating the findings of Dubief et al. (2004) and Kim et al. (2007).
- The transition in flow statistics for the logarithmic region of TBL from 0% DR case (Newtonian flow) to DR < 40% is rather mild, at least until the separation region between the LDR and HDR regimes of PDR. The reason for such preferred action is due to the polymer relaxation times and the associated swirling strength of the vortices, which is inversely proportional to the time scales associated with such structures. Since the most intense vortices reside beneath the log-layer, as discussed in Robinson et al. (1989), the effect of transition is more likely to be observed first in the buffer layer and then in the log-layer as the level of DR increases.
- The definition used involving the peak of correlations and its variance in spatial location to infer the structure angle (α) shows that the structure angle reduces linearly with DR $(\alpha = -0.563DR + 46.9)$. This gradual decrease in structure angle conforms to the dynamics of coherent structures under the influence of polymer additives; namely to provide anti-torque for reducing the swirling strength of the vortices (Kim et al. 2007).
- Reduced structure angle is thought to be the reason behind the increasingly anisotropic nature of the flow scale observed, which shows a bias towards the streamwise direction in proportion to the value of DR.
- The convergence of POD modes obtained for drag reduced flow is slower compared to Newtonian. The first three modes capture around 60% and 50%, respectively, for polymeric and Newtonian flows. This trend and the faster convergence of the POD modes

obtained for the drag reduced flow can be attributed to a decrease in the range of length scales due to drag reduction.

- A faster convergence of cumulative energy of the modes signifies a smaller number of structures that contain the total TKE compared to Newtonian flow.

7.4 Future work

The study of modified wall-bounded turbulence, by interpreting its structural makeup based on the relevant statistical detail, provides the depth of knowledge on the near-wall turbulent flows. Although experimental investigations have been instrumental in laying out the way to be adopted in this regard, one of the major issues is related to accurately capture the dynamics of a polymer chain, such as the Weissenberg numbers. This requires an in-depth investigation into the buffer layer and a statistically backed estimate of the coherent structures therein. Numerical data is available on such investigations. However, experimental data to establish sound physical models relating to the near-wall and outer region events are needed. This has potential implications for shaping the research on numerical models and computational schemes. Moreover, this study shows that 2D PIV has been primarily used for the analysis. With the emerging technique of 3D PIV, it would prove to be insightful to see what are the impact of the polymer additives on the spanwise fluctuations. Moreover, the use of spanwise velocity and its correlation with the other flow fluctuations in orthogonal directions can also reveal the hairpin vortex structure evolution in the spanwise direction. Also, POD analysis of 3D vector fields will introduce a clearer picture of structural dynamics.

POD modes are orthogonal and usually ordered in terms of decreasing energy content. Therefore, they represent the structures carrying the most energy and also the most `coherence'. In this respect. However, the most coherent structures in space need not also be the most coherent in time. Dynamic modes decomposition would be a useful method that explores more structural dynamics of the TBL for polymeric flow and is useful when one needs to identify coherent structures associated with a specific time-scale.

Finally, it should also be noted that since fluctuating pressure-velocity correlation term is responsible for the re-adjusting of the turbulent kinetic energy in the flow. Clearly, this mechanism happens to be modulated as shown in the chapter in mean statistics. Therefore, inferring the modification of flow structure using wall pressure-velocity correlations might prove to be successful particularly when seeking to understand the influence of polymer additives on large scale structures.

REFERENCES

Acharya, M., Bornstein, J., & Escudier, M. P. (1986). Turbulent boundary layers on rough surfaces. *Experiments in Fluids, 4*(1), 33-47.

Achia, B. U., & Thompson, D. W. (1977). Structure of the turbulent boundary in drag-reducing pipe flow. *Journal of Fluid Mechanics, 81*(3), 439-464

Adrian, R. J. (2007). Hairpin vortex organization in wall turbulence. *Physics of Fluids, 19*(4), 041301.

Adrian, R. J., Meinhart, C. D., & Tomkins, C. D. (2000). Vortex organization in the outer region of the turbulent boundary layer. *Journal of Fluid Mechanics, 422*, 1-54.

Bailey, Jr. F. E., & Callard, R. W. (1959). Some properties of poly(ethylene oxide) in aqueous solution. *Journal of Applied Polymer Science, 1*(1), 56-62.

Bailey, Jr. F. E., & Koleske, J. V. (1976). *Polyethylene Oxide*. Academic Press, New York.

Bandyopadhyay, P. R., & Ahmed, A. (1993). Turbulent boundary layers subjected to multiple curvatures and pressure gradients. *Journal of Fluid Mechanics, 246*, 503-527.

Berman, N. S. (1977). Drag reduction of the highest molecular weight fractions of polyethylene oxide. *Physics of Fluids. 20*(5) 715-718.

Barnard, B. J. S., & Sellin, R. H. J. (1969). Grid turbulence in dilute polymer solutions. *Nature, 222*(5199), 1160-1162.

Blackwelder, R. F., & Eckelmann, H. (1979). Streamwise vortices associated with the bursting phenomenon. *Journal of Fluid Mechanics, 94*(3), 577-594.

Bortel, E., & Lamot, R. (1977). Examination of the breakdown of high molecular weight polyethylene oxides in the solid state. *Macromolecular Chemistry and Physics, 178*(9), 2617-2628.

Bourassa, C., & Thomas, F. O. (2009). An experimental investigation of a highly accelerated turbulent boundary layer. *Journal of Fluid Mechanics, 634*, 359-404.

Brown, G. L., & Thomas, A. S. (1977). Large structure in a turbulent boundary layer. *Physics of Fluids. 20*(10), S243-S252.

Burger, E. D., Munk, W. R., & Wahl, H. A. (1982). Flow increase in the Trans Alaska Pipeline through use of a polymeric drag-reducing additive. *Journal of Petroleum Technology, 34*(02), 377-386.

Ching, C., Djenidi, L. & Antonia, R. (1995). Low-Reynolds-effects in a turbulent boundary layer. *Experiments in Fluids 19*, 61–68.

Choi, H. J., & Jhon, M. S. (1996). Polymer-induced turbulent drag reduction. *Industrial & Engineering Chemistry Research*, *35*(9), 2993-2998.

Clark, J. A., & Markland, E. (1971). Flow visualization in turbulent boundary layers. *Journal of the Hydraulics Division*, *97*(10), 1653-1664.

Coles, D. E. (1962). The turbulent boundary layer in a compressible fluid. Appendix A: A manual of experimental practice for low-speed flow. Rand. Rep., pp. 35–74.

Coles, D. E. (1968). Computation of turbulent boundary layers. AFOSR-IFP-Stanford Conference. Stanford University Press.

Culter, J. D., Zakin, J. L., & Patterson, G. K. (1975). Mechanical degradation of dilute solutions of high polymers in capillary tube flow. *Journal of Applied Polymer Science, 19*(12), 3235-3240.

Daniel, L. (2014). *Design and installation of a high Reynolds number recirculating water tunnel*. Thesis MS, Oklahoma State University, Stillwater, OK.

Daniel, L., Mohagheghian, S., Dunlap, D., Ruhlmann, E., & Elbing, B. R. (2015, November). Design of a recirculating water tunnel for the study of high-Reynolds number turbulent boundary layers. In *ASME 2015 International Mechanical Engineering Congress and Exposition*. American Society of Mechanical Engineers Digital Collection.

De Gennes, P. G., & Gennes, P. G. (1979). *Scaling Concepts in Polymer Physics*. Cornell University Press.

De Graaff, D. B., & Eaton, J. K. (2000). Reynolds-number scaling of the flat-plate turbulent boundary layer. *Journal of Fluid Mechanics, 422*, 319-346.

Deng, B. Q., Huang, W. X., & Xu, C. X. (2016). Origin of effectiveness degradation in active drag reduction control of turbulent channel flow at Reτ= 1000. *Journal of Turbulence, 17*(8), 758-786.

Deshpande, R., Montyrlin, J., & Marusic, I. (2019). Streamwise inclination angle of large wall-attached structures in turbulent boundary layers. *Journal of Fluid Mechanics, 877*, R4.

Donohue, G. L., Tiederman, W. G., & Reischman, M. M. (1972). Flow visualization of the near-wall region in a drag-reducing channel flow. *Journal of Fluid Mechanics*, *56*(3), 559-575.

Draad, A. A., Kuiken, G. D. C., & Nieuwstadt, F. T. M. (1998). Laminar–turbulent transition in pipe flow for Newtonian and non-Newtonian fluids. *Journal of Fluid Mechanics, 377*, 267-312.

Dubief, Y., White, C. M., Terrapon, V. E., Shaqfeh, E. S., Moin, P., & Lele, S. K. (2004). On the coherent drag-reducing and turbulence-enhancing behavior of polymers in wall flows. *Journal of Fluid Mechanics, 514*, 271-280.

Ebrahimian, M., Sanders, R. S., & Ghaemi, S. (2019). Near-wall motion of inertial particles in a drag-reduced non-Newtonian turbulent flow. *Experiments in Fluids*, *60*(7), 117.

Eckelmann, H. (1974). The structure of the viscous sublayer and the adjacent wall region in a turbulent channel flow. *Journal of Fluid Mechanics, 65*(3), 439-459.

Elbing, B. R. (2018) Flow-assisted polymer degradation in turbulent boundary layers. In: Proceedings of the AIChE Annual Meeting, Area 01C Interfacial Phenomena, Pittsburgh, PA (Oct 28 – Nov 2).

Elbing, B. R., Winkel, E. S., Solomon, M. J., & Ceccio, S. L. (2009). Degradation of homogeneous polymer solutions in high shear turbulent pipe flow. *Experiments in Fluids, 47*(6), 1033-1044.

Elbing, B. R., Solomon, M. J., Perlin, M., Dowling, D. R., & Ceccio, S. L. (2011). Flow-induced degradation of drag-reducing polymer solutions within a high-Reynolds-number turbulent boundary layer. *Journal of Fluid Mechanics, 670*, 337-364.

Elbing, B. R., Perlin, M., Dowling, D. R., & Ceccio, S. L. (2013). Modification of the mean near-wall velocity profile of a high-Reynolds number turbulent boundary layer with the injection of drag-reducing polymer solutions. *Physics of Fluids, 25*(8), 085103.

Elbing, B. R., Daniel, L., Farsiani, Y., & Petrin, C. E. (2018). Design and validation of a recirculating, high-Reynolds number water tunnel. *Journal of Fluids Engineering, 140*(8), 081102.

Elsinga, G. E., Scarano, F., Wieneke, B., & van Oudheusden, B. W. (2006). Tomographic particle image velocimetry. *Experiments in Fluids, 41*(6), 933-947.

Elsnab, J. R., Monty, J. P., White, C. M., Koochesfahani, M. M., & Klewicki, J. C. (2019). High-fidelity measurements in channel flow with polymer wall injection. *Journal of Fluid Mechanics, 859*, 851-886.

Escudier, M. P., Rosa, S., & Poole, R. J. (2009). Asymmetry in transitional pipe flow of drag-reducing polymer solutions. *Journal of Non-Newtonian Fluid Mechanics*, *161*(1-3), 19-29.

Etter, R. J., Cutbirth, J. M., Ceccio, S. L., Dowling, D. R., & Perlin, M. (2005). High Reynolds number experimentation in the US Navy's William B Morgan large cavitation channel. *Measurement Science and Technology, 16*(9), 1701.

Farsiani, Y & Elbing, B. R. (2016). Characterization of a custom-designed, high-Reynolds number water tunnel. *2016 ASME Fluids Engineering Division Summer Meeting*, FEDSM2016-7866, Track 10 Forum on Fluid Measurements and Instrumentation, Washington, DC (July 10-14).

Farsiani, Y., Saeed, Z., & Elbing, B. R. (2020a). Drag reduction performance of mechanically degraded dilute polyethylene oxide solutions. Accepted to *Journal of Fluids Engineering* on March 22, 2020 [Preprint: axXiv: 1907.07614].

Farsiani, Y., Saeed, Z., Jayaraman, B., & Elbing, B. R. (2020b). Modification of turbulent boundary layer coherent structures with drag-reducing polymer solution. *Physics of Fluids, 32*(1), 015107 (doi.org/10.1063/1.5127293).

Fontaine A., Petrie, H., & Brungart, T. (1992). Velocity profile statistics in a turbulent boundary layer with slot-injected polymer. *Journal of Fluid Mechanics, 238*, 435-466.

Fore, R. S., Szwalek, J., & Sirviente, A. (2005). The effects of polymer solution preparation and injection on drag reduction. *Journal of Fluids Engineering, 127*(3), 536-549.

Gad-el-Hak, M., Bandyopadhyay, P. R., Yang, W. J., Fann, S., & Kim, J. H. (1994). Reynolds Number Effects in Wall-Bounded Turbulent Flows. *Applied Mechanics Reviews, 47*(8), 307-365.

Gampert, B., & Wagner, P., (1985). The Influence of molecular weight and molecular weight distribution on drag reduction and mechanical degradation in turbulent flows of highly dilute polymer solutions. In *The Influence of Polymer Additives on Velocity and Temperature Fields, International Union of Theoretical and Applied Mechanics* (Deutsche Rheologische Gasellschaft) (ed. Gampert B), Springer, Berlin, Heidelberg, 71-85.

Gampert, B., & Yong, C. K. (1990). The influence of polymer additives on the coherent structure of turbulent channel flow. In *Structure of Turbulence and Drag Reduction* (pp. 223-232). Springer, Berlin, Heidelberg.

George, W. K. (2007). Is there a universal log law for turbulent wall-bounded flows? Philosophical Transactions of the Royal Society A: *Mathematical, Physical and Engineering Sciences*, *365*(1852), 789-806.

Graham, M. D. (2004). Drag reduction in turbulent flow of polymer solutions. *Rheology Reviews, 2*(2), 143-170.

Grandbois, M., Beyer, M., Rief, M., Clausen-Schaumann, H., & Gaub, H. E. (1999). How strong is a covalent bond? *Science, 283*(5408), 1727-1730.

Grass, A. J. (1971). Structural features of turbulent flow over smooth and rough boundaries. *Journal of Fluid Mechanics*, *50*(2), 233-255.

Gupta, V., Sureshkumar, R., & Khomami, B. (2004). Polymer chain dynamics in Newtonian and viscoelastic turbulent channel flows. *Physics of Fluids, 16*(5), 1546-1566.

Gyr, A. (Ed.). (2012). Structure of Turbulence and Drag Reduction. *IUTAM Symposium Zurich, Switzerland, July 25–28, 1989*. Springer Science & Business Media.

Gyr, A., & Bewersdorff, H. W. (1990). Change of structures close to the wall of a turbulent flow in drag reducing fluids. In *Structure of Turbulence and Drag Reduction* (pp. 215-222). Springer, Berlin, Heidelberg.

Habibpour, M., & Clark, P. E. (2017). Drag reduction behavior of hydrolyzed polyacrylamide/xanthan gum mixed polymer solutions. *Petroleum Science*, *14*(2), 412-423.

Head, M. R., & Bandyopadhyay, P. (1981). New aspects of turbulent boundary-layer structure. *Journal of Fluid Mechanics, 107*, 297-338.

Hinch, E. J. (1977). Mechanical models of dilute polymer solutions in strong flows. *The Physics of Fluids*, *20*(10), S22-S30.

Hinze J. O. (1975). *Turbulence*. McGraw-Hill, Inc., 2nd ed.

Horn, A., & Merrill, E. (1984). Midpoint scission of macromolecules in dilute solution in turbulent flow. *Nature, 312*(5990), 140.

Hou, Y. X., Somandepalli, V. S. R., & Mungal, M. G. (2008). Streamwise development of turbulent boundary-layer drag reduction with polymer injection. *Journal of Fluid Mechanics, 597*, 31-66.

Hunston, D. L., & Zakin, JL. (1980). Flow-assisted degradation in dilute polystyrene solutions. *Polymer Engineering and Science, 20*(7), 517-523.

Hutchins, N., & Marusic, I. (2007). Evidence of very long meandering streamwise structures in the logarithmic region of turbulent boundary layers. *Journal of Fluid Mechanics*, *579*,1–28.

Jayaraman, B., & Brasseur, J. G. (2019). The surprising transition in atmospheric boundary layer turbulence structure from neutral to moderately convective stability states and mechanisms underlying large-scale rolls. *arXiv preprint arXiv:1807.03336*.

Jiménez, J., & Pinelli, A. (1999). The autonomous cycle of near-wall turbulence. *Journal of Fluid Mechanics*, *389*, 335-359.

Kalashnikov, V. N. (1994). Shear-rate dependent viscosity of dilute polymer solutions. *Journal of Rheology*, *38*(5), 1385-1403.

Kalashnikov, V. N., & Askarov, A. N. (1989). Relaxation time of elastic stresses in liquids with small additions of soluble polymers of high molecular weights. *Journal of Engineering Physics*, *57*(2), 874-878.

Kim, K. C., & Adrian, R. J. (1999). Very large-scale motion in the outer layer. *Physics of Fluids*, *11*(2), 417-422.

Kim, K., & Sirviente, A. I. (2005). Turbulence structure of polymer turbulent channel flow with and without macromolecular polymer structures. *Experiments in Fluids*, *38*(6), 739-749.

Kim, K., & Sureshkumar, R. (2013). Spatiotemporal evolution of hairpin eddies, Reynolds stress, and polymer torque in polymer drag-reduced turbulent channel flows. *Physical Review E*, *87*(6), 063002.

Kim, H., Kline, S. J., & Reynolds, W. C. (1971). The production of turbulence near a smooth wall in a turbulent boundary layer. *Journal of Fluid Mechanics*, *50*(1), 133-160.

Kim, C. A., Kim, J. T., Lee, K., Choi, H. J., & Jhon, M. S. (2000). Mechanical degradation of dilute polymer solutions under turbulent flow. *Polymer*, *41*(21), 7611-7615.

Kim, K., Li, C. F., Sureshkumar, R., Balachandar, S., & Adrian, R. J. (2007). Effects of polymer stresses on eddy structures in drag-reduced turbulent channel flow. *Journal of Fluid Mechanics*, *584*, 281-299.

Kim, K., Adrian, R. J., Balachandar, S., & Sureshkumar, R. (2008). Dynamics of hairpin vortices and polymer-induced turbulent drag reduction. *Physical Review Letters*, *100*(13), 134504.

Kline, S. J., Reynolds, W. C., Schraub, F. A., & Runstadler, P. W. (1967). The structure of turbulent boundary layers. *Journal of Fluid Mechanics*, *30*(4), 741-773.

Koskie, J. E., & Tiederman, W. G. (1991). Polymer drag reduction of a zero-pressure-gradient boundary layer. *Physics of Fluids A: Fluid Dynamics*, *3*(10), 2471-2473.

Kulik, V. M. (2001). Drag reduction change of polyethylene oxide solutions in pipe flow. *Experiments in Fluids*, *31*(5), 558-566.

Lander, M. (2018). *Preparation and characterization of polyethylene-oxide (PEO) solution*. MS Thesis. Oklahoma State University, Stillwater, USA.

Larson, R. G. (1999). *The Structure and Rheology of Complex Fluids*. Oxford University Press, New York.

Lauchle, G. C., & Gurney, G. B. (1984). Laminar boundary-layer transition on a heated underwater body. *Journal of Fluid Mechanics*, *144*, 79-101.

Laufer, J. (1951). Investigation of Turbulent Flow in a Two-Dimensional Channel. NACA Rep. 1053, 1951. (Supersedes NACA TN 2123.)

Layec-Raphalen, M. N., & Layec, Y. (1985). Influence of molecular parameters on laminar non-Newtonian and on turbulent flows of dilute polymer solutions. In B. Gampert (Ed.) The Influence of Polymer Additives on Velocity and Temperature Fields. *International Union of Theoretical and Applied Mechanics*, Berlin (pp. 89-100), Deutsche Rheologische.

Lighthill, M. J. (1963). Boundary layer theory. *Laminar Boundary Layers*, 46-113.

Liu, Z., Adrian, R. J., & Hanratty, T. J. (2001). Large-scale modes of turbulent channel flow: Transport and structure. *Journal of Fluid Mechanics*, *448*, 53-80.

Löfdahl, L., Stemme, G., & Johansson, B. (1992). Silicon based flow sensors used for mean velocity and turbulence measurements. *Experiments in Fluids, 12*(4-5), 270-276.

Lozano-Durán, A., Flores, O., & Jiménez, J. (2012). The three-dimensional structure of momentum transfer in turbulent channels. *Journal of Fluid Mechanics, 694*, 100-130.

Luchik, T. S., & Tiederman, W. G. (1988). Turbulent structure in low-concentration drag-reducing channel flows. *Journal of Fluid Mechanics, 190*, 241-263.

Lumley J. L. (1967). The structures of inhomogeneous turbulent flow. In A. M. Yaglom, & V. I. Tararsky (Eds.) *Proceedings of the International Colloquium on the Fine Scale Structure of the Atmosphere and its Influence on Radio Wave Propagation*, Moscow (pp.166–178), Nauka Publishing.

Marboe, R. C., Weyer, R. M., Jonson, M. L., & Thompson, D. E. (1993). Hydroacoustic research capabilities in the large water tunnel at ARL Penn State. In *Proceedings of the 1993 ASME Winter Annual Meeting* (pp. 125-135). ASME.

Marusic, I. (2001). On the role of large-scale structures in wall turbulence. *Physics of Fluids*, *13*(3), 735-743.

Marusic, I., Monty, J. P., Hultmark, M., & Smits, A. J. (2013). On the logarithmic region in wall turbulence. *Journal of Fluid Mechanics. 716*, 1-11.

Meinhart, C. D., & Adrian, R. J. (1995). On the existence of uniform momentum zones in a turbulent boundary layer. *Physics of Fluids, 7*(4), 694-696.

Metzger, M. M., Klewicki, J. C., Bradshaw, K. L., & Sadr, R. (2001). Scaling the near-wall axial turbulent stress in the zero pressure gradient boundary layer. *Physics of Fluids, 13*(6), 1819-1821.

Min, T., Yoo, J. Y. & Choi, H. (2003a). Maximum drag reduction in a turbulent channel flow by polymer additives. *Journal of Fluid Mechanics. 492*, 91–100.

Min, T., Yoo, J. Y., Choi, H., & Joseph, D. D. (2003b). Drag reduction by polymer additives in a turbulent channel flow. *Journal of Fluid Mechanics*, *486*, 213-238.

Mochizuki, S., & Nieuwstadt, F. T. M. (1996). Reynolds-number-dependence of the maximum in the streamwise velocity fluctuations in wall turbulence. *Experiments in Fluids, 21*(3), 218-226.

Mohammadtabar, M., Sanders, R. S., & Ghaemi, S. (2017). Turbulent structures of non-Newtonian solutions containing rigid polymers. *Physics of Fluids, 29*(10), 103101.

Morrison, J. F. (2007). The interaction between inner and outer regions of turbulent wall-bounded flow. *Philosophical Transactions of the Royal Society A: Mathematical, Physical and Engineering Sciences*, *365*(1852), 683-698.

Moussa, T., & Tiu, C. (1994). Factors affecting polymer degradation in turbulent pipe flow. *Chemical Engineering Science*, *49*(10), 1681-1692.

Nagib, H. M., & Chauhan, K. A. (2008). Variations of von Kármán coefficient in canonical flows. *Physics of Fluids*, 20(10), 101518.

Nagib, H., Christophorou, C., Reudi, J.-D., Monkewitz, P., Österlun, J. & Gravante, S. (2004). Can we ever rely on results from wall-bounded turbulent flows without direct measurements of wall shear stress. In *24th AIAA Aerodynamic Measurement Technology and Ground Testing Conference (USA), Portland, Oregon (p*p. 2392*)*. American Institute of Aeronautics and Astronautics (AIAA).

Odell, J. A., Keller, A., & Miles, M. J. (1983). Method for studying flow-induced polymer degradation: Verification of chain halving. *Polymer Communications, 24*(1), 7-10.

Oweis, G. F., Winkel, E. S., Cutbrith, J. M., Ceccio, S. L., Perlin, M., & Dowling, D. R. (2010). The mean velocity profile of a smooth-flat-plate turbulent boundary layer at high Reynolds number. *Journal of Fluid Mechanics, 665*, 357-381.

Panton, R. (1997). A Reynolds stress function for wall layers. Trans. *ASME Journal of Fluids Engineering, 119*, 325.

Park, J. T., Cutbirth, J. M., & Brewer, W. H. (2003, January). Hydrodynamic performance of the large cavitation channel (LCC). In *Proceedings of the ASME/JSME 2003 4th Joint Fluids Summer Engineering Conference* (USA), Honolulu, Hawaii (pp. 87-100). American Society of Mechanical Engineers Digital Collection. https://doi.org/10.1115/FEDSM2003-45599

Paschkewitz. J, Dimitropoulos. C. D., Hou. Y., Somandepalli. V., Mungal. M., Shaqfeh. E. S., & Moin. P. (2005). An experimental and numerical investigation of drag reduction in a turbulent boundary layer using a rigid rodlike polymer. *Physics in Fluids 17*, 085101.

Patel, V. C. (1965). Calibration of the Preston tube and limitations on its use in pressure gradients. *Journal of Fluid Mechanics, 23*(1), 185-208.

Paterson, R. W., & Abernathy, F. H. (1970). Turbulent flow drag reduction and degradation with dilute polymer solutions. *Journal of Fluid Mechanics, 43*(4), 689-710.

Perlin, M., Dowling, D. R., & Ceccio, S. L. (2016). Freeman scholar review: Passive and active skin-friction drag reduction in turbulent boundary layers. *Journal of Fluids Engineering, 138*(9), 091104.

Petrie, H., Deutsch, S., Brungart, T., & Fontaine, A. (2003). Polymer drag reduction with surface roughness in flat-plate turbulent boundary layer flow. *Experiments in Fluids*, 35(1), 8-23.

Petrie, H., Fontaine, A., Money, M., & Deutsch, S. (2005). Experimental study of slot-injected polymer drag reduction. In *Proceedings of the 2nd International Symposium on Seawater Drag Reduction,* Busan, Korea (May 23-26).

Prandtl, L. (1904). Über Flussigkeitsbewegung bei sehr kleiner Reibung. Verhandl. III, Internat. Math.-Kong., Heidelberg, Teubner, Leipzig, 1904, 484-491.

Ptasinski, P. K., Nieuwstadt, F. T. M., Van Den Brule, B. H. A. A., & Hulsen, M.A. (2001). Experiments in turbulent pipe flow with polymer additives at maximum drag reduction. *Flow Turbulence and Combustion*, *66*(2), 159-182.

Ptasinski, P. K., Boersma, B. J., Nieuwstadt, F. T. M., Hulsen, M. A., Van den Brule, B. H. A. A., & Hunt, J. C. R. (2003). Turbulent channel flow near maximum drag reduction: simulations, experiments and mechanisms. *Journal of Fluid Mechanics, 490*, 251-291.

Purtell, L. P., Klebanoff, P. S., & Buckley, F. T. (1981). Turbulent boundary layer at low Reynolds number. *Physics of Fluids, 24*(5), 802-811.

Reischman, M. M., & Tiederman, W. G. (1975). Laser-Doppler anemometer measurements in drag-reducing channel flows. *Journal of Fluid Mechanics, 70*(2), 369-392.

Robinson, S. K. (1991). Coherent motions in the turbulent boundary layer. *Annual Review of Fluid Mechanics*, *23*(1), 601-639.

Robinson, S. K., Kline, S. J., & Spalart, P. R. (1989). A review of quasi-coherent structures in a numerically simulated turbulent boundary layer. NASA STI/Recon Technical Report N, 90.

Roshko, A. (1961). Experiments on the flow past a circular cylinder at very high Reynolds number. *Journal of Fluid Mechanics*, *10*(3), 345-356.

Saeed, Z. (2019). *Characterization of degraded polyethylene oxide solutions and its impact on structure of turbulence*. MS Thesis. Oklahoma State University, Stillwater, USA.

Saxton-Fox, T., & McKeon, B. J. (2017). Coherent structures, uniform momentum zones and the streamwise energy spectrum in wall-bounded turbulent flows. *Journal of Fluid Mechanics, 826*.

Schlichting, H. (1960). *Boundary Layer Theory* (4th ed., Vol. 960). New York: McGraw-Hill.

Schmid, A. (1984). Experimental investigation of the influence of drag reducing polymers on a turbulent channel flow. In *Third International Conference on Drag Reduction, Proceedings edited by RH Sellin, RT Moses, University of Bristol, paper B* (Vol. 12).

Schultz, M. P. (2002). The relationship between frictional resistance and roughness for surfaces smoothed by sanding. *Journal of Fluids Engineering*, *124*(2), 492-499.

Sellin, R. H. J. (1982). The effect of drag-reducing additives on fluid flows and their industrial applications part 2: Present applications and future proposals. *Journal of Hydraulic Research, 20*(1), 29–69.

Shaban, S., Azad, M., Trivedi, J., & Ghaemi, S. (2018). Investigation of near-wall turbulence in relation to polymer rheology. *Physics of Fluids, 30*(12), 125111.

Shin, H. (1965). *Reduction of drag in turbulence by dilute polymer solutions*. PhD. thesis, Massachusetts Institute of Technology, Cambridge Department of Chemical Engineering.

Sibilla, S., & Baron, A. (2002). Polymer stress statistics in the near-wall turbulent flow of a drag-reducing solution. *Physics of Fluids*, *14*(3), 1123-1136.

Sillero, J. (2014). *High Reynolds number turbulent boundary layers*. PhD. thesis, Universidad Politenica de Madrid, Madrid, Spain.

Sillero, J. A., Jiménez, J., & Moser, R. D. (2014). Two-point statistics for turbulent boundary layers and channels at Reynolds numbers up to $\delta^+ \approx 2000$. *Physics of Fluids, 26*(10), 105109.

Sim, H., Khomami, B., & Sureshkumar, R. (2007). Flow–induced chain scission in dilute polymer solutions: Algorithm development and results for scission dynamics in elongational flow. *Journal of Rheology, 51*(6), 1223-1251.

Simpson, R. L. (1967). The turbulent boundary layer on a porous plate: An experimental study of the fluid dynamics with injection and suction. Department of Mechanical Engineering, Stanford University, Stanford, CA.

Simpson, R. L. (1970). Characteristics of turbulent boundary layers at low Reynolds numbers with and without transpiration. *Journal of Fluid Mechanics, 42*(4), 769-802.

Smith, C. R. (1984). A synthesized model of the near-wall behavior in turbulent boundary layers. In J. L. Zakin, & G. Patterson (Eds.) *Proceedings of the 8th Symposium of Turbulence*. University of Missouri–Rolla, Rolla.

Somandepalli, V. S. R., Hou, Y. X., & Mungal, M. G. (2010) Concentration flux measurements in a polymer drag-reduced turbulent boundary layer. *Journal of Fluid Mechanics, 644*, 281-319.

Spalart, P. R. (1988). Direct simulation of a turbulent boundary layer up to $R_\theta = 1410$. *Journal of Fluid Mechanics*, *187*, 61-98.

Theodorsen, T. (1952). Mechanism of turbulence. In *Proceedings of the Second Midwestern Conference on Fluid Mechanics*. Ohio State University, Columbus, OH.

Tiederman, W. G., Luchik, T. S., & Bogard, D. G. (1985). Wall-layer structure and drag reduction. *Journal of Fluid Mechanics, 156*, 419-437.

Toms, B. A. (1948). Some observations on the flow of linear polymer solutions through straight tubes at large Reynolds numbers. In *Proceedings of the First International Congress on Rheology,* 135.

Townsend, A. A. (1961). Equilibrium layers and wall turbulence. *Journal of Fluid Mechanics, 11*(1), 97-120.

Vanapalli, S. A., Islam, M. T., & Solomon, M. J. (2005). Scission-induced bounds on maximum polymer drag reduction in turbulent flow. *Physics of Fluids, 17*(9), 095108.

Vanapalli, S. A., Ceccio, S. L., & Solomon, M. J. (2006). Universal scaling for polymer chain scission in turbulence. *Proceedings of the National Academy of Sciences, 103*(45), 16660-16665.

Van Doorn, E., White, C. M., & Sreenivasan, K. R. (1999). The decay of grid turbulence in polymer and surfactant solutions. *Physics of Fluids, 11*(8), 2387-2393.

Virk, P. S. (1971). Drag reduction in rough pipes. *Journal of Fluid Mechanics, 45*(2), 225-246.

Virk, P. S. (1975). Drag reduction fundamentals. *AIChE Journal, 21*(4), 625-656.

Virk, P. S., Merrill, E. W., Mickle, H. S., Smith, K. A., & Mollo-Christensen, E. L. (1967). The Toms phenomenon: Turbulent pipe flow of dilute polymer solutions. *Journal of Fluid Mechanics, 30*(2), 305-328.

Volino, R. J., & Schultz, M. P. (2018). Determination of wall shear stress from mean velocity and Reynolds shear stress profiles. *Physical Review Fluids, 3*(3), 034606.

Wallace, J. M. (2016). Quadrant analysis in turbulence research: history and evolution. *Annual Review of Fluid Mechanics, 48*, 131-158.

Warholic, M. D., Massah, H., & Hanratty, T. J. (1999). Influence of drag-reducing polymers on turbulence: Effects of Reynolds number, concentration and mixing. *Experiments in Fluids, 27*(5), 461-472.

Warholic, M. D., Heist, D. K., Katcher, M., & Hanratty, T. J. (2001). A study with particle-image velocimetry of the influence of drag-reducing polymers on the structure of turbulence. *Experiments in Fluids, 31*(5), 474-483.

Wei, T., & Willmarth, W. W. (1989). Reynolds-number effects on the structure of a turbulent channel flow. *Journal of Fluid Mechanics, 204*, 57-95.

Wei, T., & Willmarth, W. W. (1992). Modifying turbulent structure with drag-reducing polymer additives in turbulent channel flows. *Journal of Fluid Mechanics, 245*, 619-641.

Wells, Jr. C. S., & Spangler, J. G. (1967). Injection of a Drag-Reducing Fluid into Turbulent Pipe Flow of a Newtonian Fluid. *The Physics of Fluids, 10*(9), 1890-1894.

White, F. M., (2006). *Viscous Fluid Flow* (Vol. 3, pp. 433-434). New York: McGraw-Hill.

White, C. M., & Mungal, M. G. (2008). Mechanics and prediction of turbulent drag reduction with polymer additives. *Annual Review of Fluid Mechanics, 40*, 235-256.

White, C. M., Somandepalli, V. S. R., Mungal, M. G. (2004). The turbulence structure of drag-reduced boundary layer flow. *Experiments in Fluids, 36*(1), 62-69.

White, C. M., Dubief, Y., Klewicki, J. (2012). Re-examining the logarithmic dependence of the mean velocity distribution in polymer drag reduced wall-bounded flow. *Physics of Fluids, 24*(2), 021701.

Wieneke, B. (2015). PIV uncertainty quantification from correlation statistics. *Measurement Science and Technology, 26*(7), 074002.

Wu, J., & Tulin, M. P. (1972). Drag reduction by ejecting additive solutions into pure-water boundary layer. *Journal of Basic Engineering, 94*(4), 749-754.

Wu, Y., & Christensen, K. T. (2010). Spatial structure of a turbulent boundary layer with irregular surface roughness. *Journal of Fluid Mechanics, 655*, 380-418.

Xi, L. (2019). Turbulent drag reduction by polymer additives: Fundamentals and recent advances. *Physics of Fluids, 31*(12), 121302.

Yu, J. F. S., Zakin, J. L., & Patterson, G. K. (1979). Mechanical degradation of high molecular weight polymers in dilute solution. *Journal of Applied Polymer Science, 23*(8), 2493-2512.

Zagarola, M. V., & Smits, A. J. (1998). Mean-flow scaling of turbulent pipe flow. *Journal of Fluid Mechanics, 373*, 33-79.

Zaitoun, A., Makakou, P., Blin, N., Al-Maamari, R. S., Al-Hashmi, A-AR., & Abdel-Goad, M. (2012). Shear stability of EOR polymers. *SPE Journal, 17*(2), 335-339.

Zaman, K. B. M. Q., & Hussain, A. K. M. F. (1981). Taylor hypothesis and large-scale coherent structures. *Journal of Fluid Mechanics, 112,* 379-396.

Zhou, J., Adrian, R.J., Balachandar, S., & Kendall, T. (1999). Mechanisms for generating coherent packets of hairpin vortices in channel flow. *Journal of Fluid Mechanics, 387* (1), 353-396.

Zimm, B. H. (1956). Dynamics of polymer molecules in dilute solution: Viscoelasticity, flow birefringence and dielectric loss. *The Journal of Chemical Physics*, *24*(2), 269-278.

VITA

Yasaman Farsiani

Candidate for the Degree of

Doctor of Philosophy

Dissertation: MODIFICATION OF A HIGH REYNOLDS NUMBER TURBULENT BOUNDARY LAYER WITH THE ADDITION OF DRAG-REDUCING POLYMER SOLUTION

Major Field: Mechanical and Aerospace Engineering

Biographical:

Education:

Completed the requirements for the Doctor of Philosophy in Mechanical Engineering at Oklahoma State University, Stillwater, Oklahoma in May 2020.

Completed the requirements for the Master of Science in Aerospace Engineering at Amirkabir University of Technology, Tehran, Iran in 2014.

Completed the requirements for the Bachelor of Science in Aerospace Engineering at Azad University, Tehran, Iran in 2011.

Experience: Graduate Teaching/Research Assistant at the School of Mechanical and Aerospace Engineering, Oklahoma State University, Stillwater from 2015- 2020.

Professional Memberships: American Society of Mechanical Engineers (ASME), American Physical Society Division of Fluid Dynamics (APS-DFD)